

Solid-state NMR spectroscopy for structural investigations in materials science

Von der Fakultät Chemie der Universität Stuttgart zur Erlangung
der Würde eines Doktors der Naturwissenschaften (Dr. rer. nat.)
genehmigte Abhandlung

vorgelegt von

Matthias Abele

aus Plüderhausen

Hauptberichter: Prof. Dr. Emil Roduner

Mitberichter: Prof. Dr. Michael Hunger

Zweiter Mitberichter: Prof. Dr. Paolo Scardi

Tag der Prüfung: 8. Februar 2012

Institut für Physikalische Chemie der Universität Stuttgart
Stuttgart 2012

TO PROF. DR. KLAUS MÜLLER
(† 01.04.2011)

Acknowledgements

I would like to thank all people who supported me in different ways during the elaboration of this thesis.

First of all I want to thank **Prof. Dr. Klaus Müller** for all the support he gave me from the very beginning of my work in his group, but also for the friendship I experienced during the four years I could work together with him.

Special thanks go to **Prof. Dr. Emil Roduner** for taking care of my thesis by taking over the supervision of my thesis and integrating me in his work group. It is mainly due to his help that I was able to finish my thesis in a good and straight-lined way.

I also would like to thank **Prof. Dr. Paolo Scardi** for the prosperous collaboration and for his role as member of the examination committee.

I want to thank **Prof. Dr. Michael Hunger** for his role as co-examiner and writing the second advisory opinion.

Prof. Dr. Sabine Ludwigs is kindly acknowledged for taking the chair in the examination board.

Thanks are given to **Prof. Dr. Renzo Campostrini**, **Prof. Dr. Sandra Diré** and **Prof. Dr. Rosa Di Maggio** from the University of Trento for their active support, especially during the last period of my thesis.

Thanks goes to **Dr. Frank Wallasch** and **Ahmed Mahmoud Abdellatief Mahmoud** for the joint work which I continuously enjoyed.

I would like to kindly acknowledge **Benjamin, Fabri, Simone** and **all colleagues** at the University of Trento and the University of Stuttgart for creating a pleasant working atmosphere.

Great thanks goes to **Beatrice** for being always there, when help was needed.

I would like to thank **Steffen** for the friendship and the many motivative talks during my studies and my time as PhD student.

I want to thank **Silvia** for all the support and the hospitality.

Renzo I want to thank for showing me and friendly enjoying with me the wonderful mountains of Trentino.

I thank **Gabriela, Stefano, Roberto** and their families, as well as **Gino** for all the help and support they gave me and for making Trento a second home for me...*Grazie mille.*

My family I want to heartily thank for giving me the trust and the support during my studies.

Last but not least I want to express my deepest gratitude to **Bernadette** for all the support, patience and love she gave me at all times.

TO ALL THANKS.

Contents

1	Introduction	1
2	Methodological background	7
2.1	Nuclear Magnetic Resonance	7
2.1.1	Interaction with external magnetic fields	7
2.1.2	The NMR experiment	12
2.1.3	Internal interactions	16
2.1.4	Decoupling techniques	26
2.1.5	Common NMR techniques	32
2.1.6	Experimental parameters	38
2.2	X-ray structure analysis	39
2.2.1	Theoretical basis of X-ray diffraction	39
2.2.2	Whole Powder Pattern Modelling with PM2K	47
3	Optimized ^{19}F decoupling techniques for fluorinated membranes	51
3.1	Introduction	51
3.2	Results and Discussion	54
3.3	Conclusion	64
4	Characterization of radiation grafted polymer films using CP/MAS NMR spectroscopy	65
4.1	Introduction	65
4.2	Sample preparation	69
4.3	Results and Discussion	70
4.4	Conclusions	76
5	Solid state NMR and XRD line profile analysis of heavily deformed fluorite	79
5.1	Introduction	79

Contents

5.2	Sample preparation	82
5.3	Results and Discussion	83
5.3.1	CaF ₂ milled using WC balls	83
5.3.2	Discussion of the relaxation effects	95
5.3.3	CaF ₂ milled using steel balls	98
5.4	Conclusion	107
6	Summary	111
7	Zusammenfassung	121
	Abbreviations and variables	131
	List of figures	136
	List of tables	143
	References	145

1 Introduction

Nuclear magnetic resonance (NMR) spectroscopy plays a most central role in all fields of chemistry and material science. The importance of solution-state NMR is extensively known and the application well established. Individual nuclei in a molecule are characterized by their chemical shift which allows the identification of a certain kind of nucleus. The intermolecular connectivities play an important role in the signal assignment and are accessible by the through-bond J-coupling which is manifested in characteristic splittings found in spectra. Through-space connectivities which hold information about the three-dimensional structure are accessible by experiments exploiting the nuclear Overhauser effect (NOE). A huge variety of specialized sequences have been developed to further enhance the information which is accessible by this technique.^{1,2}

However, the appropriate state of sample to investigate the molecular structure and dynamics often is the solid-state (ss). Even if the basic principle of solution-state-NMR spectroscopy is exactly the same as for ss-NMR spectroscopy, the latter is found to be much more complicated. The reason for this found in additional interactions being not, or at least to a lesser extent distinctive present in the solution-state. The well resolved solution-state NMR spectra are the result of a fast isotropic molecular tumbling, i.e. the spectra are recorded in an isotropic solution. In most cases in the solid-state, this molecular motion is hindered with the consequence of an anisotropic character for most interactions, e.g. the dipolar coupling, the chemical shift anisotropy (CSA) and the quadrupolar coupling.^{3,4} These anisotropic interactions lead to a strong broadening of the resonances in a ss-NMR spectrum, e.g. the strong ^1H dipolar coupling network in protonated organic solids leads to a static line broadening in the order of 50 kHz. The nature and theoretical description of these interactions with respect to their anisotropic character are discussed in chapter 2.1.3.

The results in this thesis are divided into three parts dealing with different aspects of the application of solid-state NMR as an analytical tool in material science instead

of keeping the focus on one certain material which could be analysed by several analytical approaches. The following introduction gives an overview of the most important aspects of ss-NMR spectroscopy and allows me to introduce the three independent central topics of my thesis.

On the one hand the mentioned interactions contain information about the structure and the dynamics. Especially the dipolar coupling can give information about inter- and intramolecular distances, while the CSA and the quadrupolar coupling can provide knowledge about the electronic structure and chemical bonds. On the other hand, these anisotropic interactions and the related line broadening are a big disadvantage, since they preclude the possibility to record highly resolved spectra. For this reason one major field of ss-NMR deals with techniques which are able to compensate these effects at least partly. One possibility is the widely used magic angle spinning (MAS). The MAS technique exploits an angular dependency to average the interaction by a fast rotation of the sample about an axis with an angle of 54.74° with respect to the external magnetic field. This technique is commonly used and described in detail in chapter 2.1.4. Instead of the MAS, or as an additional method to remove residual line broadening, RF decoupling techniques are applied which are also used in solution-state NMR. RF decoupling in general aims for the removal of unwanted interactions by applying some kind of RF irradiation. There are two kinds of sequences, multipulse decoupling and decoupling under continuous irradiation. RF decoupling can be further grouped into hetero- and homonuclear decoupling. Typically RF decoupling is used in combination with MAS. In literature one can find a huge number of different decoupling techniques which are designed for the different purposes and combination of nuclei.⁵⁻⁷

Especially for spin systems containing ^{19}F the hetero- and homonuclear decoupling is a challenging subject. It is known from literature that the so called XY-16 sequence is most appropriate to achieve a good decoupling performance for fluorinated polymers. This will be briefly described in chapter 2.1.4.⁸ Based on these results I will further investigate the conditions, under which the XY-16 sequence can or has to be used with respect to parameters as the spinning rate or the decoupling frequency offset. Another objective will be the attempt to adopt other decoupling sequences known from the use in proton containing systems. The most widely used sequence, combining cw irradiation and phase modulation, is the two pulse phase modulation (TPPM) decoupling scheme also described in chapter 2.1.4.⁵ An alternative to the TPPM scheme is the XiX sequence, also based on continuously repeated pulses with

a phase shift of 180° .^{6,7} After evaluating the potential of this alternative decoupling scheme, a detailed analysis will provide information about the characteristics and experimental conditions of the technique. My results related to the **^{19}F decoupling techniques for fluorinated membranes**, their interpretation and discussion are found in **chapter 3**.

All nuclei with a non-zero spin can be accessible by NMR techniques. Table 2.1 shows exemplary NMR-active nuclei and their properties. One distinguishes between nuclei with a spin of $I = \frac{1}{2}$ and nuclei with a nuclear spin of $I > \frac{1}{2}$ which possess a quadrupole moment.⁹ Another possibility to classify two groups of nuclei is based on the natural abundance of the isotopes. Nuclei with a high natural abundance of over 99% are referred to as being abundant, e.g. ^1H , ^{19}F or ^{31}P . Since the sensitivity correlates with the amount of nuclei in the sample, one can expect relative high signal intensities for such nuclei. Nevertheless, many nuclei of interest are characterized by a low natural abundance referred to as being rare or dilute spins, e.g. ^{17}O or ^{15}N . For them the very low signal intensity is an additional challenge when spectra are recorded. One possibility to overcome this problem is the artificial enrichment of the NMR active nucleus which if done for a selective position even can lead to additional information. However, isotope enrichment is always related to additional synthesis work and causes high additional costs.

The cross-polarization (CP) experiment is another possibility to overcome the problem of low signals for dilute nuclei with low natural abundances, e.g. ^{13}C . The idea of this concept is to produce the magnetization on a nucleus with a high natural abundance, e.g. ^1H or ^{19}F , and transfer the magnetization to the low abundance nucleus. Another reason for using the CP experiment can be a long spin-lattice relaxation time, since for the CP experiment the T_1 of the undetected spin is essential for the choice of the delay between two experiments. The CP sequence is used for a large variety of pairs of nuclei, e.g. ^1H - ^{13}C , ^1H - ^{15}N or ^1H - ^{31}P . The CP experiment is described in chapter 2.1.5. As it is outlined there, the dynamic of the magnetization transfer is affected by many parameters (e.g. proton density, internuclear distances and dipolar coupling) and can strongly differ for different molecules or even different nuclei in one molecule, i.e. the signal integrals in general cannot be used in a quantitative manner. Several specially designed sequences are known in literature which can be able to overcome this problem under certain conditions, e.g. the quantitative cross polarization (QUCP) sequence.¹⁰ The use of a ramped CP sequence is also known to partially compensate for these unwanted effects. In

chapter 4 of this thesis I will present results for the **characterization of radiation grafted polymer films using CP/MAS NMR spectroscopy**. It will be shown that in the case of such materials the ramped CP sequence can be used for the determination of relative ratios between two different molecules in the polymer.

Another very important parameter related to NMR spectroscopy is the relaxation time which describes the relaxation of a spin system back to its equilibrium state, i.e. if a sample is allowed to evolve unperturbed for a long time, the initial state of thermodynamic equilibrium will be restored. One can distinguish between two kinds of relaxation: (i) The spin-lattice relaxation T_1 describes the relaxation of the spin populations back to their Boltzmann-distribution values and (ii) the spin-spin relaxation T_2 describing the decay of the single-quantum coherences. The theoretical background is briefly described in chapter 2.1.3. There are many examples in literature where the analysis of the relaxation times, normally in combination with variable temperature measurements, was used to examine the dynamics of a large variety of materials, e.g. inclusion compounds or peptide membranes.^{11–13}

Another application of relaxation time studies is found to be the distinction between different species or states present in a sample, e.g. relaxation measurements have been widely used to investigate the different states of water in cement.¹⁴ Thereby it is possible to describe systems with up to seven phases, e.g. chemically bound water, water in small gel pores and water in larger capillary pores.¹⁵ Another reason for the occurrence of species which differ in their relaxation behaviour is the presence of bulk and surface relaxation which is often present in nano crystalline materials.¹⁶ However, even if the presence of two or more components in the relaxation data is obvious, it is normally not easy to fully understand the nature of the two components taking into account only the NMR data, especially if the chemical shift of the two components is similar and no spectral separation can be achieved. In the thesis I will present results dealing with the **Solid state NMR and XRD line profile analysis of heavily deformed fluorite** in **chapter 5**. This study is based on a series of CaF_2 samples which was prepared by high energy ball milling, whereby tungsten carbide (WC) and steel were used as materials for the vial and the balls of the planetary mill and the milling time was varied between 4 h and 64 h. The samples were analysed by means of NMR spin lattice relaxometry and X-Ray diffraction in combination with line profile analysis (LPA). As it will be described in this chapter, it was possible for this system to distinguish and quantify two components by NMR T_1 relaxometry. In the end the combination of NMR spectroscopy

and XRD line profile analysis proved itself able to not only detect and quantify the two phases, but to clearly identify and characterize the two components. This in turn gives rise to a clear description of the micro structural processes during the milling.

The title of the present thesis, **Solid-state NMR spectroscopy for structural investigations in material science**, already foretells that the central aspect of this thesis is not found in a certain material, but in the method of NMR spectroscopy itself. Therefore, as described above the present thesis is composed of three independent chapters dealing with different aspects of ss-NMR, namely a more methodological part dealing with the improvement of ^{19}F decoupling for fluorinated polymers (**Chapter 3: ^{19}F decoupling techniques for fluorinated membranes**), the use of ^{13}C MAS NMR spectroscopy to quantify the ratio of monomers in a fluorinated polymer (**Chapter 4: Characterization of radiation grafted polymer films using CP/MAS NMR spectroscopy**) and the use of relaxation measurements to identify different species present in a ball-milled CaF_2 (**Chapter 5: Solid state NMR and XRD line profile analysis of heavily deformed fluorite**). While this introduction is kept relatively general, the reader will find a separate and more detailed introduction in the beginning of each chapter.

2 Methodological background

2.1 Nuclear Magnetic Resonance

2.1.1 Interaction with external magnetic fields

Nuclear Magnetic Resonance (NMR) is an important method for structure determination and dynamic studies on a molecular level.^{17,18} All materials containing nuclei with a non-zero spin are accessible by this method.

Table 2.1: Exemplary NMR-active nuclei and their properties

	Protons	Neutrons	nuclear Spin	Natural Abundance
¹ H	1	0	$\frac{1}{2}$	99.985
² H	1	1	1	0.015
¹³ C	6	7	$\frac{1}{2}$	1.1
¹⁹ F	9	10	$\frac{1}{2}$	100
³¹ P	15	16	$\frac{1}{2}$	100

Following the laws of quantum mechanics the nuclear intrinsic angular momentum of a nucleus is quantized.

$$P = \sqrt{I(I+1)}\hbar \quad (2.1)$$

\hbar is the Planck's constant ($\frac{h}{2\pi} = 1,0545 \cdot 10^{-34} Js$) and I the magnetic quantum number. I can be a positive integer or half-integer. This nuclear intrinsic angular

2 Methodological background

momentum P is related to a magnetic moment μ .

$$\mu = \gamma P \quad (2.2)$$

It is linked by the gyromagnetic ratio $\gamma = \frac{\mu}{P}$. The gyromagnetic ratio is a characteristic constant for each nucleus. Equations (2.1) and (2.2) give rise to the magnetic moment of a nucleus.

$$\mu = \gamma \sqrt{I(I+1)}\hbar \quad (2.3)$$

A nucleus with a non-zero spin in a static magnetic field B_0 ($\vec{B} = (0, 0, B_0)$) is affected by the Zeeman interaction. The spin angular momentum P is oriented in such a way, that the component parallel to the external magnetic field (z -component) is an integer- or half-integer multiple of the Planck's constant.

$$P_z = m_I \hbar \quad (2.4)$$

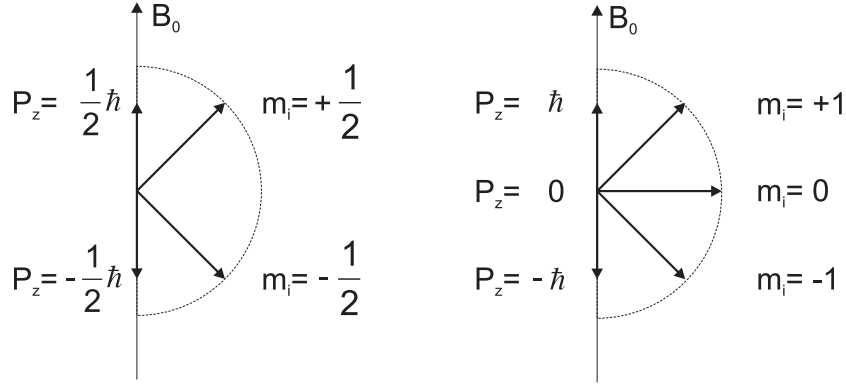
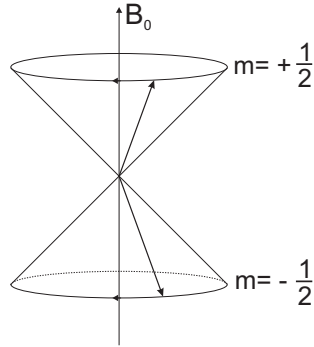
The eigenvalues of P_z are quantized and related to the magnetic quantum number m_I .

$$m_I = I, I-1, \dots, -I \quad (2.5)$$

The number of possible eigenvalues is given by $(2I+1)$. Figure 2.1, as an example, shows the quantization for nuclei with $I = 1$ and $I = \frac{1}{2}$.

The z -component of the magnetic moment is also quantized and by use of equations (2.2) and (2.4) given by:

$$\mu_z = m_I \gamma \hbar \quad (2.6)$$


 Figure 2.1: Quantization for the spin angular momentum P in a magnetic field

 Figure 2.2: Precession double cone for a spin $I = \frac{1}{2}$ nucleus

Having a look at the system in a classical manner, the spins in a magnetic field precess about the external z -axis (Fig. 2.2). The so-called Larmor frequency is described by the gyromagnetic ratio γ and the magnetic flux density B_0 .

$$\nu_L = \left| \frac{\gamma}{2\pi} \right| B_0 \quad (2.7)$$

The energy E of a magnetic dipole μ in a magnetic field B_0 is given by:

$$E = -\mu_z B_0 \quad (2.8)$$

2 Methodological background

Since the spins possess $(2I + 1)$ possibilities of orientation one can find the same number of Zeeman states (Fig. 2.3).

$$E = -m\gamma\hbar B_0 \quad (2.9)$$

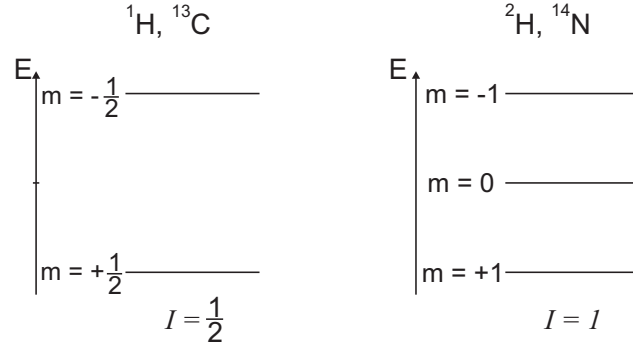


Figure 2.3: Energy levels for an $I = \frac{1}{2}$ and an $I = 1$ spin-system

The equidistant energy differences are characterized by a field-dependent term.

$$\Delta E = \gamma\hbar B_0 \quad (2.10)$$

In the classical model a full ensemble of nuclear spins do precess on a common double cone.

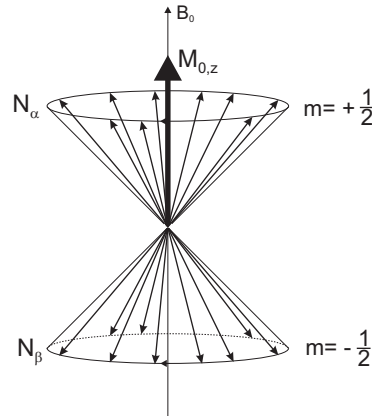


Figure 2.4: Formation of the macroscopic magnetization for ensemble spin- $\frac{1}{2}$ nuclei

The summation of all z-components gives the net magnetization along the z-axis, called M_0 .

$$M_0 = \sum_i \mu_{z,i} \quad (2.11)$$

Consequently the macroscopic magnetization is directly related to the occupation of the different states which for example can be described by a Boltzmann distribution. For a spin- $\frac{1}{2}$ nucleus with z-components α and β it is:

$$\frac{N_\beta}{N_\alpha} = e^{-\frac{\Delta E}{k_B T}} \quad (2.12)$$

By the use of the Boltzmann constant k_B and the temperature T one gets values which mostly differ only in the fifth decimal place, i.e. the net magnetization in general is very low.

In an NMR experiment transitions between these different energy levels are induced. This is done by an additional field \vec{B}_1 , or rather electromagnetic radiation with a corresponding energy aligned orthogonal to B_0 .

$$h\nu_1 = \Delta E \quad (2.13)$$

The transitions occur in both directions, from the lower to the higher energy level and inversely. Due to the population difference the adsorption is the dominant process, i.e. the detected signal is proportional to the population difference $N_\alpha - N_\beta$.

The resonance constraint arises from equations (2.9) and (2.13).

$$\nu_L = \nu_1 = \left| \frac{\gamma}{2\pi} \right| B_0 \quad (2.14)$$

Thereby only transitions are allowed which follow the selection rule $\Delta m = \pm 1$.

2.1.2 The NMR experiment

In general there are two approaches to perform a NMR experiment:

cw-experiment: When using the cw-method the transitions are induced by a continuous high-frequency field with a low amplitude. During the signal acquisition the frequency ν_1 or the field strength B_0 is changed continuously. Due to the possibly long relaxation time, this method is, compared to the FT-experiment, relatively time consuming.

FT-experiment: For this approach the sample is irradiated with a very short high-power radiofrequency (RF) pulse, causing a perturbation of the equilibrium magnetization, and transverse magnetization is formed. After the pulse, the time evolution of the transverse magnetization is recorded and transformed into the frequency space by a Fourier transform. Another advantage is the possibility of applying multi-pulse sequences, which drastically expand the potential of NMR.

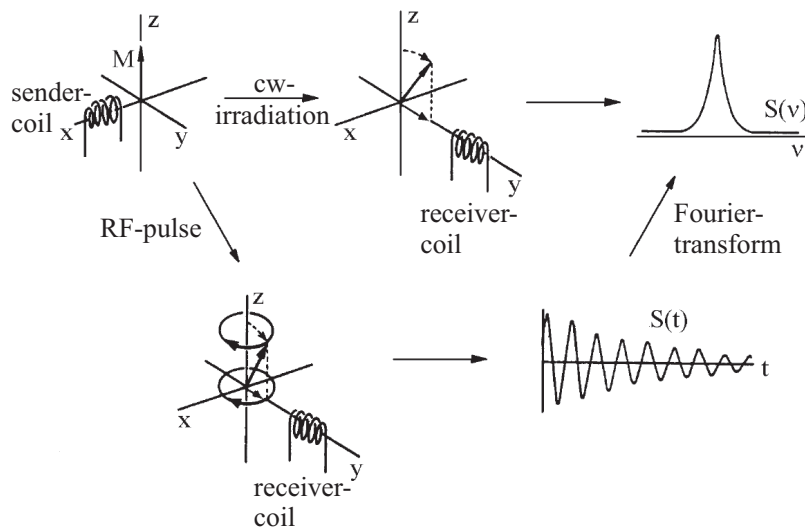


Figure 2.5: Schematic comparison of the cw- und FT-experiment¹⁹

Historically the method used for acquiring NMR spectra was the cw-experiment, but it lost its prominence after the introduction of FT-NMR-spectrometers in the end of the sixties. Today nearly only the FT-method is used.

As already described, when using the FT-method all nuclei of one kind in a sample are excited by a high-power RF-pulse. The frequency generator produces

one fixed frequency ν_1 . When opening the amplifier gate only for a very short time, a rectangular "hard" pulse is formed, containing a range of frequencies around the carrier-frequency ν_1 . This makes it possible to excite all spins, even if they differ in their transition frequency. For NMR experiments the pulse lengths are in the range of μs , while the amplifier powers are in the range of some Watt for liquid NMR applications, while for solid-state NMR experiments these are in the range of some hundreds of Watts.

In a one-pulse experiment the pulse is applied along the x-axis. The oscillating magnetic component of the electro-magnetic radiation, called \vec{B}_1 , interacts with the nuclear dipole. This interaction rotates the magnetization from the z-axis into the x-y-plane. The longer the pulse and the higher the pulse amplitude, the stronger the magnetization is influenced.

$$\theta = \gamma \vec{B}_1 \tau_P \quad (2.15)$$

It is mathematically very difficult to describe the motion of the magnetization in a stationary coordinate system. Therefore a rotating coordinate system (x' , y' , z') is introduced. The so-called rotating frame is a coordinate system which is rotates about the z-axis with the Larmor frequency. In most common experiments one can find 90° - and 180° -pulses, rotating the magnetization into the x-y-plane and along the -z-axis, respectively. Figure 2.6 sketches a 90° - and a 180° -pulse in the rotating frame.

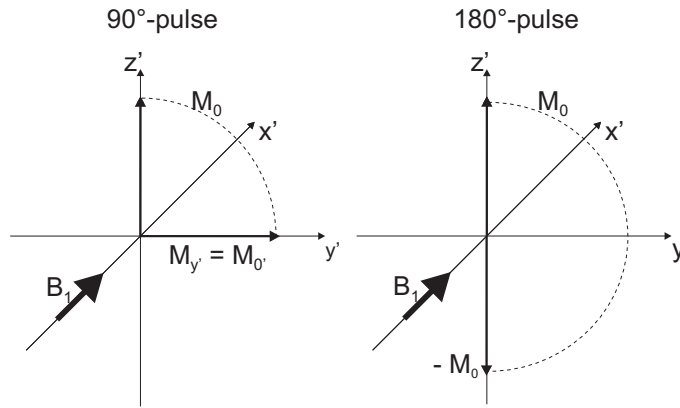


Figure 2.6: 90° - and 180° -pulse in the rotating frame

Directly after a pulse the magnetization vector starts moving back into equilibrium. Thereby it is precessing, comparable to an isolated spin, about the z-

2 Methodological background

axis. Bloch provided the mathematical expressions describing this process in a phenomenological way.

$$\frac{dM_z}{dt} = -\frac{M_z - M_0}{T_1} \quad (2.16)$$

$$\frac{dM_{x'}}{dt} = -\frac{M_{x'}}{T_2} \quad (2.17)$$

$$\frac{dM_{y'}}{dt} = -\frac{M_{y'}}{T_2} \quad (2.18)$$

T_1 is called the spin-lattice or longitudinal relaxation and describes the energy exchange between the spin system with all the other degrees of freedom. This decay of M_z is the critical parameter for the experimental delay between two experiments and is typically measured by using an inversion-recovery sequence, which is discussed later. The spin-spin or transverse relaxation time T_2 describes the decay of M_{xy} . Directly after the pulse all spins are in-phase. The loss of this phase coherence is described by T_2 and can be measured by using a simple Hahn-Echo sequence. A more detailed description of the relaxation effects is found in chapter 2.1.3.

Figure 2.5 sketches a simple one-pulse experiment. After the 90° -pulse, which is applied along the x-axis, the detection is performed along the y-axis. The detected signal is called the Free Induction Decay (FID) which is described by the Bloch equations (figure 2.7).

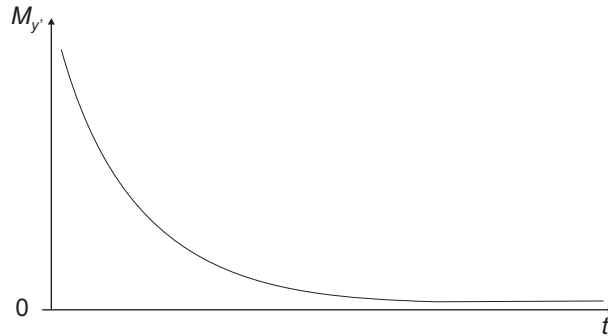
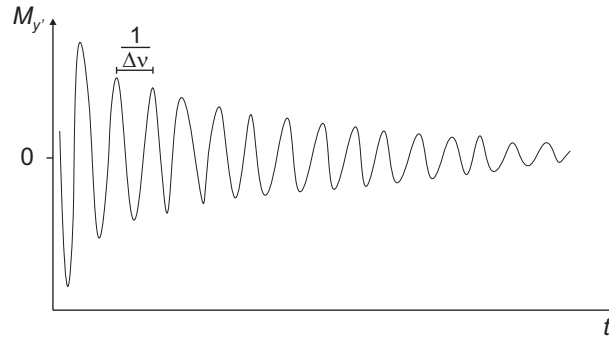


Figure 2.7: Evolution of the transverse magnetization $M_{y'}$

Such an ideal FID will only be observed if the resonance frequency exactly matches the carrier frequency. For a nucleus for which the resonance frequency differs from the carrier frequency one will observe an oscillating FID. In this case the difference between two maxima corresponds to the reciprocal difference between the resonance frequency and the carrier frequency.

Figure 2.8: Schematic FID $f(t)$ for an isolated spin, e.g. in CH_3I

If the sample contains more than one spin differing in their resonance frequency or if couplings are present, the different decay curves are superimposed in one FID. After a Fourier transform the superimposed curves are represented by isolated peaks in the spectrum (figure 2.9).

$$g(\omega) = \int_{-\infty}^{+\infty} f(t)e^{-i\omega t}dt \quad (2.19)$$

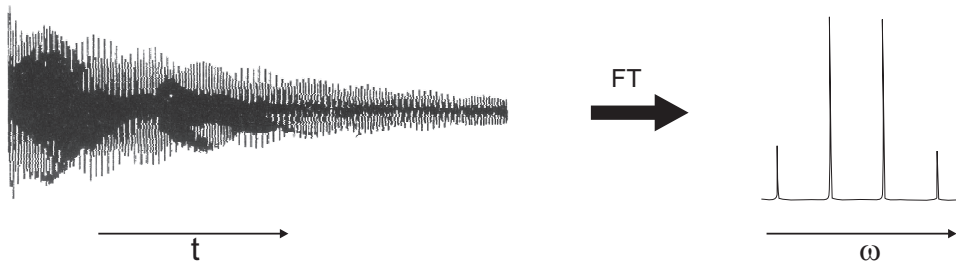


Figure 2.9: Example of a Fourier transform

2.1.3 Internal interactions

The intensity of a signal in a single-pulse experiment is proportional to the population difference, while the position and the shape of a signal is related to many different effects.¹⁹ In other words, the relevant overall Hamiltonian is built-up by a series of independent terms.

$$\hat{H}_{NMR} = \hat{H}_Z + \hat{H}_{RF} + \hat{H}_{CS} + \hat{H}_D + \hat{H}_K + \hat{H}_P + \hat{H}_Q \quad (2.20)$$

Where z is the Zeeman-, RF the radio frequency, CS the chemical shift, D the dipolar, K the Knight-shift, P the paramagnetic and Q the quadrupolar interaction. At this point only the most important interactions will be described.

Chemical Shift

The applied external magnetic field is not equal to the field that is locally present at a certain nucleus. The electronic surrounding slightly changes the Zeeman interaction, which in turn changes the resonance frequency. This can be demonstrated by the appropriate Hamiltonian.

$$\hat{H}_{CS} = \gamma \hbar B_0 \sigma \hat{I} \quad (2.21)$$

σ is the chemical shift tensor and implies the anisotropic character of this interaction. Figure 2.10 visualizes this effect, showing a powder pattern for a molecule with an axially symmetric chemical shift tensor. In this context a "powder pattern" is a sample in which the molecular orientations are statistically distributed.

In an isotropic solution only the isotropic chemical shift interaction is present, since the orientation of individual molecules is averaged by molecular motions. In this case the chemical shift is characteristic for certain functional groups and it is widely used in structure determination.

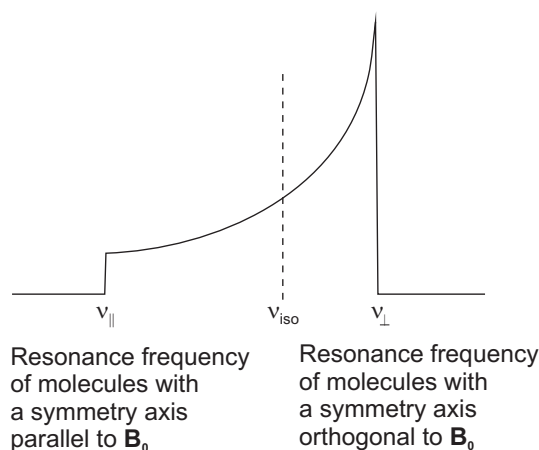


Figure 2.10: Powder pattern for a molecule with an axially symmetric chemical shift tensor

The resonance frequency is proportional to the external magnetic field M_0 . For this reason the chemical shift δ is commonly given in ppm, referenced to a reference compound, and independent of B_0 .

$$\delta_{\text{sample}} = \frac{\nu_{\text{sample}} - \nu_{\text{reference}}}{\nu_{\text{reference}}} \quad (2.22)$$

$$\delta_{\text{sample}}[\text{ppm}] = \frac{\Delta\nu}{\nu_{\text{reference}}} \frac{[\text{Hz}]}{[\text{MHz}]} \quad (2.23)$$

J-Coupling

If two nuclear spins are connected through a chemical bond, they can interact through the bonding electrons. The following equation represents the related Hamiltonian.

$$\hat{H}_J = h \hat{I} \mathbf{J} \hat{S} \quad (2.24)$$

\mathbf{J} is a tensor, representing the anisotropic character of this interaction and \hat{I} , \hat{S} are the spin operators.

Like for the chemical shift anisotropy (CSA) the anisotropic character is averaged in an isotropic solution and only the isotropic part of the J coupling is left. In this case the J-coupling is also known as scalar coupling. While for solid-state NMR the J-coupling in most cases is negligible, in solution NMR it is an important

feature. Figure 2.11 shows an NMR spectrum recorded for ethyl acetate, in which the neighbouring CH₃- and CH₂-groups are represented by a triplet and quartet, respectively.

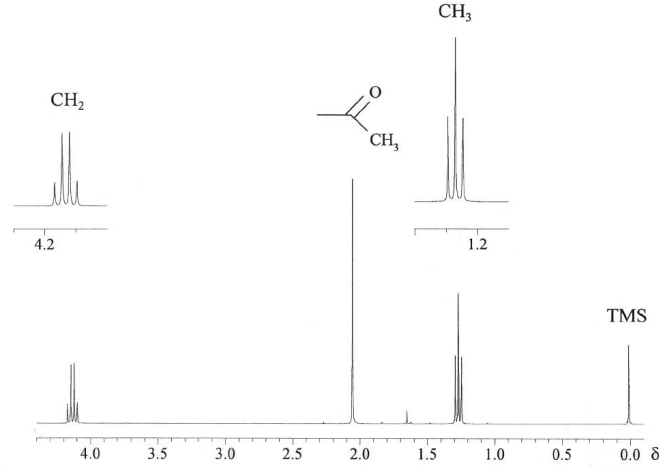


Figure 2.11: Example for J-coupling in an anisotropic solution

Dipolar coupling

As described earlier, every nuclear spin is related to a magnetic moment. This magnetic moment can interact through space with other nuclear spins in the local surrounding. This interaction is called the dipolar coupling or dipole-dipole coupling. In the classic model this interaction can be described as two bar magnets "feeling" each other. The corresponding quantum mechanical operator is given by:

$$\hat{H}_D = \frac{\mu_0}{4\pi} \gamma_1 \gamma_2 \hbar^2 \left\{ \frac{\hat{I}_1 \hat{I}_2}{r^3} - 3 \frac{(\hat{I}_1 \vec{r})(\hat{I}_2 \vec{r})}{r^5} \right\} \quad (2.25)$$

where γ_i is the gyromagnetic ratio, \hat{I}_i are the spin operators and \vec{r} is the vector describing the distance and the relative orientation between the two interacting spins. Dipolar coupling is a purely anisotropic effect and can only influence the relaxation behaviour in solution. Figure 2.12 illustrates the orientation dependency of two dipolar coupled spins. The magnetic moment of each spin is orientated with respect to the external magnetic field and so the interaction is dependent on this orientation.

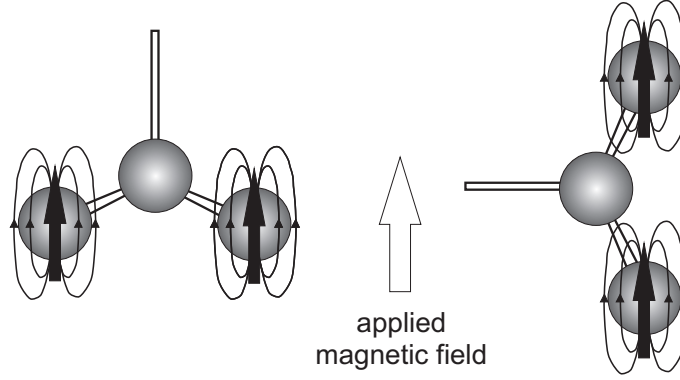


Figure 2.12: Illustration of the orientation dependency of the dipolar coupling¹⁷

When describing dipolar coupling one has to distinguish between homo- and heteronuclear dipolar coupling. For the homonuclear case one can show that equation (2.25) can be transformed to:

$$\hat{H}_D^{homo} = -d \frac{1}{2} (3 \cos^2 \theta - 1) \left[3 \hat{I}_z \hat{S}_z - \hat{\vec{I}} \cdot \hat{\vec{S}} \right] \quad (2.26)$$

$$d = \hbar \left(\frac{\nu_0}{4\pi} \right) \frac{1}{r^3} \gamma_I \gamma_s \quad (2.27)$$

while a dipolar coupling constant d is defined and θ is describing the orientation of the dipole with respect to the external magnetic field. The heteronuclear dipolar coupling not only shifts the different Zeeman levels ($\hat{I}_z \hat{S}_z$), but also mixes the normally degenerate states ($\hat{\vec{I}} \cdot \hat{\vec{S}}$). This is the reason for an undefined broadening of the lines by the dipolar coupling in a multispin system. The effect of dipolar coupling is illustrated in figure 2.13.

Describing the heteronuclear dipolar coupling is straightforward and one can show that it does not lead to a mixing of the Zeeman levels.

$$\hat{H}_D^{hetero} = -d (3 \cos^2 \theta - 1) \hat{I}_z \hat{S}_z \quad (2.28)$$

The heteronuclear dipolar coupling for this reason is more similar to the scalar coupling discussed above. The Zeeman levels are only shifted and by looking at two coupled spin $-\frac{1}{2}$ nuclei I and S one can see that both possible transitions have the same isotropic frequency and are like mirror images to each other. Figure 2.14 sketches the shift of the Zeeman levels and shows an exemplary powder pattern for

2 Methodological background

a spin I with an axially symmetric CSA, and which is heteronuclear coupled to a spin S .

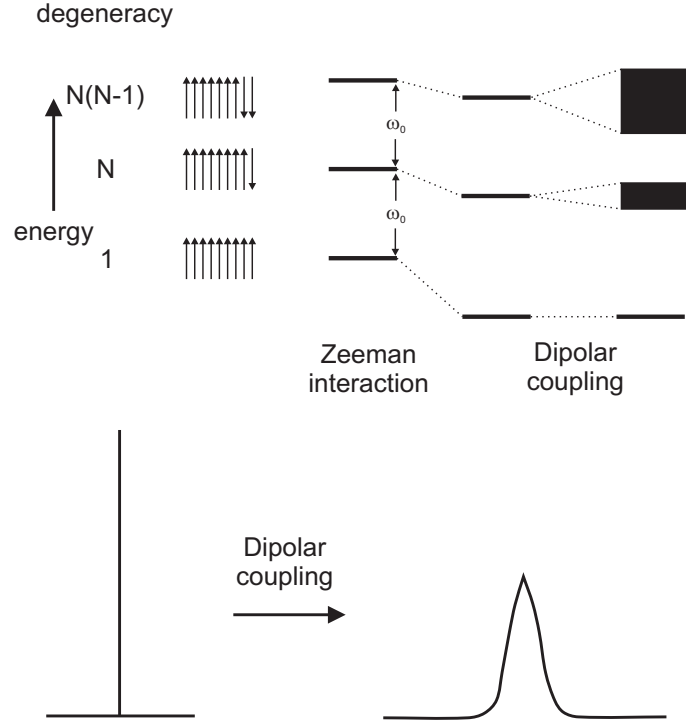


Figure 2.13: Splitting and mixing of degenerate Zeeman levels due to homonuclear dipolar coupling¹⁷

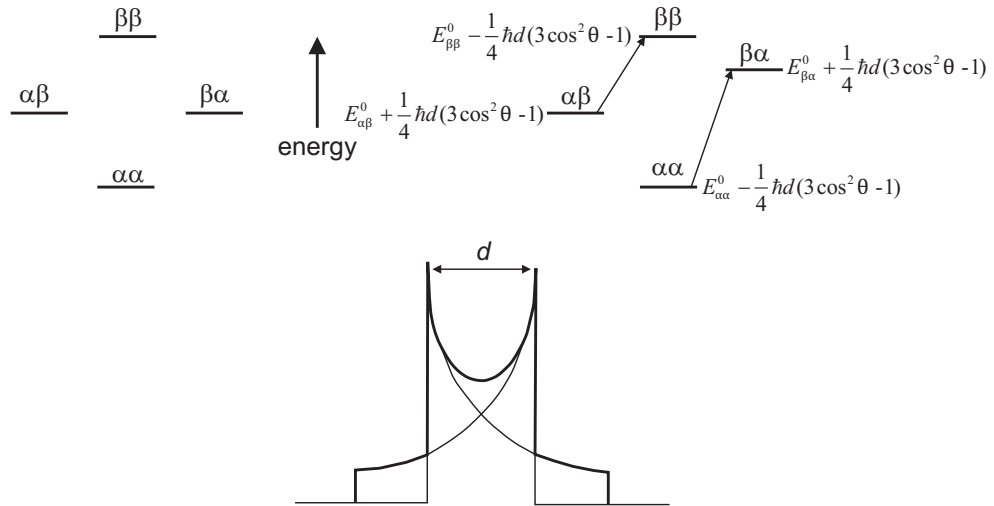


Figure 2.14: Splitting of degenerate Zeemann levels due to heteronuclear dipolar coupling¹⁷

Quadrupolar interaction

A quadrupole can be described as two identical dipoles, arranged with opposite charges.

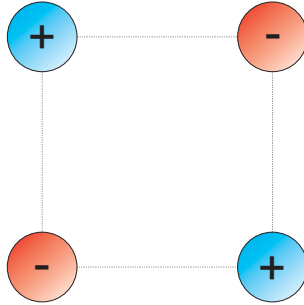


Figure 2.15: Scheme of an electrical quadrupole

All nuclei with a nuclear spin of $I > \frac{1}{2}$ possess such a quadrupole moment. The quantum mechanical operator is represented by the following equation.

$$\hat{H}_Q = \hat{I}_1 \mathbf{Q} \hat{I}_1 \quad (2.29)$$

$$\text{mit } \mathbf{Q} = \frac{eQ}{2I(2I-1)\hbar} \mathbf{V} \quad (2.30)$$

\mathbf{Q} is found to be the quadrupole coupling tensor, comprising the quadrupole moment eQ and the electric field gradient \mathbf{V} . As for dipolar coupling, this effect is averaged by molecular motions in an isotropic solution and so normally only relevant for solid-state NMR spectroscopy. Here the effect plays an important role, since the interaction is strong in most cases, compared to other interactions.

Closing this description of the most important interactions chart 2.2 gives an overview over all interactions together with typical values.

Table 2.2: Overview of common interactions in NMR²⁰

\hat{H}_m	Interaction	Typical size [Hz]	Anisotropy
\hat{H}_Z	Zeeman	$10^7 - 10^9$	
\hat{H}_{RF}	RF	$10^3 - 10^5$	
\hat{H}_D	Dipolar	$10^3 - 10^4$	anisotropic
\hat{H}_{CS}	Chemical Shift	$10^2 - 10^5$	anisotropic / isotropic
\hat{H}_J	Scalar	$1 - 10^3$	isotropic
\hat{H}_P	Paramagnetic	$10^2 - 10^5$	anisotropic / isotropic
\hat{H}_K	Knight Shielding	$10^2 - 10^5$	anisotropic / isotropic
\hat{H}_Q	Quadrupolar	$10^3 - 10^5$	anisotropic

Relaxation

If a sample is allowed to evolve unperturbed for a long time, the initial state of thermodynamic equilibrium will be restored. One can distinguish between two kinds of relaxation: (i) The spin-lattice relaxation T_1 describes the relaxation of the spin populations back to their Boltzmann-distribution values and (ii) the spin-spin relaxation T_2 describing the decay of the single-quantum coherences. $T_{1\rho}$ describes the spin-lattice relaxation in the rotating frame (in presence of an RF field: spin-lock conditions). The difference between T_2 and T_2^* is found in local field inhomogeneities:

$$\frac{1}{T_2^*} = \frac{1}{T_2} + \frac{1}{T_{\text{inhom.}}} = \frac{1}{T_2} + \gamma \Delta B_0 \quad (2.31)$$

where γ is the gyromagnetic ratio and ΔB_0 the difference in strength of the locally varying field. T_2^* can be extracted from the FID or spectrum as the inverse line width characterizing the decay of the FID affected by a local inhomogeneity, while T_2 has to be measured using an echo-sequence, which is shown later. Figure 2.16 shows the typical ranges for the relaxation constants.

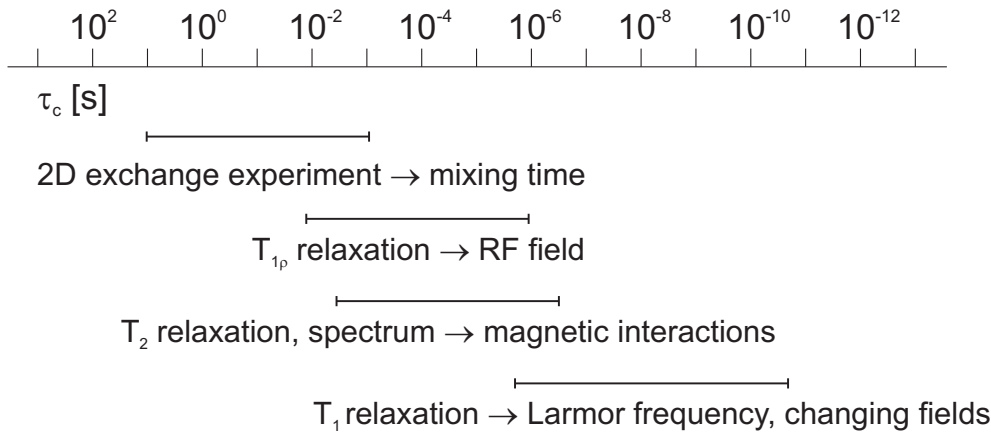


Figure 2.16: NMR time scale for the most common parameters and experiments

Relaxation is mainly caused by fluctuating magnetic fields and molecular motion, modulating the local fields. Sources for such local fields are direct dipole-dipole coupling, CSA, quadrupole coupling, paramagnetic centers or wobbling of the total field. For spin- $\frac{1}{2}$ -nuclei and nuclei with a spin of $I > \frac{1}{2}$ (additional quadrupolar contributions) the influence of the different mechanisms can be classified by their

contribution:

$$(\text{quadrupole}) \gg \text{dipole-dipole} > \text{CSA} > \text{spin-rotation}$$

Pound, Purcell and Bloembergen introduced a model to describe relaxation with respect to a correlation time of the molecular tumbling motion τ_c . In figure 2.17 the different relaxation times are plotted against τ_c , which in turn is inversely proportional to the temperature.

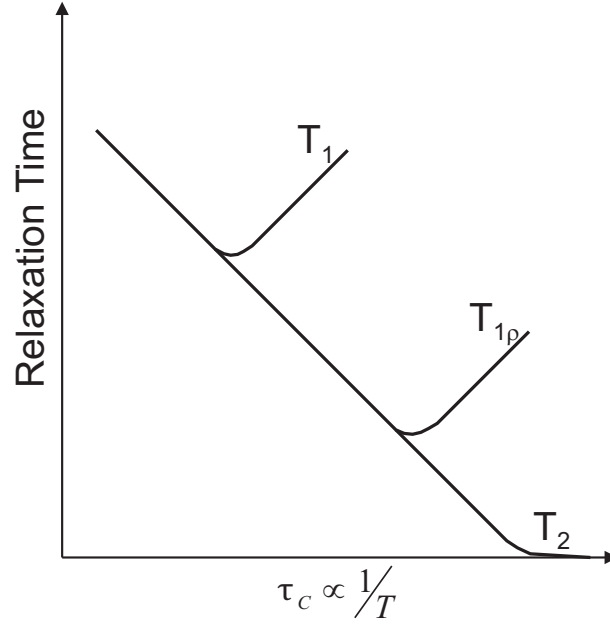


Figure 2.17: The dependency of T_1 , T_2 and $T_{1\rho}$ on the correlation time τ_c

As outlined in chapter 2.1.1 the Bloch equations are used for a phenomenological description. As it will be shown in chapter 2.1.5, they are sufficient to analyze the data, recorded with spin-echo-, inversion-recovery- or saturation-recovery-sequences, to determine the T_1 or T_2 values.

Design of an NMR spectrometer

Figure 2.18 shows a schematic representation of an NMR spectrometer. The central element is a nitrogen and helium cooled superconducting magnet, in which the probe head is located. In the console a constant carrier frequency is produced, e.g. by a crystal oscillator. This carrier frequency is transferred to the transmitter part of the spectrometer. Here the phases are added and the pulse sequence is generated by gating. These low power signals are then transferred to the amplifiers. The amplifiers for liquid NMR normally possess a power of some Watts, while in solid state NMR amplifiers with several 100 Watts are needed. After the amplification the pulses are applied to the sample by an accordingly tuned coil. For the detection of the FID the same coil is used, receiving the FID with an amplitude of some micro-Volts. After the pre-amplification of the signal, still containing the carrier frequency, it is split into two paths and is mixed again with the carrier frequency, with and without a phase shift of 90° , to achieve quadrature detection. These two signals, called real and imaginary part, are then further amplified, digitized and transferred to the console.

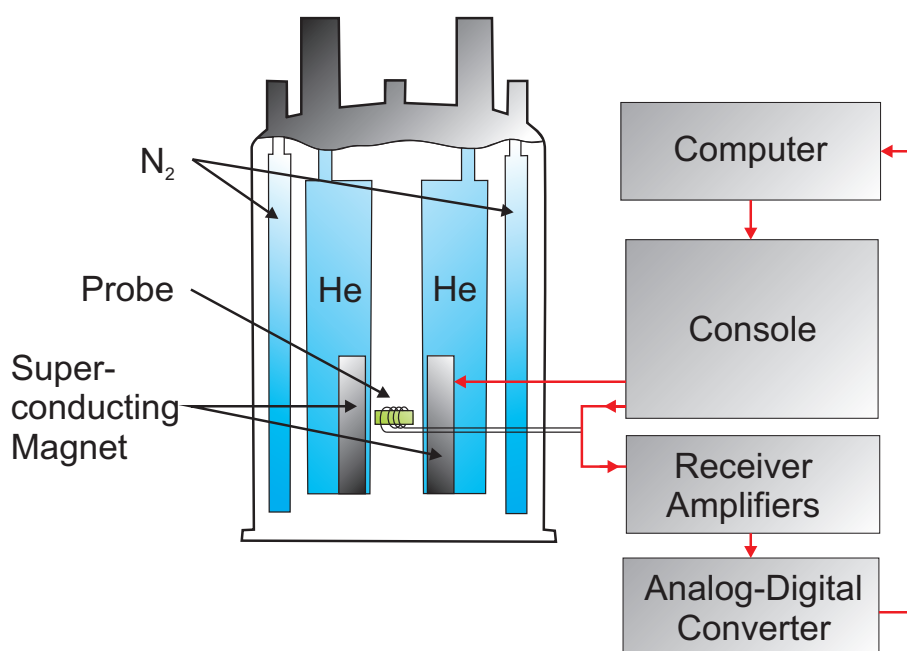


Figure 2.18: Schematic representation of an NMR spectrometer

2.1.4 Decoupling techniques

There are two general approaches to remove unwanted spin interactions. Both are related to rotations, which in a certain way average the effects over time. The first approach, the so called Magic Angle Spinning (MAS), is based on a spatial rotation, while the second method is using RF fields to achieve a spin rotation.

Magic angle Spinning

A look at the Hamiltonians for the different interactions reveals the common term $[3 \cos^2 \theta - 1]$. Here θ is defining the orientation of a tensor describing a certain interaction with respect to the external magnetic field, e.g. CSA, dipolar coupling or quadrupole coupling. In an isotropic solution these effects are averaged by molecular motions which are fast compared to the magnitude of the interactions. In solid-state NMR, for common powder samples, all molecular orientations are statistically distributed. The MAS technique exploits this angular dependency to average the interaction by a fast rotation of the sample about an axis with an angle of 54.74° with respect to the external magnetic field. Therefore, the sample is packed into a cylindrical sample holder, called rotor, with a drive-tip at the bottom. Then the sample is put into a cylindrical hole in the probe head, called stator, which is adjusted to the magic angle of 54.74° (figure 2.19). Then, by use of pressurized air or nitrogen the sample can be rotated at spinning rates, depending on its diameter and the probe. Typical spinning frequencies are found to be in the range of 3 kHz up to over 100 kHz, using rotors with diameters between 15 and 1 mm.



Figure 2.19: Rotors and probe-head used for MAS experiments. The Canadian one penny coin has a diameter of 19 mm.

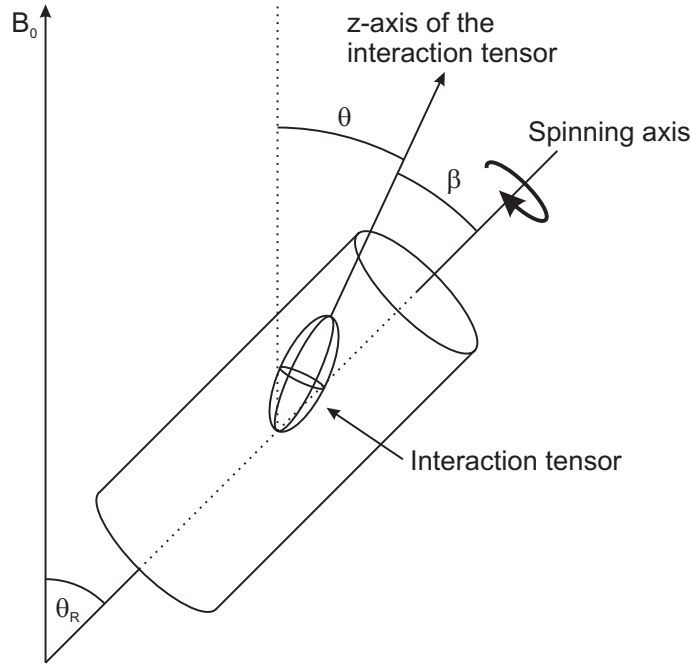


Figure 2.20: Definition of the angles describing the tensors' orientation with respect to the external magnetic field in a MAS experiment

Figure 2.20 shows the rotor positioned at an angle θ_R with respect to the magnetic field. The position of the tensor of an anisotropic interaction then is defined by the two angles θ and β . One can show that for a fast rotation the term $[3 \cos^2 \theta - 1]$ gets dependent on θ_R and β .

$$\langle 3 \cos^2 \theta - 1 \rangle^{\text{Rotation}} = \frac{1}{2} (3 \cos^2 \theta_R - 1) (3 \cos^2 \beta - 1) \quad (2.32)$$

When the sample is rotated exactly at the magic-angle of $54,74^\circ$ the term $(3 \cos^2 \theta_R - 1)$, as well as the term $\langle 3 \cos^2 \theta - 1 \rangle$ are averaged to zero. At this point it is worth mentioning some general rules for MAS:

- The spinning rate has to be high compared to the interaction that one wants to remove.
- The MAS is not always (at low spinning rates) capable of removing the homonuclear interaction due to the mixing of the Zeeman states, which are present in this case.
- The MAS is normally not sufficient for removing quadrupole coupling, since the

angular dependency is more complex, and only first order terms are removed.

When the spinning is not fast compared to the CSA, the formation of spinning side-bands occurs. As shown in figure 2.21 one can see the splitting of the signal with frequency differences equal to the applied spinning rate. At 1 kHz many spinning side-bands are present representing the shape of the CSA. When the spinning rate is increased, the side-bands further spread and decrease in intensity. At 10 kHz only the isotropic chemical shift is left.

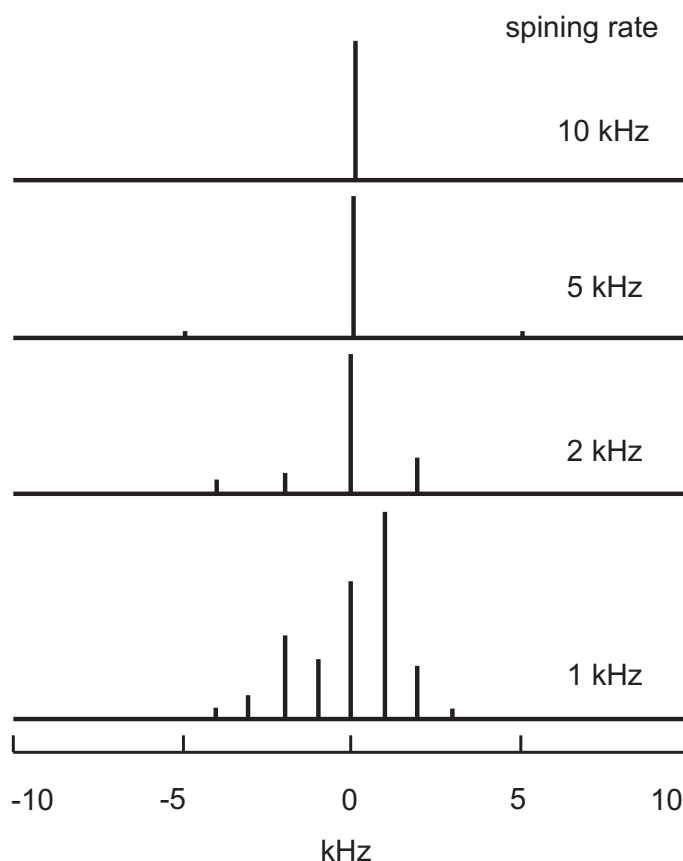


Figure 2.21: Formation of spinning side-bands at different MAS speeds

RF Decoupling

RF decoupling in general aims for the removal of unwanted interactions by applying some kind of RF irradiation. There are two kinds of sequences, multipulse decoupling and decoupling under continuous irradiation. RF decoupling can be further grouped in hetero- and homonuclear decoupling. Typically RF decoupling is used in combination with MAS.

The most simple decoupling approach is the continuous wave decoupling (cw). When recording spectra of the S spin in an I-S-spin system, e.g. ^1H - ^{13}C , the decoupling can be achieved by irradiating the I (^1H) spin continuously during the detection of the spin S (^{13}C). Figure 2.22 sketches the ^1H -decoupling during the ^{13}C -detection. The cross-polarization used to enhance the ^{13}C -signal will be explained later (see chapter 2.1.5). The only parameters affecting the decoupling efficiency of cw-decoupling are the chosen decoupler frequency and the power (amplitude) of the irradiation. While the amplitude is mainly limited by the amplifiers and the probe head, the choice of the frequency can be crucial. However, if the I spins are homonuclear coupled and if the z-component of a certain spin is on resonance, it affects all nearby spins. This means, that the irradiation does essentially not need to be very broad-banded. The continuous irradiation is causing permanent transitions ($\alpha \leftrightarrow \beta$), which in turn is permanently changing the sign of the dipolar coupling. Taking into account that the rate of these transitions is fast compared to the strength of the coupling, the effect will be averaged by this rapid oscillation.

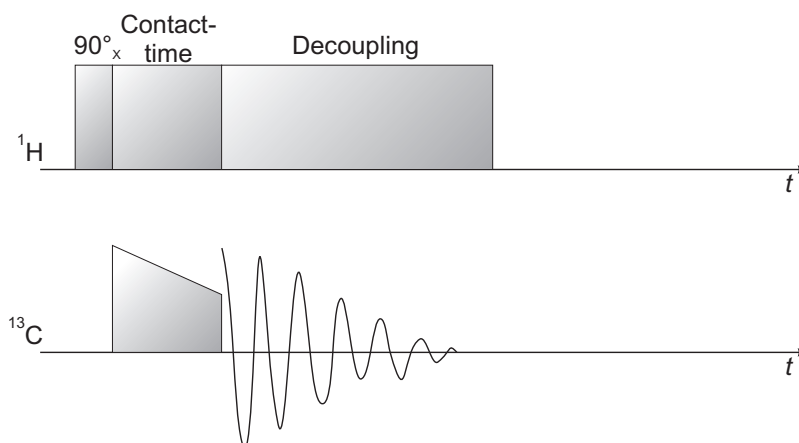


Figure 2.22: ^1H -CW-decoupling during ^{13}C -detection

One approach to further optimize the cw-decoupling is the use of an additional phase alternation. One example, often used for ^1H -decoupling, is the two-pulse phase-modulated (TPPM) decoupling, shown in figure 2.23. The continuous irradiation is separated into blocks and the phase is alternated between ϕ and $\phi + \Delta\phi$. The additional parameters in this sequence are the $\Delta\phi$ and the length of the pulses, which will be discussed later in this thesis (see chapter 3.2). The improvement is caused by an additional averaging of heteronuclear coupling due to the phase alternation. Sequences like this are one option to increase the decoupling performance or to reduce the power needed for sufficient decoupling.

2 Methodological background

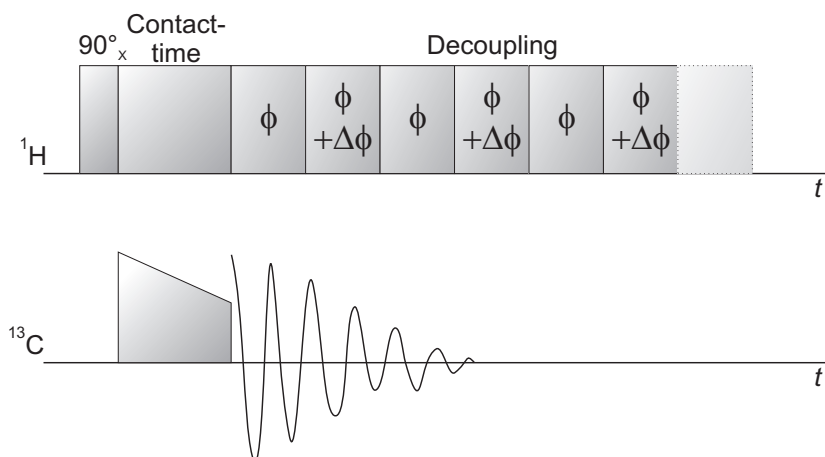


Figure 2.23: ^1H -TPPM-decoupling during ^{13}C -detection

At this point the XY-16 decoupling will be shown as one example for a multi-pulse decoupling technique. Figure 2.24 sketches the sequence, which is a variation of the Carr-Purcell-Meiboom-Gill (CPMG) sequence. During detection the decoupling is achieved by applying rotor-synchronized pulses with pulse lengths τ_R on the coupled spins. The phase-cycling for the pulses consists of 16 elements (x y y x x y y -x -y -y -x -x -y -y -x) and can be further improved by the permutation of this basic element. The 180° -pulses average the CSA and the heteronuclear dipolar coupling. The advantage of this sequence is the broad-banded inversion, due to the use of hard pulses. A major drawback can be the fact that homonuclear coupling is eliminated exclusively by MAS, and for this reason high spinning rates are needed.

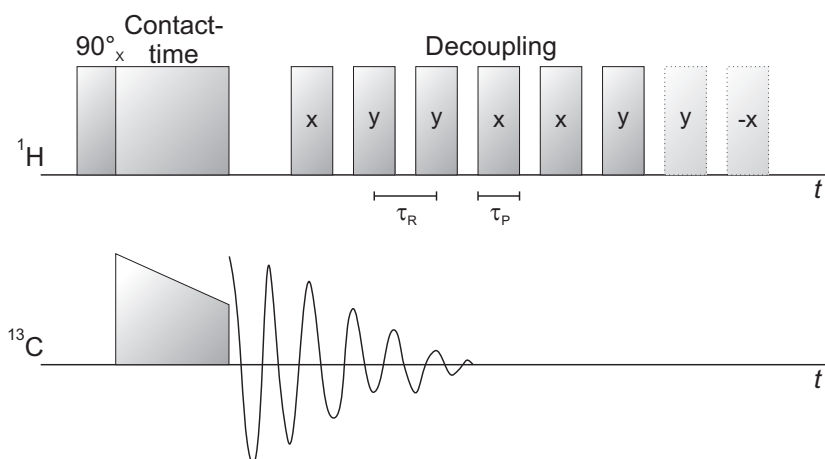


Figure 2.24: ^1H -XY16-decoupling during ^{13}C -detection

The choice of a proper decoupling technique is essential and in most cases not

straight-forward, especially for nuclei with a higher CSA, wider chemical shift distribution or quadrupolar nuclei. This will be briefly discussed for the case of ^{19}F -decoupling in chapter 3.

2.1.5 Common NMR techniques

Single pulse (SP) experiment

As outlined before, in the SP experiment first a 90°_x -pulse is applied directly, followed by the acquisition of the FID.

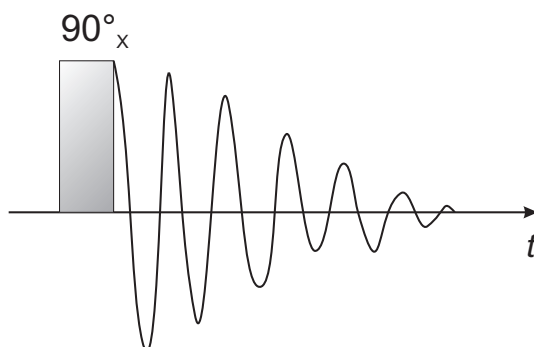


Figure 2.25: Single pulse experiment

Spin-echo experiment

Similar to the SP experiment, first transverse magnetization is generated by a 90° -pulse. But instead of directly starting the acquisition, the system is allowed to evolve for a period τ . Due to local field inhomogeneities the spins start dephasing. After the evolution period τ a 180° -pulse is applied inverting the effect and refocusing all spins after 2τ . The decay of this “echo” is then recorded, which is identical to the normal FID, despite the signal intensity.

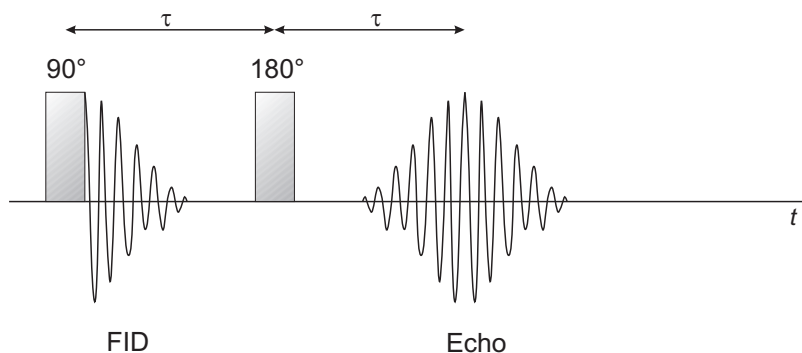


Figure 2.26: Spin-echo experiment

This sequence is commonly used to measure T_2 . The sequence is performed for different τ -values, and by plotting the intensity against 2τ it can be used to determine the exact T_2 , free of any T_2^* contributions. The exponential decay of the

magnetization can be analyzed using formula 2.34, which is a solution of the Bloch equations.

$$\frac{dM_{xy'}}{dt} = -\frac{M_{xy'}}{T_2} \quad (2.33)$$

$$M_{xy'}(\tau) = M_{xy'}(0) \exp(-\tau/T_2) \quad (2.34)$$

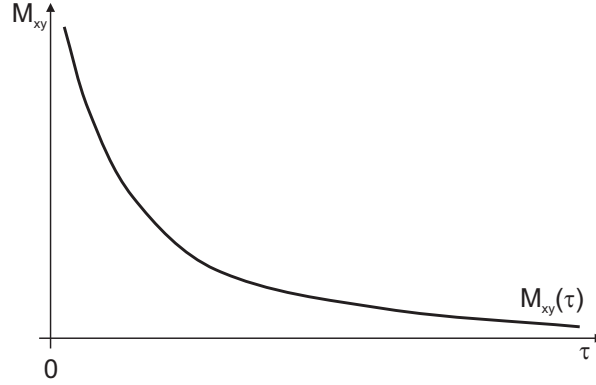


Figure 2.27: Exemplary spin-echo decay curve

Inversion-recovery (IR) experiment

The inversion-recovery sequence is used to measure the spin-lattice relaxation time T_1 . The sequence starts with a 180° -pulse. The equilibrium magnetization is inverted and aligned along the $-z$ -axis. After an evolution period, during which the system is allowed to relax, a 90° -pulse generates a detectable transverse magnetization in the x - y -plane.

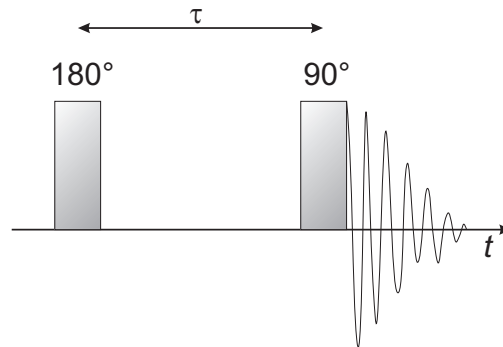


Figure 2.28: Scheme of the inversion-recovery sequence

2 Methodological background

Again the analysis is based on the Bloch equations. The factor of two before the exponential function is added, since the equilibrium magnetization is recovered twice starting from $M_z(0) = -M_{z,eq}$.

$$\frac{dM_z}{dt} = -\frac{M_z - M_0}{T_1} \quad (2.35)$$

$$M_z(\tau) = M_z(0) [1 - 2\exp(-\tau/T_1)] \quad (2.36)$$

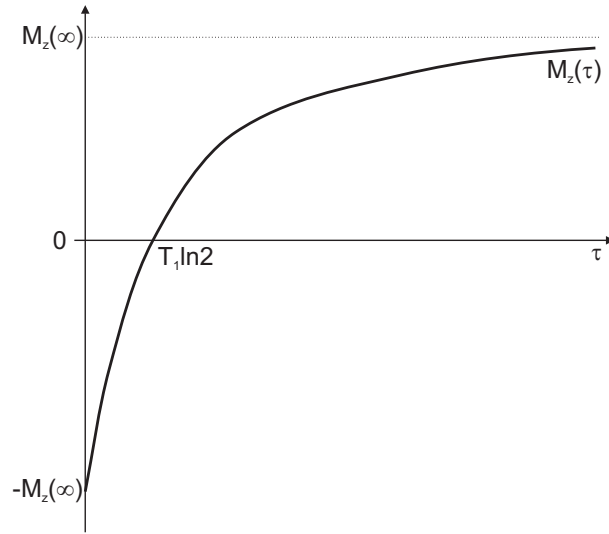


Figure 2.29: Exemplary inversion-recovery curve

Saturation-recovery experiment

The idea of the saturation-recovery sequence is to saturate the system completely in the beginning and then follow the recovery process. The saturation is done by applying a very fast series of 90° -pulses. Then, after an evolution period during which the system is allowed to relax with T_1 , the signal is recorded after a 90° -pulse.

In this case the evolution of the magnetization (figure 2.31) is described by formula 2.38. The advantage of this method is the short experimental repetition time. Since the system is saturated in the very beginning, there is no need to wait for the system to be fully relaxed, when accumulating experiments. For this reason this sequence is commonly used for materials with a very long T_1 .

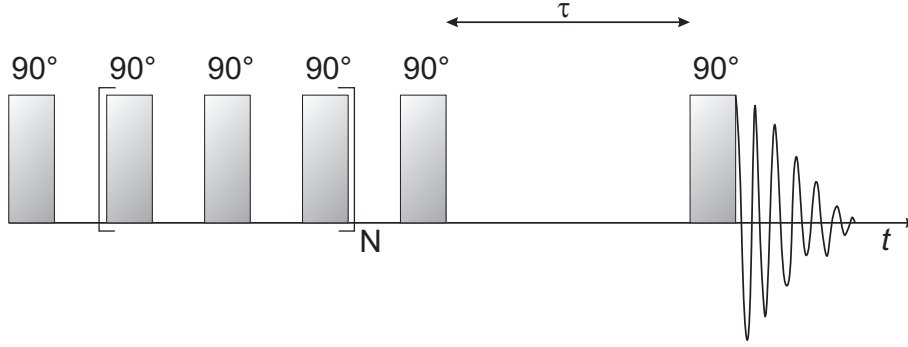


Figure 2.30: Scheme of the saturation-recovery sequence

$$\frac{dM_z}{dt} = -\frac{M_z - M_0}{T_1} \quad (2.37)$$

$$M_z(\tau) = M_z(0) [1 - \exp(-\tau/T_1)] \quad (2.38)$$

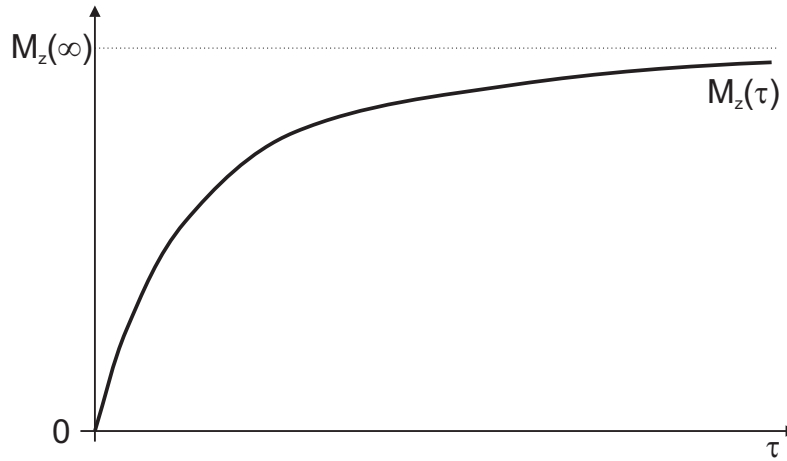


Figure 2.31: Exemplary saturation-recovery curve

Cross-polarization experiment

The CP experiment is one possibility to overcome the problem of low signals for nuclei with low natural abundances, e.g. ^{13}C . The idea of this concept is to produce the magnetization on a nucleus with a high natural abundance, e.g. ^1H or ^{19}F , and transfer the magnetization to the low abundance nucleus. Another reason for using the CP experiment can be a long spin-lattice relaxation time, since for the CP experiment the T_1 of the undetected spin is essential for the choice of the delay

2 Methodological background

between two experiments. The CP sequence is used for a large variety of pairs of nuclei, e.g. ^1H - ^{13}C , ^1H - ^{15}N or ^1H - ^{31}P , while in the following everything will be based on the most common ^1H - ^{13}C -example. Figure 2.32 sketches the CP sequence. It starts with a 90°_x -pulse on the protons to produce magnetization, followed by a contact-time (CT), during which both nuclei are irradiated along the -y-axis. Then the FID of the ^{13}C -nuclei is detected under proton decoupling.

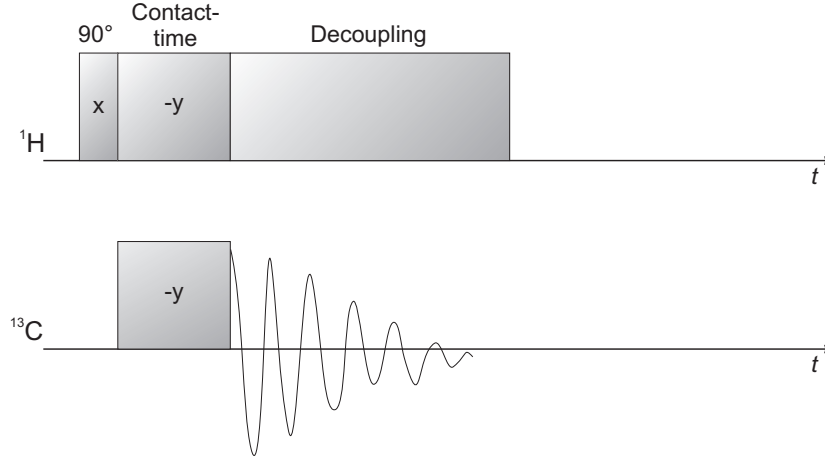
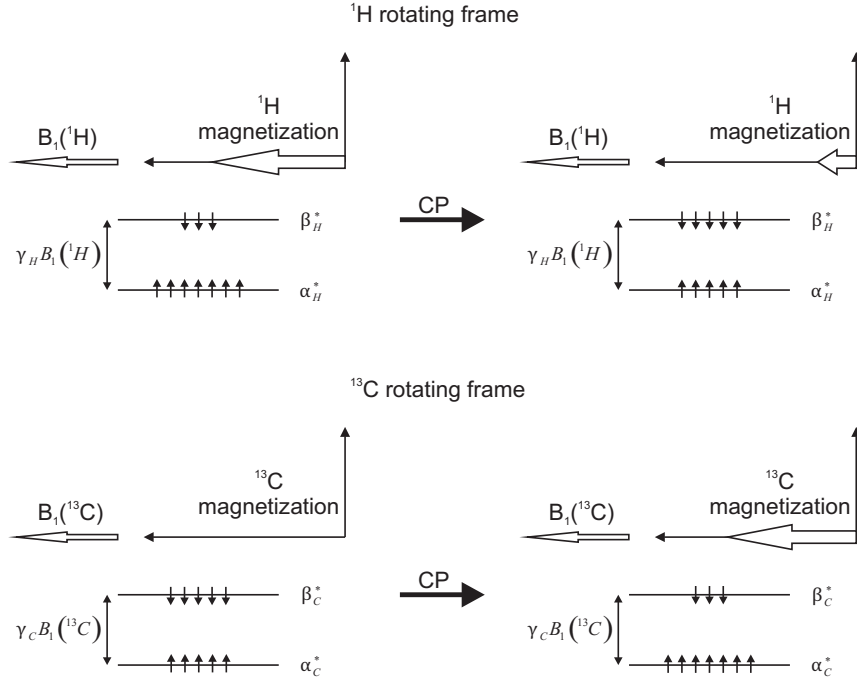


Figure 2.32: CP experiment for a ^1H - ^{13}C spin system

To explain the concept of the CP the problem is transformed to a double rotating frame, in which all the pulses appear static. In other words two rotating frames are introduced, one for the protons, in which all ^1H -pulses appear to be static and one for the ^{13}C , in which all the ^{13}C -pulses appear to be static. Both frames are rotating about B_0 (z-axis in the laboratory frame) with the Larmor frequencies of the ^1H -spins and the ^{13}C -spins, respectively. A scheme for the following explanation is found in figure 2.33. The ^1H 90°_x -pulse generates a transverse magnetization along the -y-axis, before the contact pulse is applied along the -y-axis. This, so-called spin-lock field $B_1(^1\text{H})$, behaves in the protons rotating frame like B_0 in the laboratory frame. If we now assume the simplification that all pulses are on-resonance, the $B_1(^1\text{H})$ is the only field present in the ^1H rotating frame. Now we can define new spin states, arising from quantizations along the $B_1(^1\text{H})$ -axis, α_{H}^* and β_{H}^* . The same is done for the ^{13}C -spins, leading to a field $B_1(^{13}\text{C})$ in the ^{13}C rotating frame and the two spin states α_{C}^* and β_{C}^* . For this "spin system" there is no polarization after the ^1H 90°_x . To get an efficient polarization transfer during the CT the amplitudes of the contact pulses have to fulfill the Hartmann-Hahn (HH) matching condition (equation 2.39).


 Figure 2.33: Scheme for the CP transfer in a ^1H - ^{13}C spin system

$$\gamma_1 \cdot \tilde{B}_1(^1\text{H}) = \gamma_2 \cdot \tilde{B}_1(^{13}\text{C}) \quad (2.39)$$

In this simple model the HH matching conditions make sure that the energy gaps for the spin-states of ^1H and ^{13}C are equal. The actual polarization transfer is caused now by the dipolar coupling between the ^1H - and ^{13}C -spins:

$$\hat{H}_D^{\text{HC}} = - \sum_i d_i \left(3 \cos^2 \theta_i - 1 \right) \hat{I}_{iz}^{\text{H}} \hat{S}_z^{\text{C}} \quad (2.40)$$

where d_i is the dipolar coupling constant for the coupling between the i th ^1H and the considered ^{13}C . Since the rotating frames rotate about the z -axis, both operators I_z and S_z are not affected by the transformation. The dipole-dipole coupling is not able to change the net energy or the net magnetization of the system, since the spins are quantized in directions which are perpendicular to the z -axis. For this reason the clearly present dipolar coupling can affect the spin system only by conserving the net energy and magnetization. If the HH match is obeyed, the energy gap is the same for both kind of nuclei and spin-up transitions ($\beta^* \rightarrow \alpha^*$) for one nucleus

can be compensated by spin-down ($\alpha^* \rightarrow \beta^*$) transitions of the second. Since at the beginning of the CT the magnetization of the protons along the -y-axis was equal to that one along the B_0 -axis before the 90°_x -pulse and the net magnetization of the ^{13}C was zero at this point, the ^1H magnetization is reduced by $\alpha^* \rightarrow \beta^*$ transitions while the ^{13}C magnetization is increased by $\beta^* \rightarrow \alpha^*$ transitions. Not considered in this explanation is the influence of the homonuclear dipolar coupling between the protons, which indeed has a strong influence on the CP-dynamics.

When working under MAS conditions it is common to use the ramped CP sequence (figure 2.34). In the ramped CP sequence one of the contact pulses has a linearly decreasing or increasing amplitude. The reason for this is found in the Hartmann-Hahn condition. For static samples the HH condition regularly is very broad, in other words it is easy to set-up and insensitive to small mis-settings. When spinning a sample, the HH match splits up in more than one possible HH match and the CP efficiency drops. By applying such a ramp it is possible to cover a certain HH match completely and the sequence gets less sensitive to small mis-settings.

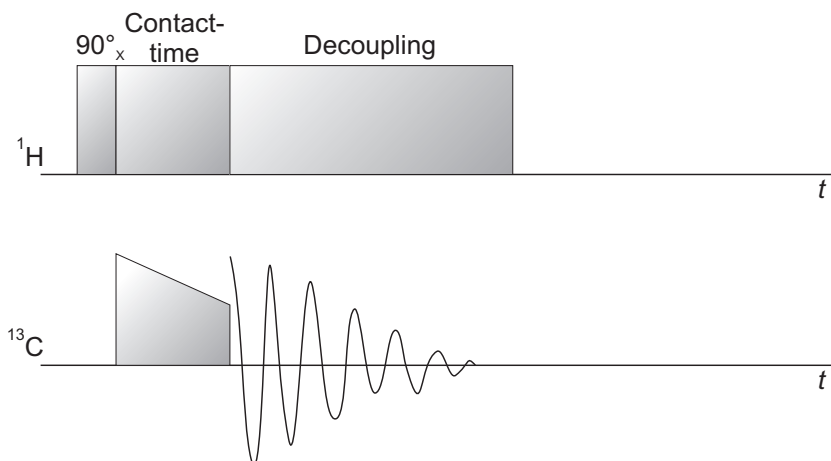


Figure 2.34: Ramped CP experiment for a ^1H - ^{13}C spin system

2.1.6 Experimental parameters

NMR experiments were performed on a Varian InfinityPlus NMR spectrometer operating at ^1H , ^{19}F and ^{13}C NMR frequencies of 399.76 MHz, 376.09 MHz and 100.53 MHz, respectively. If not mentioned differently the NMR spectra were acquired under magic-angle spinning (MAS) conditions using a 4-mm MAS probe at a spinning frequency of 16 kHz with $\pi/2$ pulse lengths which were adjusted to be $5\ \mu\text{s}$. All experiments have been performed at room temperature.

2.2 X-ray structure analysis

2.2.1 Theoretical basis of X-ray diffraction

The X-ray structure analysis is based on the diffraction of X-ray radiation in a crystal lattice. The incidence of radiation on a one dimensional lattice causes interference phenomena (diffraction). One can explain this by assuming that at each point of the lattice a spherical scattered wave is generated. When we look towards the lattice in a certain angle θ , the different waves possess a certain path difference Δ depending on the angle θ and the distance d between two lattice points (figure 2.35). For certain angles θ the path difference Δ is a multiple of the wavelength $n\lambda$. For these angles constructive interference is found, i.e. all scattered waves potentiate to a diffracted beam, whereas n is the diffraction order. $n\frac{\lambda}{2}$ by analogy, leads to destructive interference.

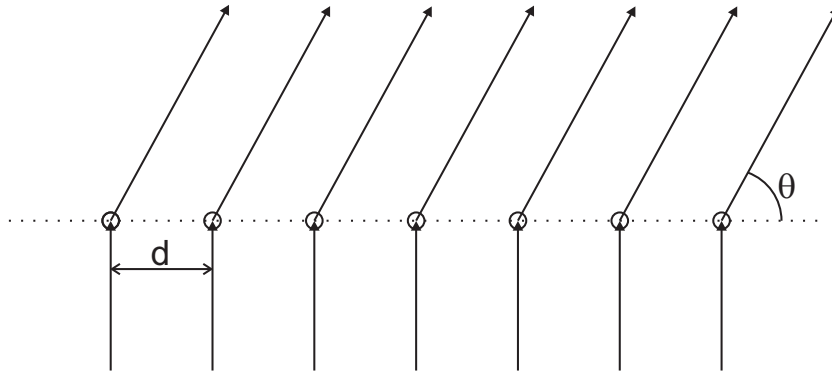


Figure 2.35: Diffraction at a 1D-lattice

The intensities for ranges between $n\lambda$ and $n\frac{\lambda}{2}$ are related to the number of diffraction points. If for example the path difference is found to be $\frac{\lambda}{10}$ and one takes into account 10 diffraction points, wave number 1 and 6 are completely cancelled out. In general n diffraction points are needed to cause destructive interference for a path difference of $\frac{\lambda}{n}$ as sketched in figure 2.36.

Having a look at the particle density and lattice constant for a typical crystalline solid one can see that the number of particles is much higher than needed. For this reason for all areas in which the interference constraint is fulfilled very sharp reflections are expected.

In a crystal, certain atom positions are found periodically in all three directions in space. For one dimension the Laue-equation (equation 2.41) describes the inter-

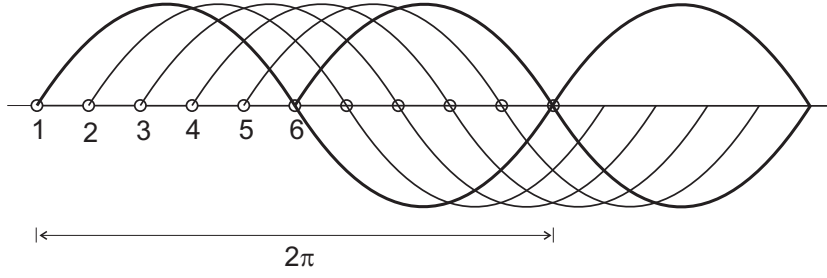


Figure 2.36: Destructive interference of scattered waves for a path difference of $\frac{\lambda}{10}$ ²¹

ference constraint for each order of diffraction n .

$$a \cos \mu_a + a \cos \nu_a = n_1 \lambda \quad (2.41)$$

$$n_1 = 1, 2, 3, \dots$$

$$\mu = \text{Angle of incidence}$$

$$\nu = \text{Emergent angle}$$

$$a = \text{Distance between two particles along the a-axis}$$

According to this equation an angle of incidence μ is related to an emergent angle ν for which a diffracted beam can be observed. Since the wave is spread in the whole space, this is true for all angles of vision on a cone with an opening angle of 2ν (Laue cone) shown in figure 2.37.

For each dimension in space there is a system of such Laue cones. In the general three dimensional situation three Laue cones have to intersect in one common line to cause a reflection for a common angle of incidence and emergence.

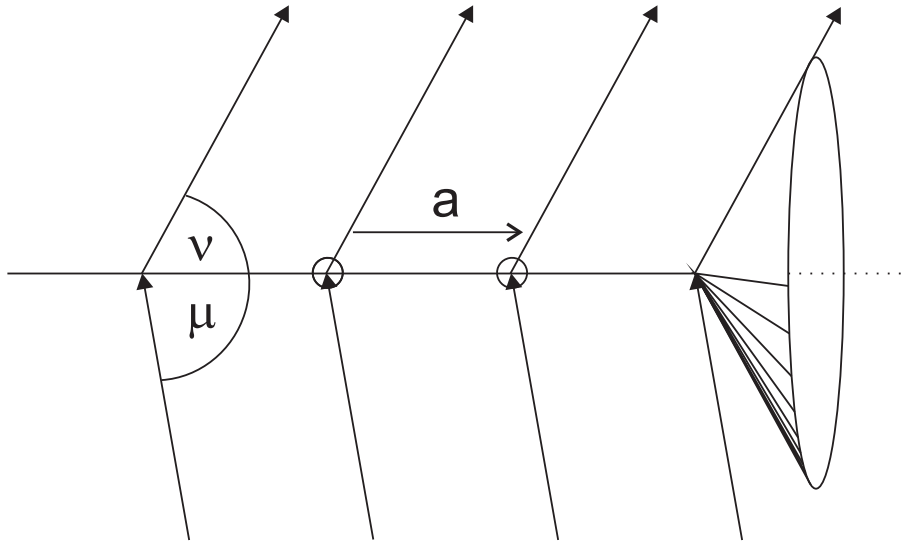
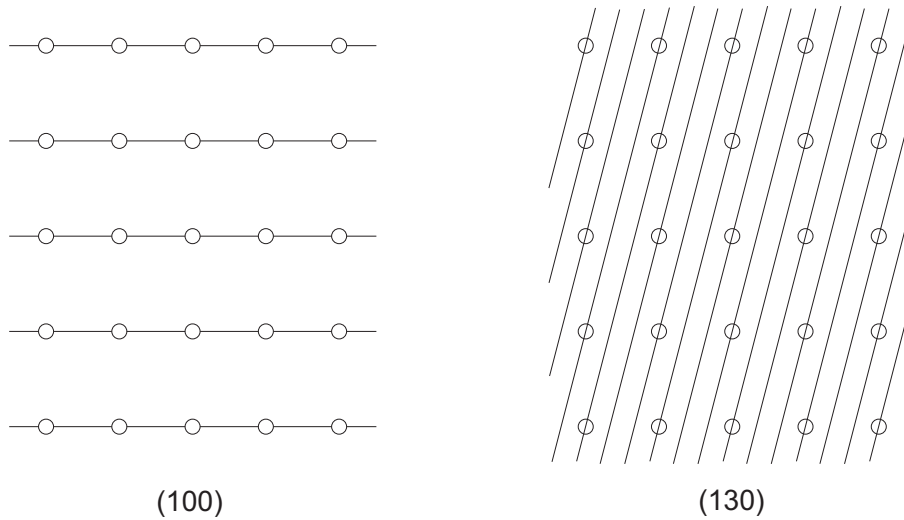
$$a \cos \mu_a + a \cos \nu_a = n_1 \lambda \quad (2.42)$$

$$b \cos \mu_b + b \cos \nu_b = n_2 \lambda \quad (2.43)$$

$$c \cos \mu_c + c \cos \nu_c = n_3 \lambda \quad (2.44)$$

The planes at which the reflections occur are called lattice planes. They are characterized by the hkl -values, the so-called Miller indices. For each plane, built-up by lattice atoms, a series of parallel planes can be found (figure 2.38).

The hkl -values can be determined by taking the plane which is nearest to the

Figure 2.37: Diffraction of a row of atoms²¹Figure 2.38: Example for lattice planes in a crystal²¹

origin and measure the reciprocal axis intercepts $1/h$, $1/k$ and $1/l$ with respect to the a -, b - and c -axis of the unit cell (figure 2.39).

Constructive interference is found if the angle of incidence is equal to the emergent angle and the Laue equations are fulfilled. These constraints can be described by the Bragg equation. The Bragg equation can be derived by the consideration of the path difference to a wave diffracted at the next and lower plane (figure 2.40).

Only for angles which are related to a multiple of the wavelength as the path

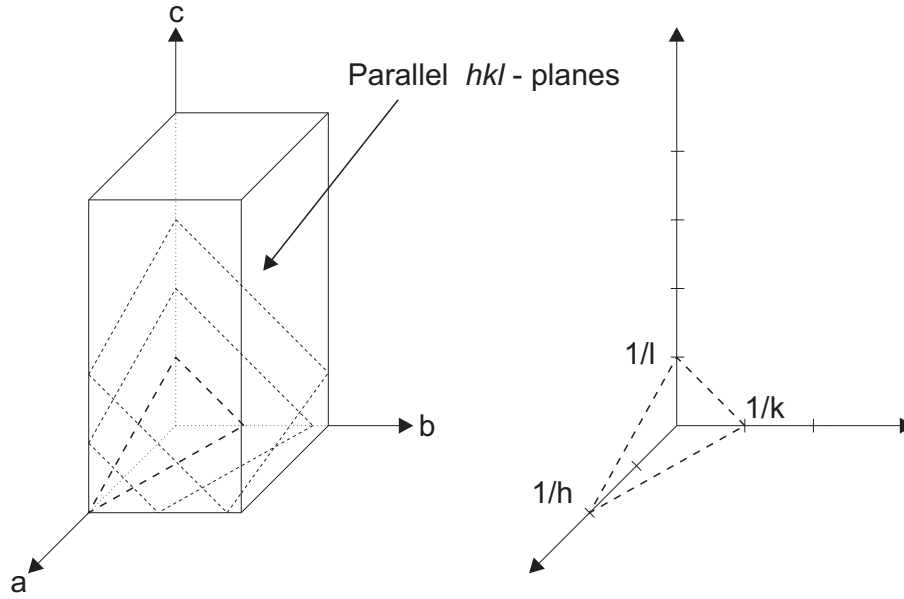


Figure 2.39: Definition of the hkl -values by the reciprocal axis intercepts relative to the unit cell²¹

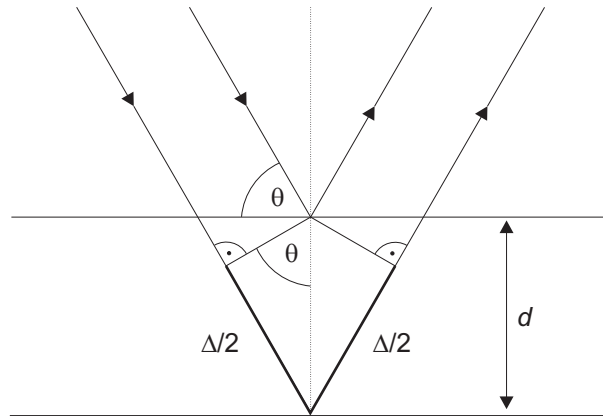


Figure 2.40: Derivation of the Bragg equation²¹

difference, i.e. fulfill equation 2.45, show constructive interference.

$$2d(hkl) \sin \theta = n\lambda \quad (2.45)$$

$$n = 1, 2, 3... \quad (2.46)$$

The X-ray radiation is produced by an X-ray tube. Figure 2.41 sketches the design of such an X-ray tube. In the most simple version it consists of a tungsten heating

coil as cathode and an anode (e.g. copper). At around 200° C the cathode emits electrons which are accelerated by a difference of potential to hit the anode with high speed.

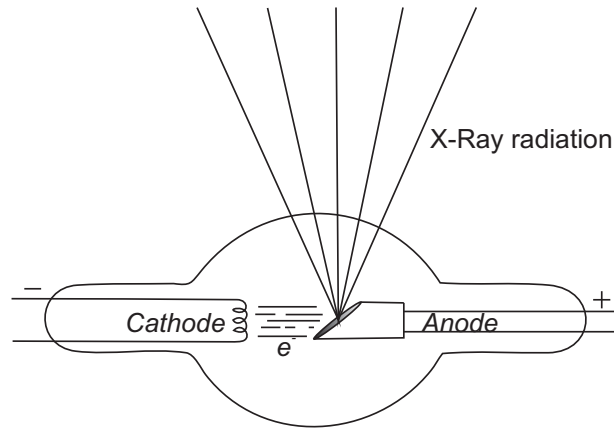


Figure 2.41: Scheme of an X-ray tube

Electrons with an adequate speed can kick out an electron from the K- or L-shell. The electron gap is then filled by an electron of a higher shell and the energy difference is emitted as X-ray radiation.

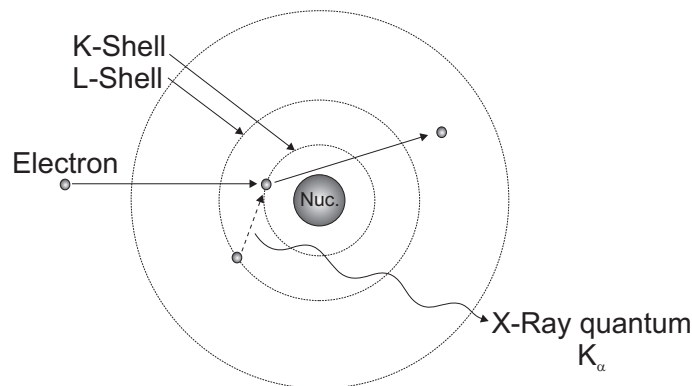


Figure 2.42: Formation of X-ray radiation

The possible energies which are dependent on the shell from which the electron was taken out are K_n and L_n . In the case of elements with a high atomic number, electrons from different shells with higher energies can be used to fill the gap, defined by the index n (α , β , ...). In addition to this element-specific radiation, a broad continuous background which is dependent on the potential difference is present (figure 2.43). This Bremsstrahlung is caused by a deceleration of electrons passing the

2 Methodological background

metal, since all accelerated (or decelerated) charged particles irradiate electromagnetic radiation. This part of the radiation is dependent on the acceleration current. The lowest wavelength is not dependent on the acceleration current and equal to the energy which is passed to a single photon which consumes all kinetic energy.

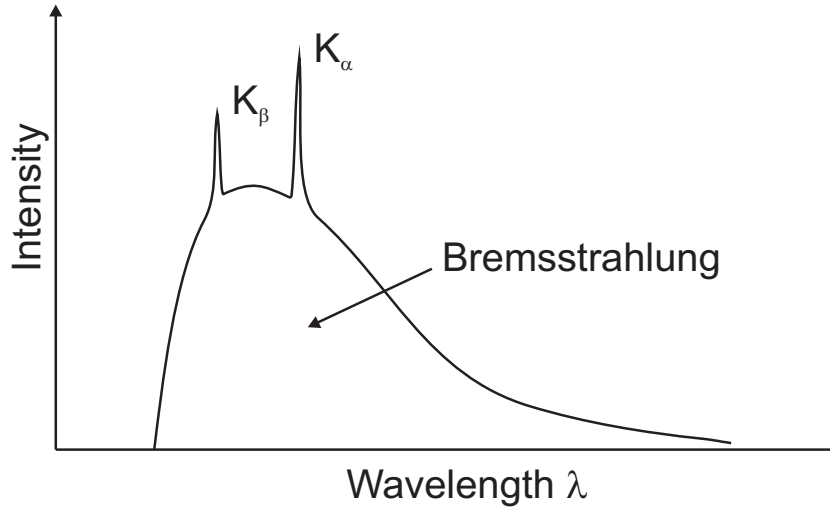


Figure 2.43: Typical X-ray spectrum

For a single crystal it is normally possible to solve the structure by the use of between 1000 and 50000 reflections. Each lattice plane (hkl) related to a certain reflection has a certain orientation in the crystal. For this reason it is necessary to move the crystal's orientation mechanically. In figure 2.44 a four-circle-diffractometer with a "kappa-circle" geometry is shown as an example. In this geometry the X-ray source and the centre of the crystal are fixed and the crystal can be moved along three axes to record different reflections on the detector plate.

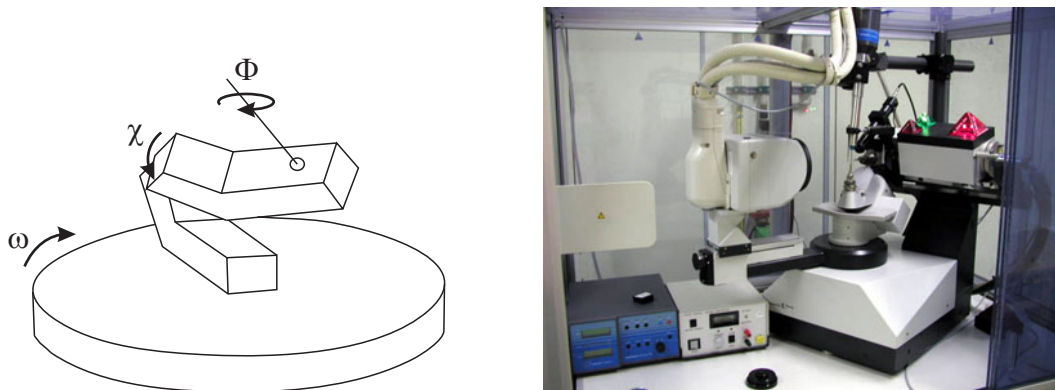


Figure 2.44: Example for a four-circle-diffractometer with "kappa-circle" geometry

If a single crystal is not available, e.g. the sample is nano-crystalline, the single crystal diffraction is not applicable. In this case powder diffraction is used to record a diffractogram. Figure 2.45 shows a powder diffractometer with Bragg-Brentano-Geometry.

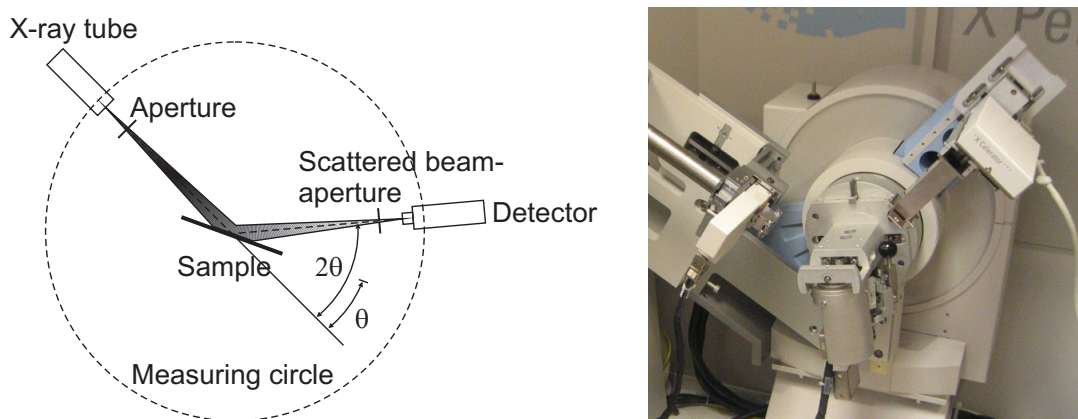


Figure 2.45: Bragg-Brentano-Geometry and an example for a powder diffractometer

The powder is positioned on the sample table which is situated exactly in the center of the measuring circle and in this way in the focal point of the X-ray source. The detector is fixed, while the sample table and the X-ray tube move radially in the ratio 1:2. In this way the Bragg constraint is permanently fulfilled. For this reason the intensities of powder diffractograms are always plotted against the angle 2θ .

To get information out of a recorded diffractogram one has to solve the crystal structure, i.e. find a structure related to the measured reflections. Solving a crystal structure can be separated in three steps:

- Determination of the unit cell and the crystal symmetry (Assignment of a space group)
- Solving the structure
- Refinement of the structure

For the determination of the unit cell only the position of the diffraction maxima are of interest. The intensities are needed for the determination of the symmetry and to solve and refine the structure. After ascertaining the unit cell and the crystal symmetry, the first goal of the structure determination is to find a rough solution

for the crystal structure without assigning certain atoms to certain positions in the lattice. When a certain quality of structure determination is achieved, the structure model can be refined by comparing the model with the experimental diffraction data. Refining the structure for powder samples is routinely possible with modern methods (e.g. the Rietveld method), while solving the structure is found to be a bigger challenge for powder samples. The reason for this is a loss of spatial information, since the data is compressed in one dimension. This effect leads to the loss of the intensities for some diffractions caused by the overlapping of signals. If the powder diffraction is only used to identify a known structure, the diffraction data is compared to values found in databases (e.g. ICDD database).

The next paragraph will give a brief description about diffraction line profile analysis (LPA).²² An expression to describe the length parameter was found already in 1918 and the models have been further improved and extended since then.²³ A common step in many approaches is the adjustment of a certain parameter to adopt a profile which describes the measured line profile. For this reason the first step is often the separation of different contributions of different peaks in a powder pattern. One example for this can be the use of the Scherrer equation to analyse the broadening of a reflection with respect to the crystallite size.²⁴ The most significant draw-back of this method is the need to remove additional contributions, like instrumental effects.

Another option to interpret powder diffractograms is an approach which is referred to as profile modelling. This approach is based on a physical model of the microstructure, taking into account parameters like crystallite size and shape, lattice defect type, density and distribution. In this procedure, which is called Whole Powder Pattern Modelling (WPPM), the powder pattern is reproduced by a direct optimisation of the physical parameters, as mentioned before. While the LPA method could be described as a top-down approach, the WPPM can be seen as a bottom-up approach.²² In contrast to the methods mentioned before, in this case the full powder pattern is fitted by variation of only a few physical parameters, also reproducing unwanted effects, e.g. instrumental characteristics.

2.2.2 Whole Powder Pattern Modelling with PM2K

One possibility to perform WPPM, is the use of the software PM2K.²⁵ The software is based on a physical model for the line profiles which will be presented in a basic manner in the following paragraph.

$$I(s) = I^{IP}(s) \otimes I^S(s) \otimes I^{IP}(s) \otimes I^F(s) \otimes I^{APB}(s) \otimes I^C(s) \otimes I^{GRS}(s) \otimes \dots \quad (2.47)$$

Where s is the reciprocal space variable (equal to $2\sin\Theta/\lambda$, Θ and λ are the diffraction angle and X-ray wave length, respectively), IP the instrumental profile, S the coherent scattering domain size/shape, D the lattice distortions (e.g. dislocation), F the faulting, APB the anti-phase domain boundaries, C the composition fluctuation and GRS the grain surface relaxation. The most important effects, which can influence the modelled powder pattern are explained briefly in the following.

Domain size/shape The most important source of line broadening can be the small size of the coherent scattering regions, i.e. crystallites, and is inversely proportional to the FWHM.²² The implemented simple and relatively robust models are based on shapes with a two-parameter size distribution, i.e. the two parameters mean (ν) and variance (σ). In the PM2K software one can choose different crystallite shapes and distributions.

Lattice defects In many samples the consideration of the crystallite size alone cannot explain the measured line broadening. One effect which leads to an additional line broadening can be a lattice deformation induced by defects (micro strain). These dislocations can be caused by non-perfect growth processes or by mechanically induced plastic deformations. The parameters to optimize are the average dislocation density (ρ), the effective cut-off radius of the dislocation strain field (R_e) and the type of dislocation, which is described by an edge/screw fraction or character (f_e). Furthermore the lattice parameter is reduced in nanoparticles, in particular near the surface.

Various contributions In addition to the contributions described above, the instrumental profile has to be taken into account which is determined by the powder pattern of a standard compound. Also parameters for the peak intensities,

2 Methodological background

the background polynomial and the specimen displacement from the goniometer axis have to be considered, even if they do not directly affect the profile determination.

Figure 2.46 and 2.47 show an example for the modelling of a powder pattern recorded for a ball-milled α -iron alloy with the PM2K software under consideration of the six structure/microstructure parameters: $a_0, \rho, R_e, f_E, \nu, \sigma$.^{22,26}

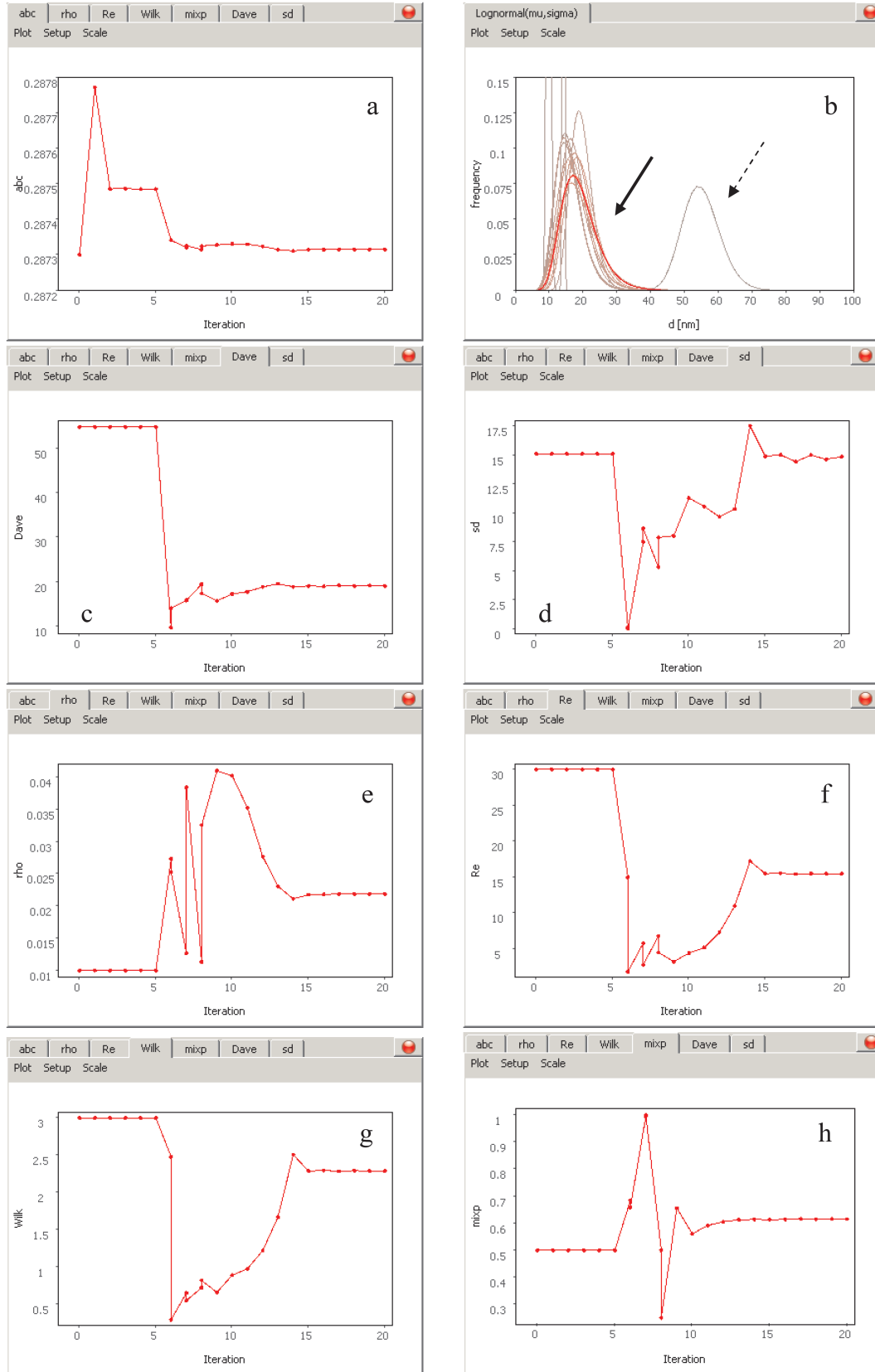


Figure 2.46: PM2K results for a ball milled α -iron alloy^{22,26}. For description see figure 2.47.

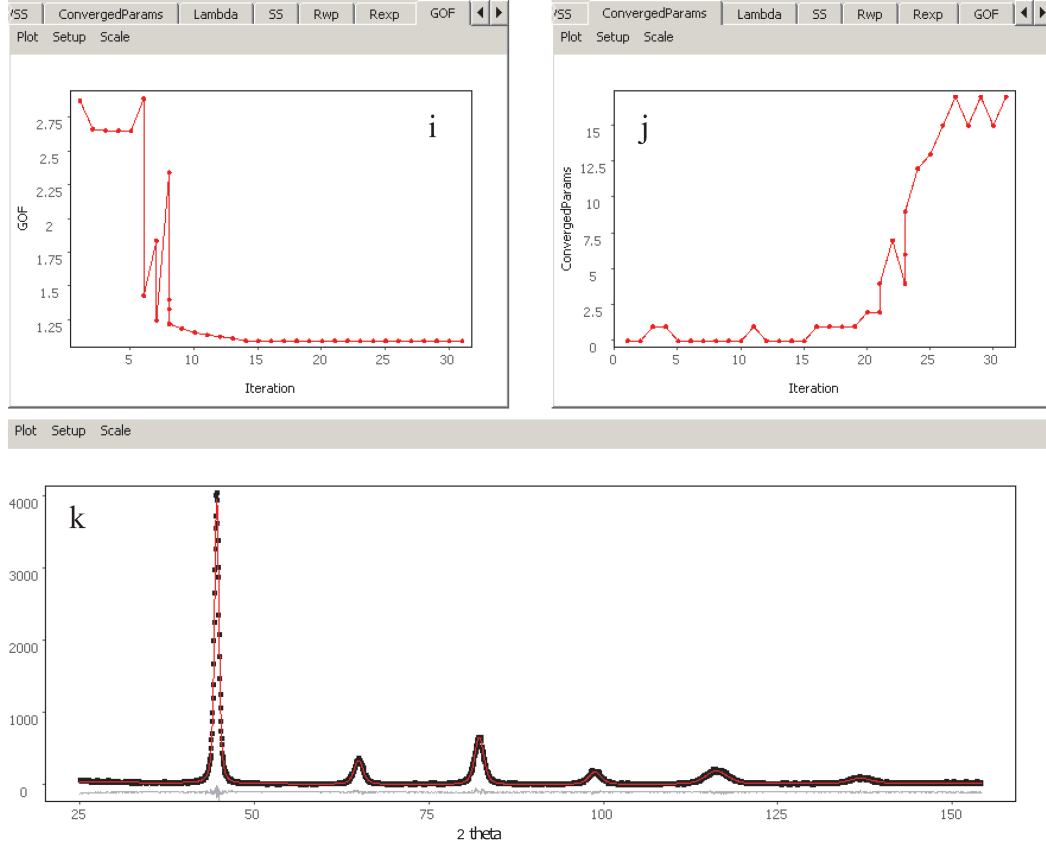


Figure 2.47: (continued). Trend toward convergence of unit cell parameter (a), mean diameter of spherical domains (c), standard deviation of the lognormal distribution of diameters (d), a dash arrow indicates the starting distribution, whereas the result is pointed by a full arrow. Mean dislocation density (e), effective outer cut-off radius (f), Wilkens parameter (g), edge fraction (h), Goodness of Fit (GoF) (i), number of parameters to convergence (all 17 after 26 iterations) (j), experimental data (dot) and modelling result (line) and their difference (residual, line below) (k). Some parameters have been kept constant for the first five iterations, during which only peak intensities, background coefficients and unit cell parameter were allowed to change.^{22,26}

3 Optimized ^{19}F decoupling techniques for fluorinated membranes

3.1 Introduction

A major issue in solid-state NMR is the reduction of line-broadening caused by the anisotropic effects present in a solid sample. While the contribution of the chemical shift anisotropy can be removed mainly by the magic angle spinning technique, which was briefly described in chapter 2.1.4, the broadening arising from the heteronuclear dipolar interaction is typically removed by heteronuclear decoupling, e.g. multi-pulse decoupling schemes described in chapter 2.1.4. Beginning from the basic continuous wave decoupling (cw) in the last decades numerous decoupling methods have been described in literature, e.g. TPPM⁵, XiX²⁷, SPINAL²⁸ or XY-16²⁹. As outlined in chapter 2.1.4, these decoupling techniques can be divided into two general groups, sequences using continuous irradiation to achieve decoupling (e.g. cw-, TPPM- or XiX-decoupling), and multi-pulse decoupling schemes which are based on isolated pulses (e.g. SPINAL or XY-16). All these sequences were developed, optimized and compared mainly with the focus on proton containing systems.³⁰

Another abundant nucleus with a high γ and natural abundance is fluorine. ^{19}F containing substances can be found in many materials which are in the focus of research due to their interesting properties. For example, because of their high proton conductivity and their promising mechanical properties perfluorinated membranes have been in the focus of research in the last few years and found application in fuel cells and all kinds of electrochemical devices.^{31,32} The commercially available perfluorinated membrane Nafion[®] has been in the focus of many ^{19}F and ^{13}C NMR studies, and it was possible to gather interesting information about its structure, structural dynamics^{33–35}.

3 Optimized ^{19}F decoupling techniques for fluorinated membranes

In general ^{19}F -NMR can be a powerful tool to investigate structural and dynamic properties on a molecular scale.^{36,37} Nevertheless, to get high quality and well resolved ^{13}C NMR spectra of fluorine containing samples, e.g. perfluorinated membranes, the use of a proper ^{19}F decoupling technique is unavoidable. ^{19}F decoupling is a larger challenge than the rather easy to handle ^1H decoupling, since the CSA is considerably larger and the range of chemical shifts covers a wider area (-200 ppm up to 200 ppm). The spinning rate needed to fully remove the effects of the CSA, correlates with the value found for the CSA of the system. While for the proton case this condition is normally already obeyed at rather low spinning rates, for fluorine containing samples one normally has to handle the still present spinning side-bands for ^{19}F . Another problem arises from the higher dispersion of the isotropic chemical shifts, as mentioned before, since when performing decoupling the choice of the correct decoupling frequency for this reason is more complicated. For proton systems normally both effects are no big issue and setting the decoupling frequency with respect to the frequencies of the isotropic chemical shifts is sufficient in most of the cases. The same is not true in general for ^{19}F decoupling. Taking this into account, it is not surprising that the analysis of different approaches for fluorine decoupling deviate from results found for the decoupling of protons.

S.F. Liu and K. Schmidt-Rohr were able to show the capability of a rotor synchronized XY-16 sequence to achieve highly resolved ^{13}C spectra, as found for the PTFE signal shown in figure 3.1d recorded at a spinning rate of 25 kHz under XY-16 decoupling, revealing a FWHM of 14.4 Hz. It seems that the XY-16 multi-pulse decoupling is able to offer an effective ^{19}F decoupling under the condition of rather high spinning rates $\nu_r > 25$ kHz, while the power fed to the sample is minimized by the use of a multi-pulse decoupling technique instead of a sequence based on a continuous irradiation.⁸

Based on these results I will further investigate the conditions, under which the XY-16 sequence can or has to be used with respect to parameters like the spinning rate or the decoupling frequency offset. Another objective will be the attempt to adopt other decoupling sequences known from the use in proton containing systems. The most widely used sequence, combining cw irradiation and phase modulation, is the Two Pulse Phase Modulation (TPPM) decoupling scheme.⁵ The TPPM sequence consists of two repeated pulses with a fixed flip angle near π and a phase difference of typically 10° - 70° . A scheme of the sequence can be found in figure 3.2b. In a recent publication the performances of two TPPM related decoupling sequences

were compared for an organic fluorinated compound, namely frequency-swept TPPM and SPINAL.³⁸ An alternative to the TPPM scheme is the XiX sequence, also based on continuously repeated pulses with a phase shift of 180° .^{6,7} After evaluating the potential of this alternative decoupling scheme, a detailed analysis will provide information about the characteristics and experimental conditions of the technique.

3.2 Results and Discussion

In the following results will be shown comparing the different decoupling approaches used for the recording of highly resolved ^{13}C NMR spectra of fluorinated polymers. For optimization and comparison we mainly recorded spectra for a Polytetrafluoroethylen (PTFE) sample, but also verified the results for a commercially available Nafion[®] sample. Figure 3.1a shows the $^{13}\text{C} \{^{19}\text{F}\}$ NMR spectra recorded under high power continuous wave decoupling at spinning rate of 25 kHz. The incomplete decoupling, also described in the publication of S.F. Liu and K. Schmidt-Rohr⁸, leads to a FWHM of ~ 340 Hz with over 1.4 kHz broad resonance features. As discussed in literature, the reason for this is the, compared to protons, much larger CSA for ^{19}F which leads to incomplete excitation of the ^{19}F spins.

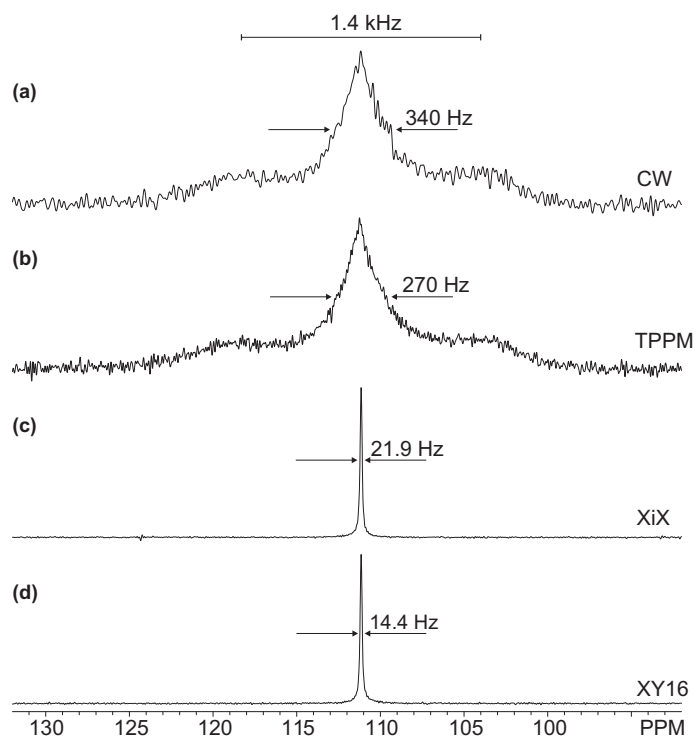


Figure 3.1: Comparison of different ^{19}F decoupling methods applied to PTFE at MAS of 25 kHz. (a) cw-decoupling with a power of 100 kHz (b) TPPM with a flip angle of 15° and a pulse width of 170° (c) optimized XiX (d) optimized XY-16

To achieve optimum performance for the TPPM decoupling sequence, the pulse width and the flip angle were optimized for PTFE by changing them independently from 150° to 210° and 5° to 80° , respectively. The optimization revealed best performance for the TPPM sequence at a pulse width of 170° and a flip angle of 15° . These values are comparable to those normally found for proton decoupling.⁵ Nevertheless, the use of optimized TPPM decoupling cannot provide sufficient decoupling and reveals the same very broad pattern as found for continuous wave decoupling, while the central signal width is reduced to ~ 270 Hz (figure 3.1b). The small superiority of TPPM over cw decoupling can be explained by the additional averaging of the heteronuclear dipolar coupling, but it seems neither to be capable to average the strong ^{13}C - ^{19}F dipolar coupling, nor to eliminate the high CSA present in perfluorinated materials.³⁹

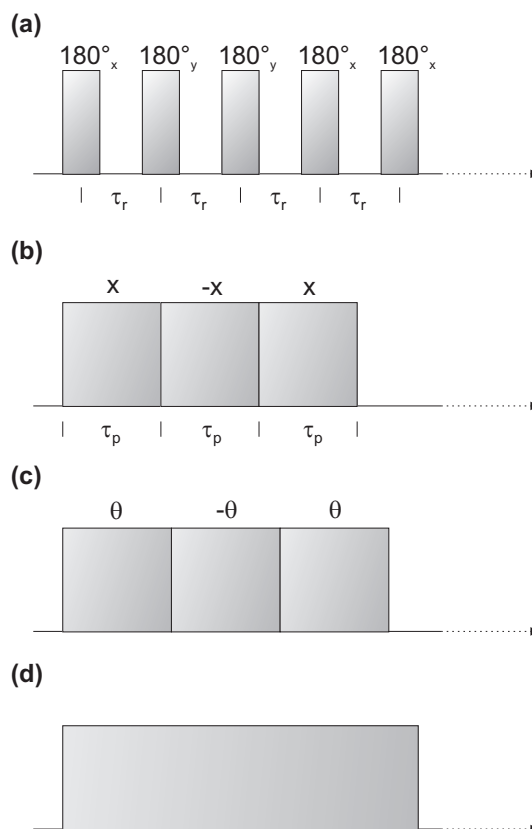


Figure 3.2: Schemes for the (a) XY-16, (b) XiX, (c) TPPM and (d) cw decoupling sequences

As mentioned in the introduction S.F. Liu and K. Schmidt-Rohr were able to show the capability of a rotor synchronized XY-16 sequence to achieve highly resolved ^{13}C spectra, also found for the PTFE signal shown in figure 3.1d recorded at spinning

rate of 25 kHz under XY-16 decoupling, revealing a FWHM of 14.4 Hz. First attempts showed that at the same spinning rate the use of XiX decoupling, presented later in this work, also leads to a good decoupling performance and can reduce the line width to 21.9 Hz. The corresponding spectrum is shown in figure 3.1c. The XiX sequence at this point at least seems to be an alternative to XY-16 and can even overcome the performance of XY-16 under certain conditions, which will be carefully discussed later in the text. To get a comprehensive understanding of the different sequence characteristics, it is needed to examine the sequences with respect to all common experimental parameters. In the following, we will show results recorded at different spinning rates, changing the decoupling frequency offset and all specific parameters for the respective sequences.

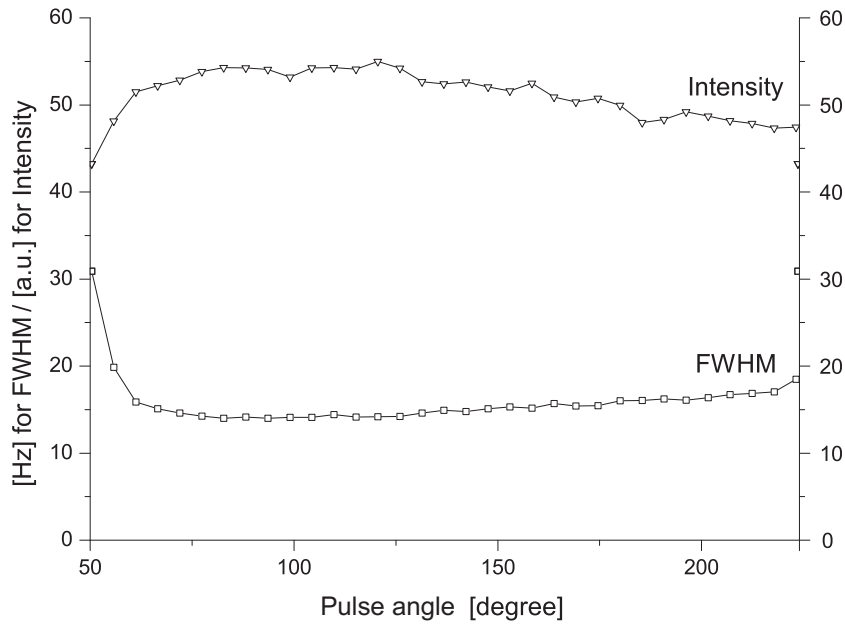


Figure 3.3: Decoupling performance on PTFE for XY-16 in dependence of the pulse width at a MAS frequency of 25 kHz

Figure 3.2a sketches the XY-16 decoupling scheme, applying a 180° pulse after each rotor period, repeating a phase cycle containing 16 elements (x y y x x y y x -x -y -y -x -x -y -y -x). When applying the XY-16 sequence to a spin system, the rotor synchronized pulses average the contributions of the CSA and the heteronuclear dipolar coupling since they change permanently the sign of the interaction, acting on the S_z spin operator present in the Hamiltonian for the CSA (2.21) and the heteronuclear dipolar interaction (2.28). The homonuclear interactions are exclusively eliminated by the magic angle spinning. The reason for this is the term present

in expression 2.26 that mixes the spin states, as discussed in chapter 2.1.3.²⁹ Since the decoupling pulses are rotor synchronized, the only two improvable parameters are the decoupling frequency offset relative to the isotropic chemical shift and the length of the pulses, normally set to 180° . Figure 3.3 visualizes the dependencies of the FWHM and the signal intensity of XY-16 on the pulse width. The changes in the signal intensity and signal width are negligible for a wide range of pulse widths. Only for very short pulses below 75° the FWHM and signal intensity change significantly to larger and smaller values, respectively. A broad optimum is found to be around 100° . So the efforts of optimizing this parameter can be kept minimal, or rather a pulse length of 100° can be used without further optimization. In this way, it can also be shown that the decoupling scheme performance is not sensitive to rf-field inhomogeneities, which can be seen as a local change or instability of the pulse width.

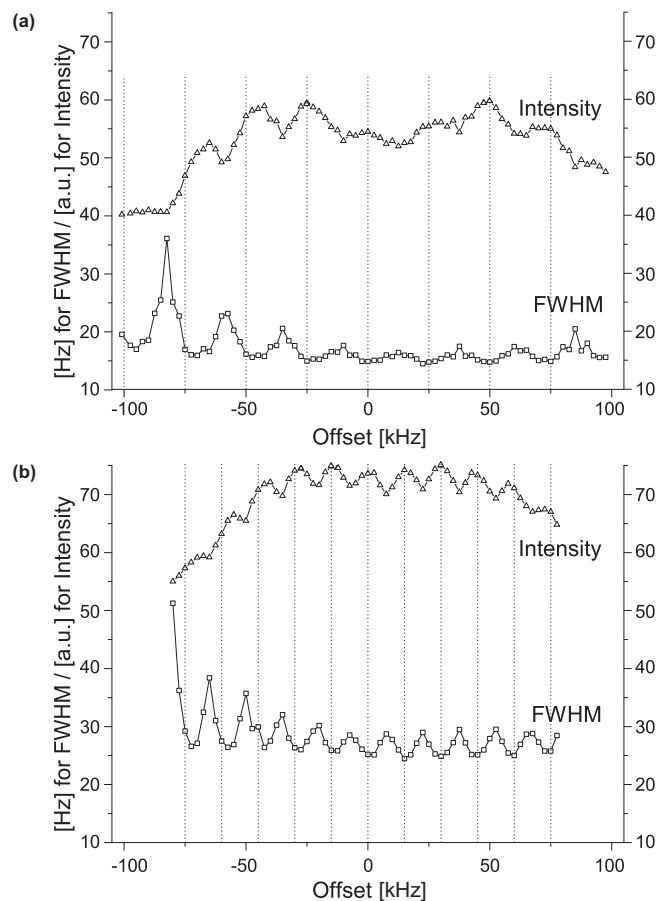


Figure 3.4: Offset characteristics of XY-16 shown for PTFE spectra recorded at (a) 25 kHz and (b) 15 kHz

However, changing the decoupling frequency offset relative to the isotropic chemical shift strongly affects the signal intensity and signal width, as shown in figure 3.4 for PTFE at spinning rates of 15 kHz and 25 kHz. In both cases an opposite periodic behaviour for signal intensity and width is found. The intensity maxima, correlated to signal width minima, are located at offsets which are integer multiples of the spinning rate. The modulation is not symmetric to the zero-point, and the amplitude of the modulation is higher for negative offset values. In general the modulation is more pronounced for spectra recorded at 15 kHz. The most significant overall change is found at a spinning rate of 25 kHz, for which a decoupling offset of 50 kHz leads to a gain of intensity, while the signal width is preserved.

The reason for the modulation could be the very high CSA found for fluorine, e.g. for the PTFE, of more than 50 ppm.³³ For this reason the rather moderate spinning rates up to 25 kHz are not capable to fully eliminate the spinning side bands in the fluorine spectra and the decoupling efficiency is good when the decoupling frequency is fixed to the frequency of one of the spinning side-bands. In other words, the oscillation in decoupling efficiency reflects the high CSA of fluorine under an insufficient magic angle spinning. The same modulation was found for the $^{13}\text{C}\{^{19}\text{F}\}$ NMR spectra of hydrated Nafion[®], shown in figure 3.5. The intensity modulation seems to be less distinct, while the change in the signal width is even more pronounced. According to literature the ^{19}F CSA parameter of Nafion[®] (~ 56 ppm) is 15% smaller than that for PTFE (~ 66 ppm), which can be explained by higher motional narrowing for Nafion[®].³³ The correlation between the CSA parameter and the modulation intensity again indicates a relation between the CSA and the modulations. As already mentioned for PTFE, an increase in intensity under conservation of the FWHM is possible. The two spectra recorded for Nafion[®] which are shown in figure 3.5b, give an example for the gain of intensity without expense of the signal width, by applying an offset of -50 kHz relative to the frequency corresponding to the isotropic shift. The signal width is ~ 36 Hz in both cases, whereas the intensity is $\sim 20\%$ higher for the spectra recorded under offset condition.

The high isotropic chemical shift dispersion and high CSA for ^{19}F give rise to the idea that the pulses in the XY-16 sequence are not able to provide a sufficient spin inversion for the full ^{19}F spectrum. If this is true, it should be possible to increase the decoupling efficiency by the use of shorter and harder pulses. Since this is limited by the amplifiers and probe heads used, another option would be the use of composite pulses to achieve a more broad-banded spin-inversion. It was

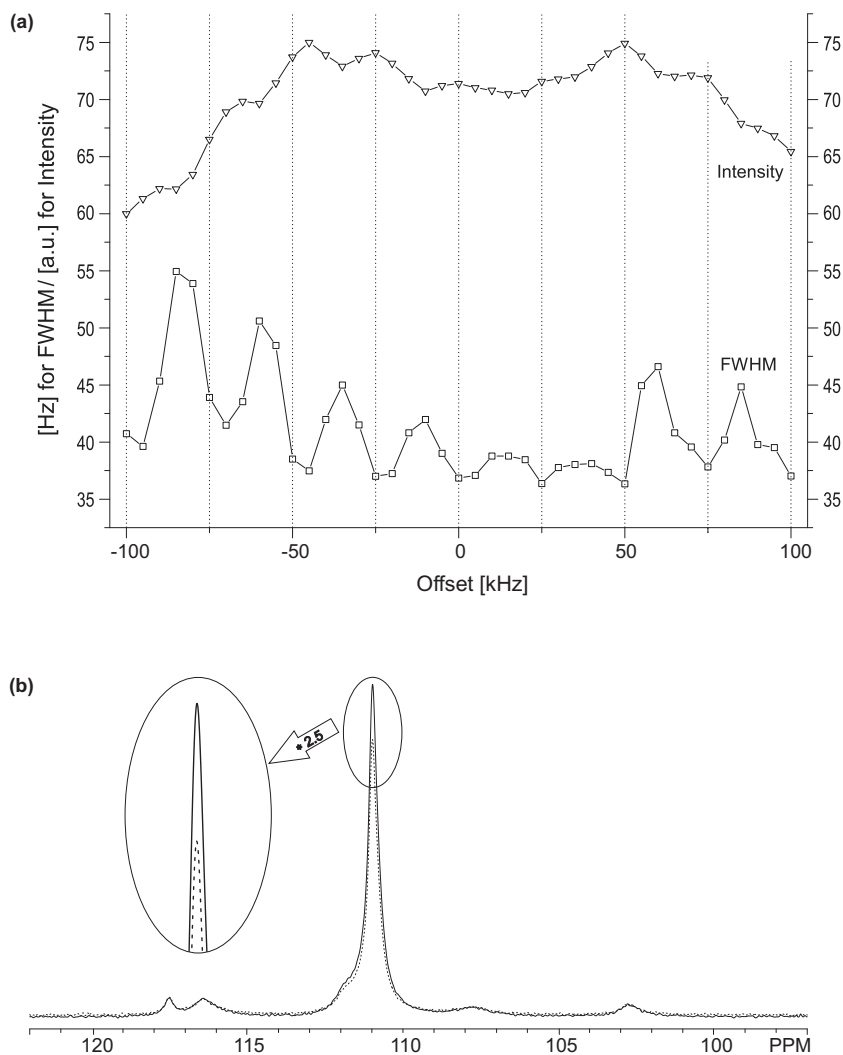


Figure 3.5: (a) Offset characteristics of XY-16 showed for the CF₂ of Nafion® at 25 kHz and (b) Nafion® spectra recorded for on- (dashed line) and off-resonance (solid line) decoupling

possible to show that the use of broadband composite pulses, like $90_x270_y90_y$ or $336_x246_{-x}10_y74_{-y}10_y246_{-x}336_x$ can further increase the line width of PTFE by ~ 1.5 Hz at a spinning rate of 20 kHz.⁴⁰ These results can be interesting with respect to systems with a higher dispersion of isotropic chemical shifts and even higher CSAs, in which case the effect could be even higher.

One draw-back of the XY-16 decoupling sequence is the fact, that the homonuclear dipolar interaction is eliminated exclusively by the MAS. Therefore the sequence is limited to rather high spinning rates $\nu_r > 20$ kHz. To illustrate this, $^{13}\text{C} \{^{19}\text{F}\}$ NMR spectra for Nafion® recorded under XY-16 decoupling at a spinning rate of 11

3 Optimized ^{19}F decoupling techniques for fluorinated membranes

kHz are shown in figure 3.6. The signals are not fully resolved and the CF_2 signal is only decoupled to a line width of ~ 80 Hz. MAS is only able to partially eliminate the broadening caused by the homonuclear dipolar interaction.

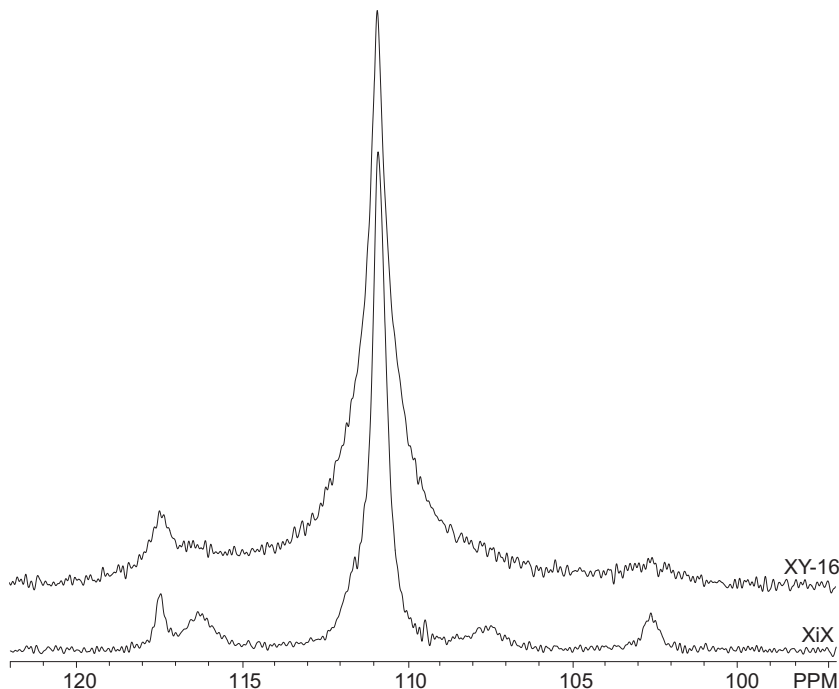


Figure 3.6: ^{13}C $\{^{19}\text{F}\}$ NMR spectra for Nafion[®] recorded under XY-16 and XiX decoupling at a spinning rate of 11 kHz

In contrary, as shown in figure 3.6, an optimized XiX decoupling sequence is appropriate to improve the decoupling efficiency at low spinning rates effectively, narrowing the CF_2 signal from ~ 80 Hz to 46 Hz when used instead of XY-16 decoupling. Regarding the much lower spinning rate of 11 kHz and the only small difference in line width of 10 Hz, compared to the line width achieved by using XY-16 at 25 kHz, a more specified study of the XiX scheme as a tool for ^{19}F decoupling in fluoropolymers is reasonable.

XiX is a high-power decoupling scheme and consists of a continuous irradiation composed of pulses of length τ_p and a phase difference of 180° , as sketched in figure 3.2b. The decoupling performance is strongly dependent on the ratio between the pulse length τ_p and the rotor period τ_r . For proton decoupling it is found in literature that for the ratio between τ_p and τ_r , optima are found for 1.85 and 2.85 and these values are typically used as standard-parameters.²⁷ We were able to show, that when using the XiX scheme for ^{19}F decoupling a similar characteristic can be found. Figure 3.7 shows the intensities and FWHMs recorded for a PTFE sample at a spinning

rate of 25 kHz for different τ_p/τ_r -ratios. This dependency on τ_p/τ_r is similar to the characteristics found in literature for the decoupling of protons.²⁷ The suggestion to start optimization with a τ_p/τ_r -ratio of 1.85 or 2.85 also seems to be valid for fluorine decoupling. This fact keeps the effort needed for the optimization of the decoupling relatively low, since it is only dependent on one parameter, which can be easily calculated from the spinning rate, and for standard applications they can be even used without further optimization.

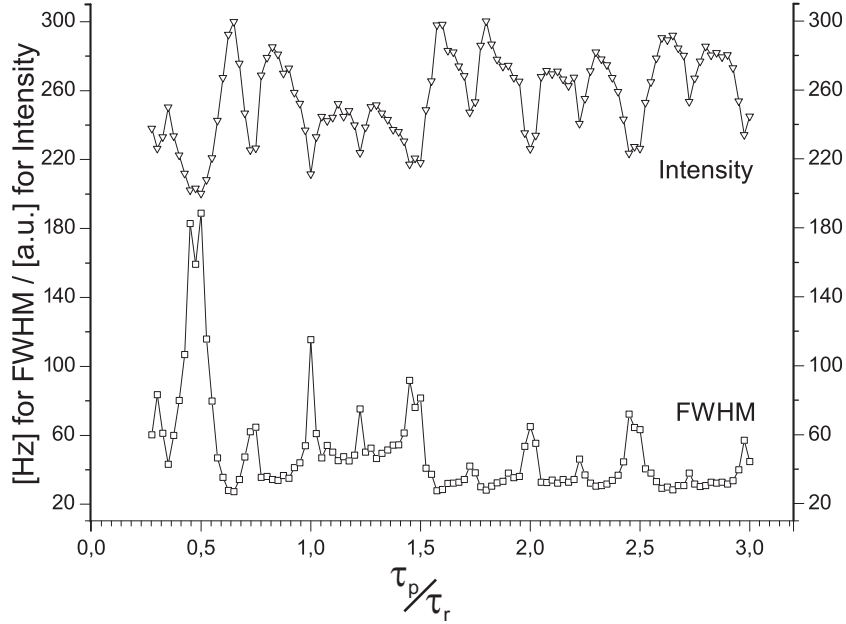


Figure 3.7: Dependency of line width and intensity on the τ_p/τ_r -ratio found for PTFE under XiX decoupling

Figure 3.8 shows the intensity and the FWHM dependency with respect to an offset for the decoupling frequency. The modulating off-resonance behaviour, as found for the XY-16 scheme, is not present for XiX decoupling. The FWHM shows a minimum for an offset of 5 kHz relative to the frequency corresponding to the isotropic chemical shift of fluorine, while for the intensity a maximum is found. Missing out this modulating behaviour, the decoupling efficiency is decreases constantly with an increasing offset.

The large difference between the decoupling efficiency of TPPM and XiX is an interesting fact. A comparison done in literature for proton decoupling for alanine described the potential of XiX compared to TPPM in the sharpening of broad 'feet' of signals even for the cases where the FWHM was the same for both sequences, but it did not show the large discrepancy found for fluorine decoupling.³⁹ One reason

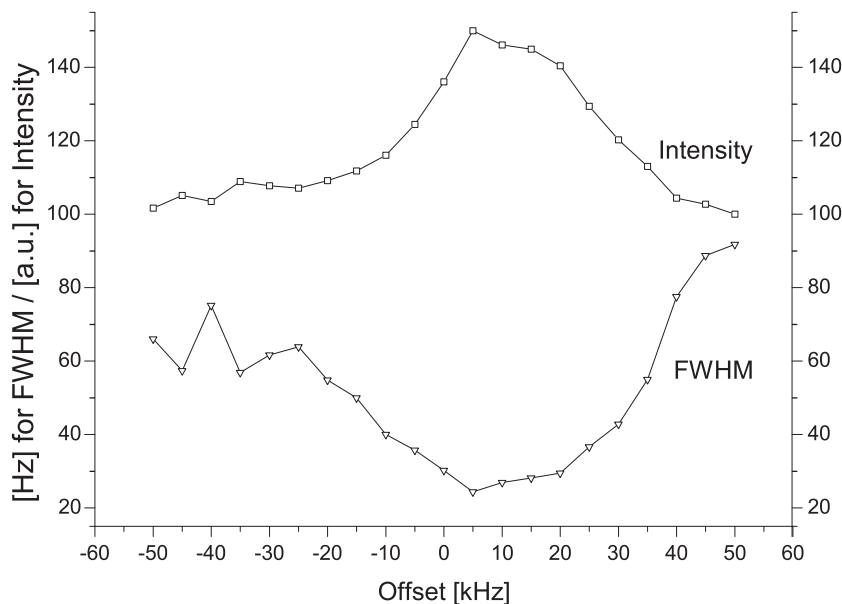


Figure 3.8: Offset characteristics for XiX decoupling on the PTFE ^{13}C resonance

for the superiority of XiX over XY-16 at low spinning rates could be the generation of a series of decoupling side-bands, due to the phase modulation ω_m with frequencies of $\pm(2n + 1)\omega_m$ compensating the splitting into spinning side-bands in the ^{19}F spectrum, present at low spinning rates.²⁹ It also has to be noted, that in the above mentioned publication, for the application of frequency-swept TPPM on potassium nonafluoro-1-butanesulfonate (NFBS-K) and sodium pentafluoro-propionate (PFP-Na) good decoupling performance was found and discussed in relation to a second-order cross term between chemical shift and dipolar coupling.^{38,41} However, a direct comparison to my results on highly flexible and mobile systems is difficult, since NFBS-K and PFP-Na are described as rigid organic solids.

To compare the decoupling efficiency at different spinning rates, the FWHM and the signal to noise ratio (S/N) for the PTFE carbon signal at different spinning rates are plotted in figure 3.9 and 3.10, respectively. While the S/N ratio for the XY-16 decoupled spectrum overcomes the XiX already at 15 kHz, XiX results in sharper lines up to a spinning rate of ~ 20 kHz. According to these results at high spinning rates, the XY-16 ^{19}F decoupling has superior performance for fluorinated materials. Nevertheless the XiX scheme seems to be an interesting alternative when the spinning rate is limited, since it can provide a sufficient decoupling at a rather low spinning rate of 11 kHz. The reasons for a limitation of the spinning rate are manifold, e.g the need of large rotors for the signal enhancement or the separation

effects for wet samples at high spinning rates.

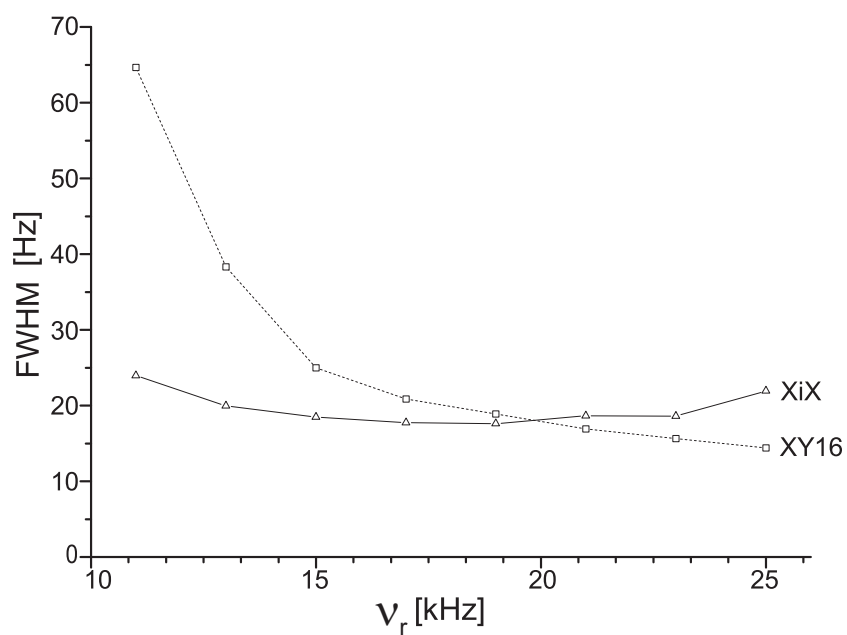


Figure 3.9: FWHM of the PTFE ^{13}C signal obtained under XY-16 and XiX decoupling at different spinning rates

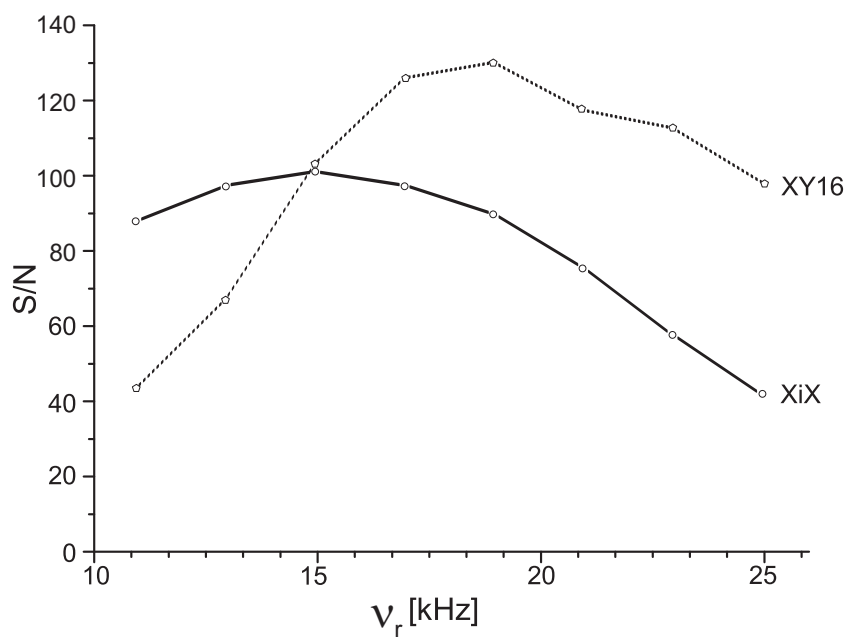


Figure 3.10: S/N of of the PTFE ^{13}C signal obtained under XY-16 and XiX decoupling at different spinning rates

3.3 Conclusion

The presented results show the possibility to further improve the high decoupling efficiency of the XY-16 decoupling scheme for fluoropolymers reported in literature by exploiting the modulating off-resonance behaviour with maxima in intensity for $\Delta\nu_{dec} = n\nu_r$, while preserving the FWHM found for on-resonance decoupling. For a Nafion[®] sample one can achieve 20% gain in intensity with constant line width for a -50 kHz decoupling frequency offset at MAS frequency of 25 kHz. In addition it was possible to further understand the good performance of the XY16-decoupling scheme by thoroughly examining the characteristics of the sequence and by the use of composite pulses.

When using the XY-16 sequence one is limited to high spinning rates, which makes it impossible to use rather large rotors. In future this limitation can be avoided by applying the XiX scheme on fluorinated membranes, which leads to a line width reduced by 40% compared to spectra recorded under XY-16 decoupling at the same spinning rate of 11 kHz. In this respect XiX decoupling can be an interesting tool, when spinning is limited to low values $\nu_r < 15$ kHz, .e.g. for one of the reasons discussed above.

4 Characterization of radiation grafted polymer films using CP/MAS NMR spectroscopy

4.1 Introduction

Polymer electrolyte fuel cells (PEFCs) are known as highly efficient and clean energy converters. They are operated at ambient temperatures between 60 °C and 100 °C. Their major advantage is the low weight and fast start-up capability. Due to these reasons they are used in emergency power supplies or in electrical cars. The two critical parameters for a membrane to be used in a fuel cell are the performance and the longevity. The state-of-the-art membranes, e.g. Flemion[®], Aciplex[®] or Nafion[®] extensively fulfill these requirements. However, these membranes are still too expensive for most applications, and therefore the actual objective of research is the development of less costly membranes.

Among many approaches which are in the actual focus of research, one cheaper possibility to produce a proton conducting polymer membrane is the modification of commercially available perfluorinated or partially fluorinated base films. This can be achieved by radiation grafting during which the desired base film, e.g. PTFE, is electron beam irradiated to produce a certain concentration of radicals in the membrane, which in turn can react with a solution of suitable monomers, e.g. α -methylstyrene (AMS). There are two different ways to perform the irradiation, either simultaneously⁴² or in advance of the grafting of the monomers onto the base film. Then, the pre-irradiation can be done in air or under an inert atmosphere.⁴³ As for the commercially available PEFC membranes, the desired proton conductivity is achieved by sulfonic acid groups in the membrane. These can be introduced by the direct grafting of monomers which carry a sulfonic acid group or in a second step after the grafting, i.e. the sulfonation of the grafted compounds.⁴⁴

The membranes in this study were synthesized by the pre-irradiation grafting method in air. The reason for this choice is found in the lower requirements compared to pre-irradiation under an inert atmosphere or the simultaneously applied grafting radiation. Another advantage is the absence of homopolymer, which has no covalent bond to the base film and is caused by transfer reactions between the chain and the monomer, or by a direct influence of the radiation on the monomer during simultaneously performed irradiation. If the membrane does not swell during the grafting process one can describe the grafting by the front-mechanism shown in figure 4.1. This is true for all different synthetic approaches.

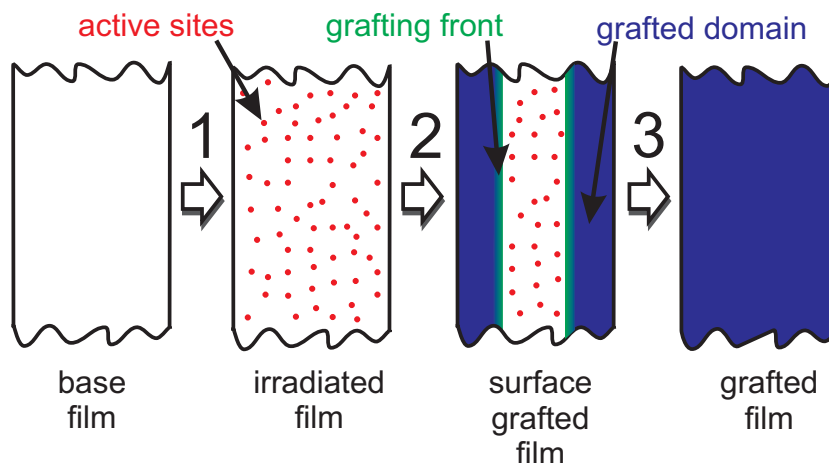


Figure 4.1: (1) Active sites (radicals) are generated by activation inside the base film. (2) Beginning of the grafting at the surface, followed by bulk grafting after diffusion of the monomers into the membrane. (3) Homogeneously grafted film with the same degree of grafting over the entire film thickness. *Adopted from Wallasch et al.*⁴⁵

The high through-plane proton conductivity which is essential for the fuel cell application⁴⁶ is dependent on the sulfonic acid group's homogeneity along the entire membrane thickness (fully grafted film in figure 4.1). Normally, the degree of grafting (DoG) is used as parameter for the overall grafting in such reactions. It is the mass-ratio of the reacted grafting component and the original base film mass.

$$\text{DoG} = \frac{m_{\text{graft}} - m_{\text{base}}}{m_{\text{base}}} \quad (4.1)$$

Where m_{base} is the mass of the irradiated base film and m_{graft} is the mass of the membrane after the grafting reaction. Another possibility to further influence

the mechanical and dynamic properties of a membrane is the use of a mixture of grafting monomers. The membranes in this study are formed by the use of a mixture of AMS and methacrylonitrile (MAN). For these membranes the DoG alone cannot describe the molecular situation in a suitable manner, since it is not capable of describing the ratio of the two components in the membrane. The grafted ratio does not have to be equal to the ratio in the grafting solution, since the monomers can differ in their reactivity and diffusion behaviour into the membrane. The determination of the AMS:MAN-ratio can be a rather complicated challenge due to the poor solubility of the grafted membranes. For this reason the AMS:MAN-ratio is commonly determined by FT-IR spectroscopy. The FT-IR spectra reveal separate signals for the two components and the ratio can be calculated by the help of previously recorded calibration curves.^{47,48} One major drawback of this method are the problems which arise from the expansion of the film during the grafting which in turn change the area considered in the FT-IR measurements and leads to the exigency of a factor correcting this behaviour.

A complementary method for the characterization of such membranes can be the solid state NMR spectroscopy which is not affected by the poor solubility of the fluorinated materials. The studies found in literature are mainly focused on the application of ^1H and ^{19}F NMR spectroscopy dealing with a large variety of features, as the structure, structural dynamics and degradation.³⁵ There are also some works based on ^{13}C spectra measured for such samples.^{33,34} It is known, that for studies of fluorinated samples one needs high spinning rates and dedicated decoupling techniques. While these aspects are covered in chapter 3, this chapter will deal with the protonated parts of membranes.

Due to the low abundance of the ^{13}C -isotope the NMR signal is normally enhanced by the CP technique which is briefly described in chapter 2.1.5. As it is described there, the dynamic of the magnetization transfer is affected by many parameters (e.g. proton density, internuclear distances and dipolar coupling) and can strongly differ for different molecules or even different nuclei in one molecule. Figure 4.2a demonstrates this and shows three build-up curves recorded for the CH_3 , CN and CO carbon resonances in a $\{^1\text{H}\}^{13}\text{C}$ CP spectrum of N-t-Boc-alanine, i.e. the signal intensities are plotted against the CT which was used for the magnetization transfer in the sequence.⁴⁹ These curves can contain important information about the dipolar coupling or mobility effects.⁵⁰ However, since the transfer dynamics can strongly differ for different sites, the possibility of integration or even the determination of

relative amounts, is not given in general for a $\{^1\text{H}\}^{13}\text{C}$ NMR CP spectrum.

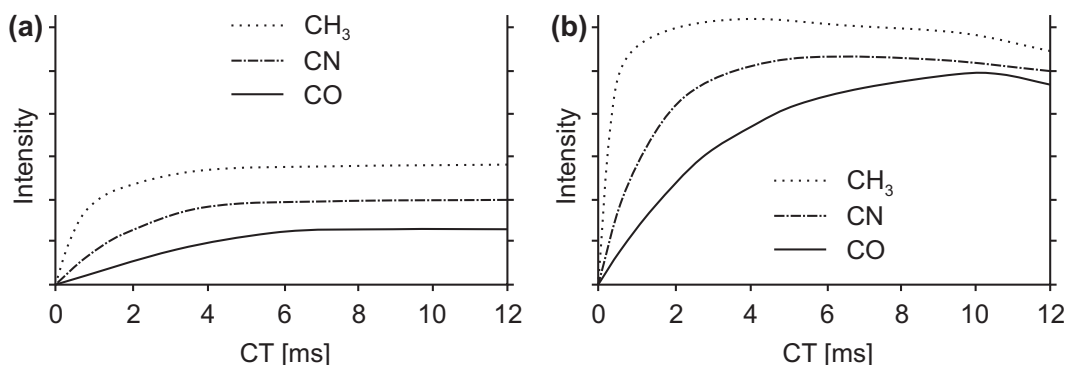


Figure 4.2: Build-up curves for the CH_3 , CN and CO carbon resonances in a $\{^1\text{H}\}^{13}\text{C}$ CP spectrum of N-t-Boc-alanine for a (a) normal and a (b) ramped CP sequence. *Adopted from Metz et al.*⁴⁹

Several specially designed sequences are known in literature which can be able to overcome this problem under certain conditions, e.g. the quantitative cross polarization (QUCP) sequence.¹⁰ The use of a ramped CP sequence is also known to partially compensate for these unwanted effects, but only for a long enough contact time, e.g. after 10 ms in the example shown in figure 4.2b.⁴⁹

In this chapter the use of $\{^1\text{H}\}^{13}\text{C}$ CP NMR spectroscopy to determine the monomer ratio in a mixed monomer membrane system will be discussed and validated by comparison to ^{13}C single pulse (SP) spectra. It will be shown that the monomer ratios obtained by $\{^1\text{H}\}^{13}\text{C}$ CP NMR spectroscopy can be used as an alternative to the values obtained by FT-IR spectroscopy and in turn validate the latter one.

4.2 Sample preparation

The samples in this study were prepared in the group of *Günther G. Scherer at the Paul Scherrer Institut in Villigen (CH)*. The membranes are based on poly(tetrafluoroethylene-co-hexafluoropropylene) (FEP, Teflon® 100 Å, DuPont, Circleville, OH, USA) with 25 μm thickness and were prepared by a known procedure.^{47,48} After the electron beam irradiation to a dose of 25 kGy, the FEP films were stored at -80 °C. For the grafting, the films were immersed into a grafting solution, consisting of 20 vol% water ($>18.2\text{ M}\Omega\text{cm}$ Labpure®), 50 vol% isopropanol ($>99.8\%$, Fluka) and 30 vol% monomer solution, either MAN (99%, stabilized with 50 ppm monomethyl ether hydroquinone, Aldrich) or a mixture with AMS (99%, stabilized with 15 ppm 4-(tert-butyl)catechol, Aldrich), at a nAMS:nMAN-ratio of 1.5. The grafting process was performed at a temperature of 50 °C and the reaction time was varied to obtain different DoGs (5%, 15%, 24%, 35% and 44%).

4.3 Results and Discussion

As mentioned above, the determination of the relative amounts of the two monomers MAN and AMS is usually performed by FT-IR spectroscopy. For this purpose, spectra were recorded for wavelengths between 4000 cm^{-1} and 400 cm^{-1} with a Perkin Elmer FTIR System 2000 spectrometer and evaluated with the curve fitting GRAMS/AI software, version 8.00 (Thermo Electron Corporation, Waltham, USA). The concentration of AMS was determined using the aromatic C=C-stretching vibration at 1498 cm^{-1} and for MAN using the C=N-stretching vibration at 2235 cm^{-1} . The results are shown in table 4.1.

Table 4.1: Comparison of the AMS:MAN molar ratios determined with FT-IR spectroscopy

DoG [m/%]	5	15	24	35	44
AMS:MAN-ratio	0.84	0.85	0.91	0.92	0.91

As mentioned in chapter 4.1 these values are calculated by the use of a correction factor which deals with the expansion of the film during the grafting process. Due to the poor solubility of the fluorinated material, the determination of the ratio by solution NMR spectroscopy is not applicable. To overcome these problems, the idea is to use $\{^1\text{H}\}^{13}\text{C}$ MAS CP NMR spectroscopy for the determination of the molar ratios. Figure 4.3 and 4.4 show the $\{^1\text{H}\}^{13}\text{C}$ CP NMR spectra for a sample grafted with MAN and a MAN/AMS mixture, respectively. By comparing the two spectra it is possible to assign all signals present, whereby the signals for the phenyl ring in the AMS are not resolved at the present field of 400 MHz and a spinning rate of 13 kHz.

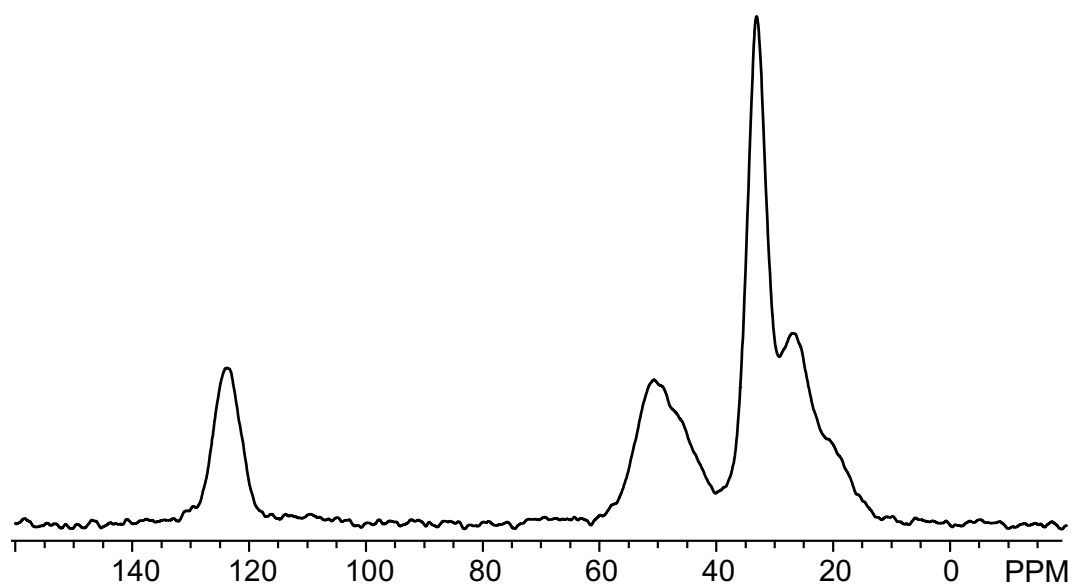


Figure 4.3: $\{^1\text{H}\}^{13}\text{C}$ CP NMR spectrum for a sample grafted with MAN.

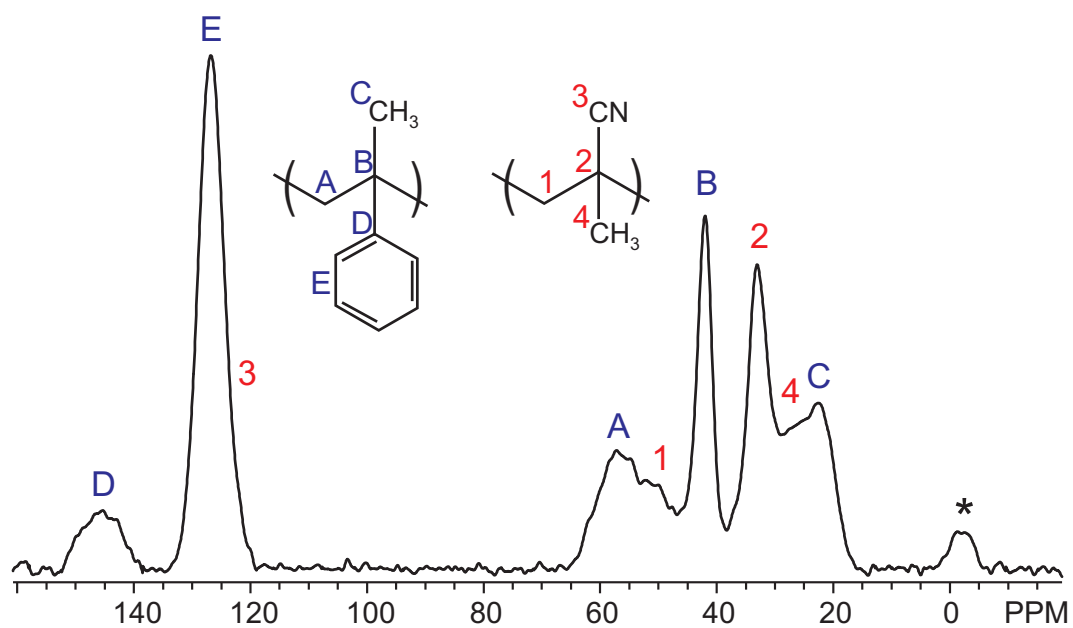


Figure 4.4: $\{^1\text{H}\}^{13}\text{C}$ CP NMR spectrum for a sample grafted with a MAN/AMS mixture.

Table 4.2 shows the exact ppm-values for the signal assignment which was performed by spectral deconvolution of the region between 0 and 70 ppm using the NUTS NMR utility transformation software (Acorn NMR 2009, Livermore, CA). Figure 4.5 shows an example for the deconvolution of this area.

Table 4.2: Signal assignment for the $\{^1\text{H}\}^{13}\text{C}$ CP NMR spectra. The signal positions are found in figure 4.4.

Monomer	Chemical shift [ppm]	Signal assignment
MAN	123	3
	51	1
	33	2
	27	4
AMS	144	D
	127	E
	57	A
	42	B
	22	C

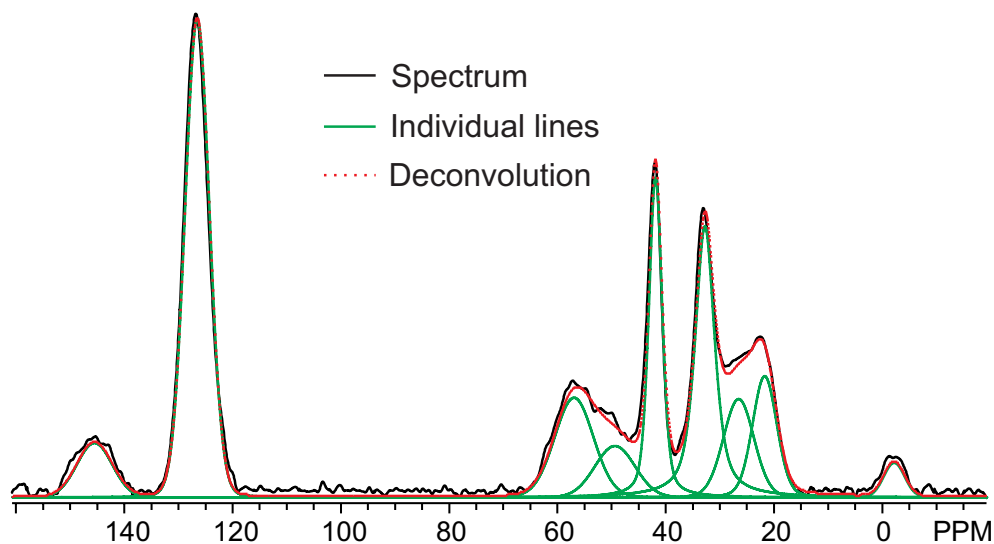


Figure 4.5: Spectral deconvolution of the region between 0 and 70 ppm using the NUTS NMR utility transformation software (Acorn NMR 2009, Livermore, CA).

At this point in general all signals found for the MAN and AMS monomer could be used to quantify the AMS:MAN-ratio. However, the best signal separation was found for the two quaternary carbons in an α -position to the phenyl ring (assignment B in figure 4.4, 42 ppm) and next to the cyano group (assignment 2 in figure 4.4, 33 ppm). The fact that both are quaternary carbons could cause a similar CP dynamics.

The determination of the AMS:MAN-ratios for the peaks at 33 ppm and 42 ppm was done in three steps:

- Acquisition of the $\{^1\text{H}\}^{13}\text{C}$ CP NMR spectra for all membranes for a fixed CT of 5 ms.
- Acquisition of the CP build-up curves, i.e. the signal integrals for different contact times, for selected samples to show that the ratio is independent from the chosen CT.
- Acquisition of the ^{13}C single pulse NMR spectra for the same selection of membranes to prove that the ratio determined by the CP spectra is not affected by the possibly different CP dynamics of the signals at 33 ppm and 42 ppm.

Figure 4.6 shows the signal integrals in dependency on the CT, extracted for the signals at 33 ppm and 42 ppm from spectra recorded for the sample with a DoG of 44%. One can see that the integrals increase in a parallel manner until a maximum is found for a contact time of approximately 2 ms. After this maximum the signal integrals slowly decrease in a parallel manner. To verify the independence of the AMS:MAN-ratio on the CT, it is plotted in the same graph.

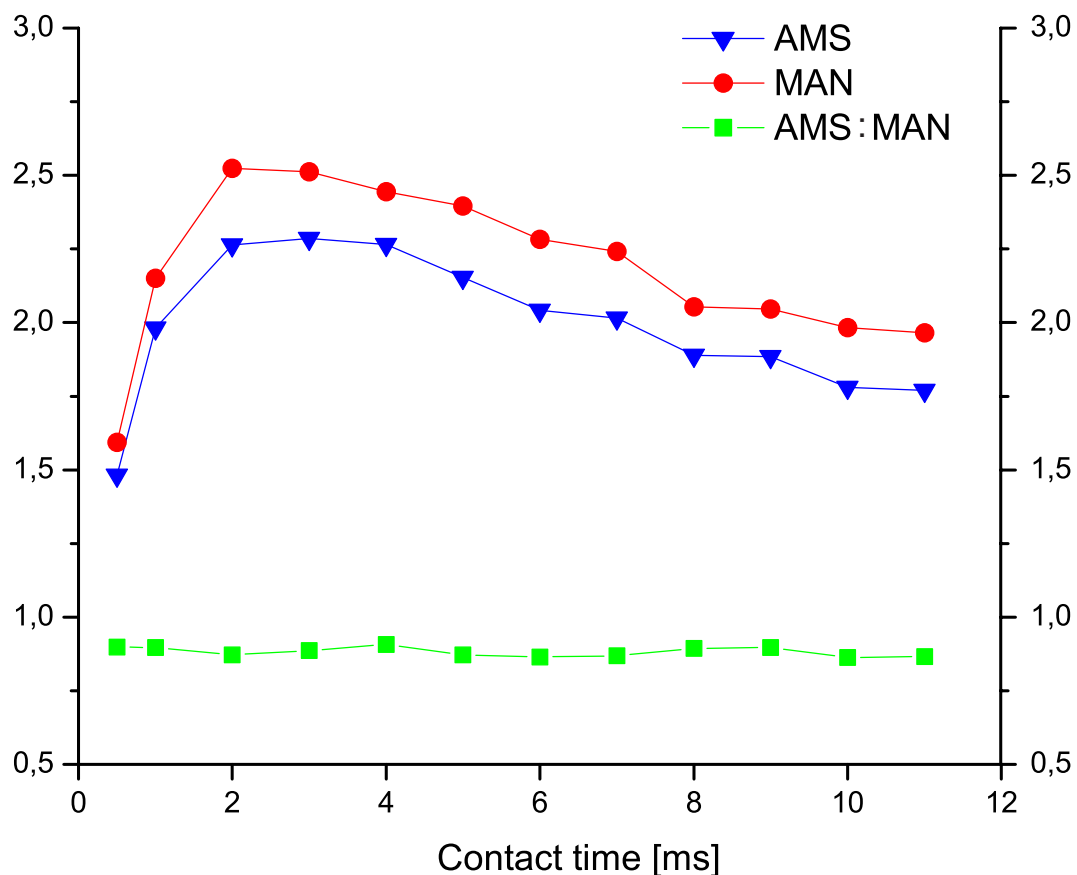


Figure 4.6: Build-up curves for the two quaternary carbons in α -position to the phenyl ring (assignment B in figure 3, 42 ppm) and next to the cyano group (assignment 2 in figure 3, 33 ppm) and the calculated AMS:MAN-ratios.

The AMS:MAN-ratios determined by the $\{^1\text{H}\}^{13}\text{C}$ CP spectra are given in table 4.3. The fact that the determined ratios are independent of the CT does not prove the reliability of the absolute values. As mentioned before, for this reason the ^{13}C single pulse spectra for two samples were recorded. Figure 4.7 compares the single pulse and the CP spectra for the sample with a DoG of 44%. The additional signals between 90 ppm and 120 ppm are related to the fluorinated carbons of the base films

and are not visible in the CP spectra due to the absence of protons. The results for the two ratios determined by the single pulse spectra are given in table 4.3 and are in good agreement with the values obtained by $\{^1\text{H}\}^{13}\text{C}$ CP NMR spectroscopy.

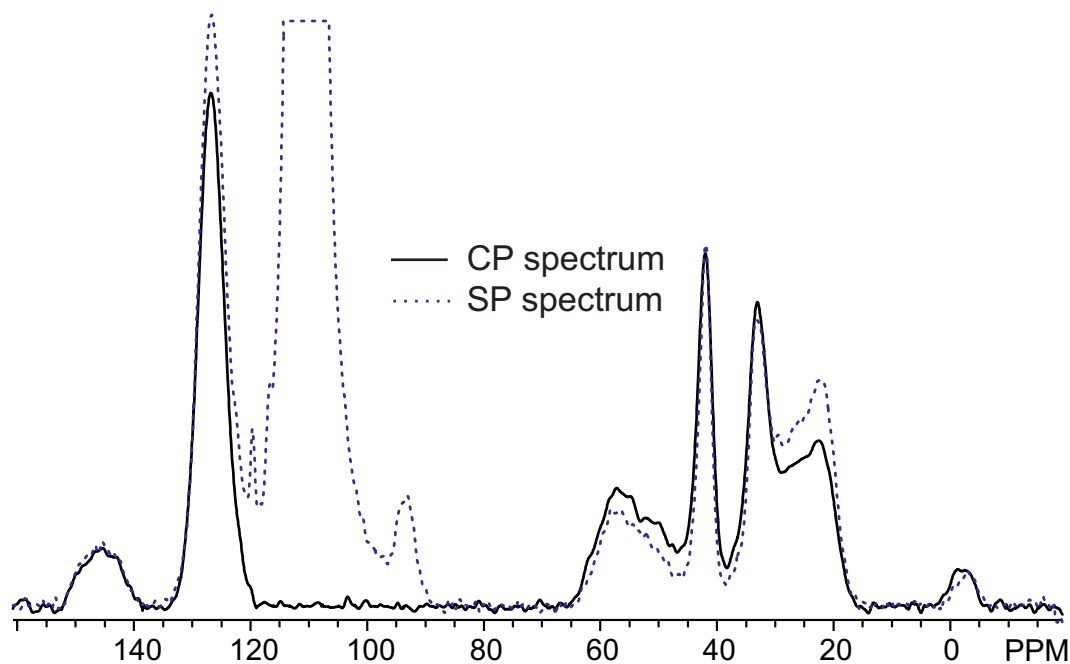


Figure 4.7: Comparison of the $\{^1\text{H}\}^{13}\text{C}$ CP and the ^{13}C single pulse spectrum recorded for the sample with DoG of 44%.

Table 4.3: Comparison of the AMS:MAN molar ratios determined by the use of the $\{^1\text{H}\}^{13}\text{C}$ CP and ^{13}C single pulse spectra

DoG [m/%]	5	15	24	35	44
AMS : MAN by $\{^1\text{H}\}^{13}\text{C}$ CP	0.82	0.89	0.92	0.88	0.87
AMS : MAN by ^{13}C single pulse	—	—	—	0.90	0.89

4.4 Conclusions

The deviation for the AMS:MAN-ratio obtained by NMR is found to be below 5% with respect to the CT and the value obtained by ^{13}C SP spectroscopy. The results for the membrane with DoG of 44% are plotted in figure 4.8. The values obtained by FT-IR spectroscopy and the ^{13}C SP spectra are also plotted in this graph.

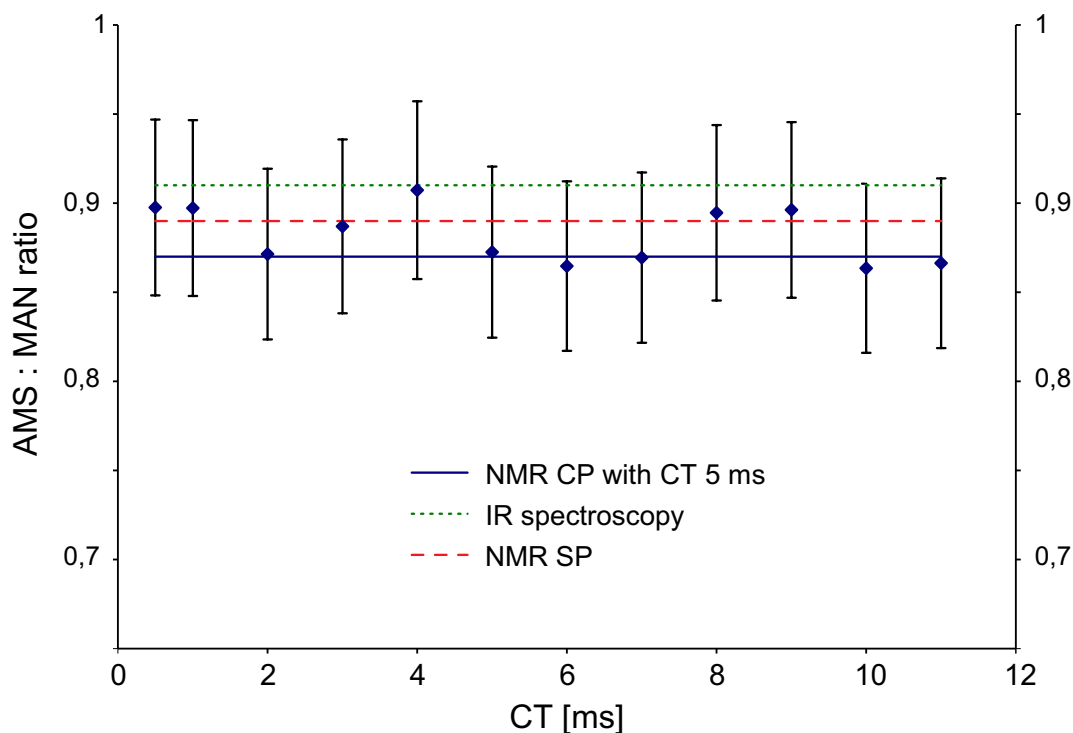


Figure 4.8: AMS:MAN-ratio in dependency of the CT with the respective error bars assuming an error of 6 %. The values obtained by FT-IR spectroscopy and the ^{13}C SP spectra are shown as horizontal lines.

The standard deviation for the molar AMS:MAN-ratio is found to be 5% for the values obtained by FT-IR spectroscopy. The values obtained by FT-IR spectroscopy and the ^{13}C SP spectra lay within the 6% error bars added to the CP dataset. The first thing to notice here is the good agreement between all three different methods.

Table 4.4 combines the results for the AMS:MAN-ratio in dependency on the DoG obtained by the use of FT-IR, $\{^1\text{H}\}^{13}\text{C}$ CP and ^{13}C single pulse spectra.

The values for the AMS:MAN-ratio determined by the three different techniques reveal a high degree of consistence for all different membranes. However, the values obtained by FT-IR spectroscopy exhibit an uncertainty, since the values are corrected by an approximated expansion factor, while the values obtained by $\{^1\text{H}\}^{13}\text{C}$

Table 4.4: Results for the AMS:MAN-ratio in dependency on the DoG obtained by the use of the FT-IR $\{^1\text{H}\}^{13}\text{C}$ CP and ^{13}C single pulse spectra

Molar AMS:MAN-ratio			
DoG [m%]	in the grafted polymer obtained by		
	FT-IR	$\{^1\text{H}\}^{13}\text{C}$ CP	^{13}C SP
5	0.84	0.82	—
15	0.85	0.89	—
24	0.91	0.92	—
35	0.92	0.88	0.9
44	0.91	0.87	0.89

CP possess a certain measurement inaccuracy caused by the slightly different CP dynamics of the signals used for the ratio calculation. Only in comparison with the values extracted from the ^{13}C SP spectra, both methods reveal a high degree of accuracy.

With respect to the good agreement of the values obtained by ^{13}C NMR and FT-IR spectroscopy, the latter will be further used as routine method to determine the monomer ratio, while the so far approximated expansion factor can now be calculated from the results of the exact ^{13}C SP NMR measurements. Nevertheless, the determination of the ratio by $\{^1\text{H}\}^{13}\text{C}$ CP NMR spectroscopy can still be an interesting alternative for different pairs of monomers or even for mixtures which consist of more than two components.

5 Solid state NMR and XRD line profile analysis of heavily deformed fluorite

5.1 Introduction

Fluorine based materials are known for their transport properties and stability. For this reason they find application in several fields engaged with energy conversion, e.g. as electrolytes in fuel cells, transparent electrodes for solar cells and electrodes for aqueous batteries, i.e. lithium batteries.⁵¹ Also in systems for clean energy storage, such as secondary ion batteries and fuel cells, fluorides are used as well as in chemical sensors.^{37,52,53} In the last years nano-structured ionic materials got into the focus of research, e.g. as new catalysts.^{37,54–57}

The potential of an ionic conductor to be used for energy storage mainly depends on its ionic conductivity which in turn is closely related to its microstructure. The microstructure of an ionic material is amongst other parameters described by lattice defects, e.g. vacancies as point defects in which ions can migrate. Even if less distinct, line (dislocations) and planar defects (stacking faults, interfaces and grain boundaries), as well as defects in form of dislocations, can be crucial to describe the microstructure.

CaF_2 is found to be an important material with respect to many applications. It is used as a reactant in the production of hydrofluoric acid, ceramics and glasses. Other applications of CaF_2 are the use as catalyst in the production of calcium cyanamide and as material for UV-permeable high performance lenses.

In the following chapter CaF_2 was chosen as an example for a typical ionic conductor. It is characterized by a simple and stable face-centred cubic (fcc) crystal structure, wherein the Ca^{2+} ions are arranged in a fcc lattice and the F^- ions fill up all tetrahedral positions. A series of CaF_2 samples was prepared by high energy

ball milling, whereby tungsten carbide (WC) and steel were used as materials for the vial and the balls of the planetary mill. The samples were analysed by means of NMR spin lattice relaxometry and X-Ray diffraction in combination with line profile analysis (LPA).

As described in chapter 2.2 XRD-LPA in combination with Whole Powder Pattern Modelling (WPPM) can be a powerful tool to gather information on microstructural features, e.g. the crystalline domain shape and size distribution or the density of planar faults and dislocations. According to literature the most prominent defects induced by ball milling are planar faults and dislocations.⁵⁸ Transmission Electron Microscopy (TEM) and X-ray topography proved themselves as a tool to study dislocations in such materials. However, they don't give sufficient information about the quantity of the defects.

Therefore, even if high resolution TEM pictures can show the direct evidence of the extensive presence of dislocations in ball milled fluorite⁵⁸, quantification usually involves XRD-LPA methods⁵⁹ which can be effective even for dislocation densities as high as $10^{16} - 10^{17} \text{ m}^{-2}$.^{60,61} For these reasons the technique is known to be an efficient tool to study line-defects. On the other side the XRD-LPA technique only reveals an average density weighted over the dislocation population⁶² and is not sensitive to inhomogeneities which are often induced by high energy ball milling or other processes capable of causing plastic deformations. If such inhomogeneities are present in a sample, a complementary technique is needed to be combined with the results from the XRD-LPA.

As outlined in chapter 2.1 NMR spectroscopy is very sensitive to the local electronic structure, which in turn is dominated by the bonding angles and the local atomic coordination. In a crystalline material the latter is strongly influenced by size-effects and the presence of dislocations.⁶³ In literature there are several examples where ^{19}F NMR spectroscopy was used to investigate structural defects and the F^- mobility in different fluorites.^{64,65} ^7Li relaxometry proved to be a versatile tool to distinguish phases in heterogeneously structured lithium containing nanocrystalline materials.⁶⁶

This work presents results from XRD-WPPM and ^{19}F NMR T_1 measurements on high energy ball milled CaF_2 , whereas only the complementary analysis of both methods was able to draw a clear picture of the microstructural processes during the milling procedure. Also iron-contaminated samples were in the focus of this work and it could be shown that the technique is applicable to other materials even under

the influence of paramagnetic impurities.

It has to be mentioned that there is a recent publication dealing with CaF_2 obtained by high energy ball milling from *Stösser et al.* by the use of ^{19}F NMR and XRD.⁶⁷ The data obtained by XRD and NMR in this publication are considered separately. The samples and also the interpretation differ significantly from the results shown here. This aspects will be discussed in chapter 5.4.

5.2 Sample preparation

All samples used in this study were prepared by high energy ball milling of commercially available CaF_2 powder. The used CaF_2 contained a minor fraction of MgO below 1.5wt%. The samples were ground in a planetary mill (Fritsch Pulverisette 6) at a rather high rotational rate of 400 rpm. All batches were milled in a counter-rotating vial characterized by a 1:1 height:diameter ratio and a nominal volume of 45 ml. For one batch of 2.11 ± 0.01 g of CaF_2 including 2 wt% of ethanol as lubricant, 12 balls with a diameter 12 mm were used to achieve a powder to ball ratio of 1:40. Two series of samples were prepared under the use of WC and Fe as material for the vial and the balls. The milling time was varied from 4 h to 64 h (4 h, 8 h, 16 h, 32 h and 64 h). The absolute milling times containing the periodical breaks for letting the sample cool down are therefore much longer.

A third series of samples was prepared by the direct co-precipitation method by the use of CaCl_2 and NH_4F as reactant in an exchange reaction. 0.01 mol of CaCl_2 was added to 100 ml of a mixture of water and ethanol. The water:ethanol-ratio was varied to achieve ethanol concentrations of 0%, 30%, 60%, 90% and 100%, while the molarity was kept constant at 0.1 mol/l. As the dissociation rate of CaCl_2 depends on the ethanol concentration the time needed to produce a clear solution differed for the different samples. An appropriate amount of NH_4F (0.02 mol) was added to the solution which was then stirred for roughly 16 hours at room temperature. The white precipitation was separated from the solution by high speed centrifugation and cleaned several times with distilled water and ethanol to remove undesired ions. Finally the powder was dried in air at room temperature and ground softly in a diamond mortar.⁶⁸

5.3 Results and Discussion

5.3.1 CaF₂ milled using WC balls

In this chapter the results on ball-milled CaF₂ will be shown and discussed. In the first part the focus is kept on the samples milled using WC balls in a WC-vial. After discussing the XRD-LPA and ¹⁹F NMR results separately, the complementary interpretation of the two methods will be described.

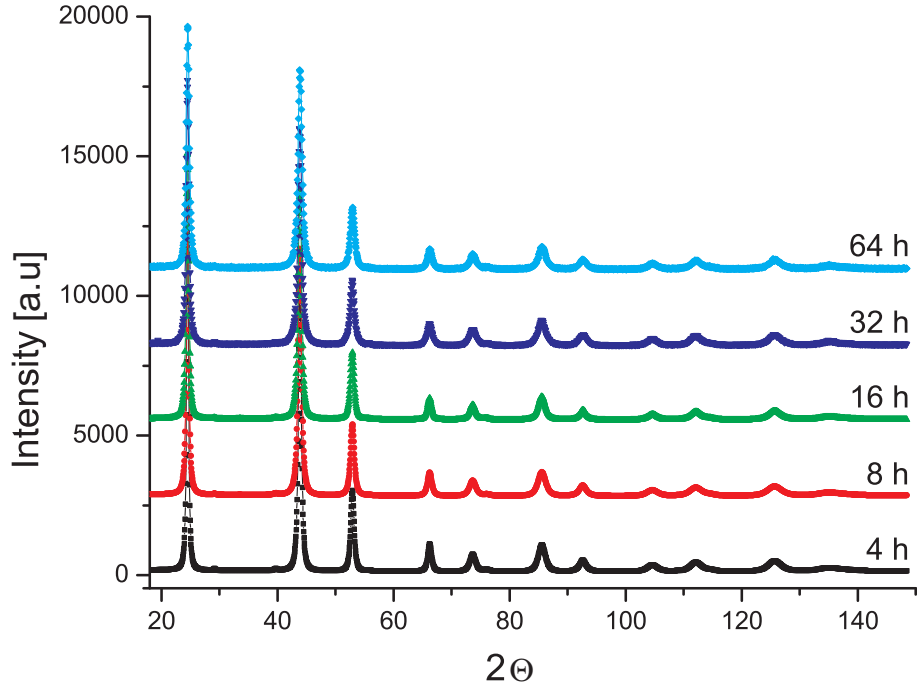


Figure 5.1: X-ray powder patterns recorded for CaF₂ samples milled for 4 h, 8 h, 16 h, 32 h and 64 h

Figure 5.1 shows the powder patterns recorded for the CaF₂ samples milled for different milling times. The positions of the diffraction maxima are not affected by the milling process. This reflects the obvious fact that the general crystal structure is not affected by the ball milling. However a progressive line broadening can be observed for an increase of the milling time, prospectively caused by the decrease of the average domain size and the increase of the mean dislocation density.

To quantify these features the powder patterns were analysed by the WPPM method which was briefly described in chapter 2.2.2 and is a convenient method to analyse the domain size and lattice strain broadening effects simultaneously.^{62,69} As already done in previous studies,⁷⁰ the dislocations in the primary slip system of

fluorite ($\{001\} \langle 110 \rangle$) were considered as the major source of strain broadening. Taking this into account and also factoring the knowledge of the fluorite single-crystal elastic constants,⁷¹ the dislocation contrast factor was determined for both edge and screw dislocations^{58,72,73} to be: $C'_{\text{edge}} = 0.104228 + 0.388633 H$ and $C'_{\text{screw}} = 0.126335 + 0.060745 H$, with $H = (h^2k^2 + h^2l^2 + k^2l^2)/(h^2 + k^2 + l^2)^2$. By analysing the powder patterns by WPPM with the PM2K software^{25,62,69} the mean dislocation density (ρ) and the effective cut-off radius (R_e) of the dislocation system can be determined. To model the domain size effect, a log-normal distribution (mean μ and variance σ) of spherical domains was refined.

When analysing the powder patterns of the samples milled for 16 h, 32 h and 64 h, the WPPM gave satisfactory results with a high degree of conformity between the experimental and the theoretical powder diffraction patterns. The corresponding results are found in table 5.1. After 16 h of milling the average domain size is reduced to 13 nm. For the samples milled for 32 h and 64 h a slightly lower average domain size of 12 nm is found, while the dislocation density is found to be relatively high and increases further with the milling time.

Table 5.1: X-ray WPPM results for the samples milled for 16 h, 32 h and 64 h. Estimated standard deviations are reported in parentheses, referred to the last significant digits.

Milling time	Mean dislocation density	Average domain size
[h]	$[10^{15} \text{ m}^{-2}]$	[nm]
16	13(1)	13(1)
32	16(1)	12(1)
64	28(1)	12(1)

However, for the powders milled for 4 h and 8 h the WPPM is not capable of describing the experimental powder pattern in a sufficient way. It seems to be likely that for these samples which were milled only for a shorter period the powders are not homogeneous and a two phase system could be best to describe the situation. But even under this assumption the WPPM is unstable and the parameters for the two phases correlate in a strong way.

As mentioned in the beginning, at this point the NMR results will be discussed independently from the X-ray diffraction data. For all samples ^{19}F NMR spectra were recorded. Figure 5.2 shows one exemplary NMR spectrum. All spectra show

one broad resonance, and strong spinning side bands are found. The spinning side bands still present at rather high spinning rates reveal the high CSA found for the samples.⁷⁴ Unfortunately it was not possible to achieve a spectral resolution high enough to distinguish two or more different fluorine sites. Even at high spinning rates of 28 kHz it was not possible to distinguish between different signals. It is known from literature that for such samples spinning rates of over 30 kHz are needed to achieve a higher resolution and even then, the signals have to be analysed by deconvolution.⁶⁷

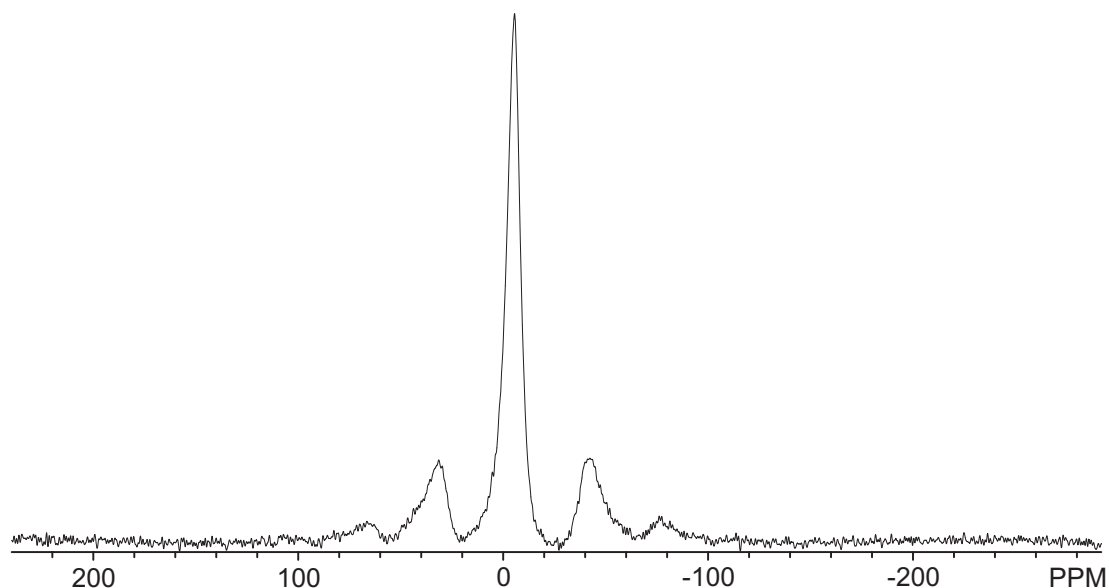


Figure 5.2: ^{19}F MAS NMR spectra for a CaF_2 sample milled for 16 h and recorded at a spinning rate of 16 kHz

The next step in the analysis by means of NMR spectroscopy is the measurement of the ^{19}F spin-lattice relaxation times. This was done by the use of the saturation-recovery sequence which is briefly described in chapter 2.1.5. The sequence was chosen to keep the experimental time low, even for samples with a very long T_1 . Figure 5.3 shows a series of spectra recorded for different recovery times τ .

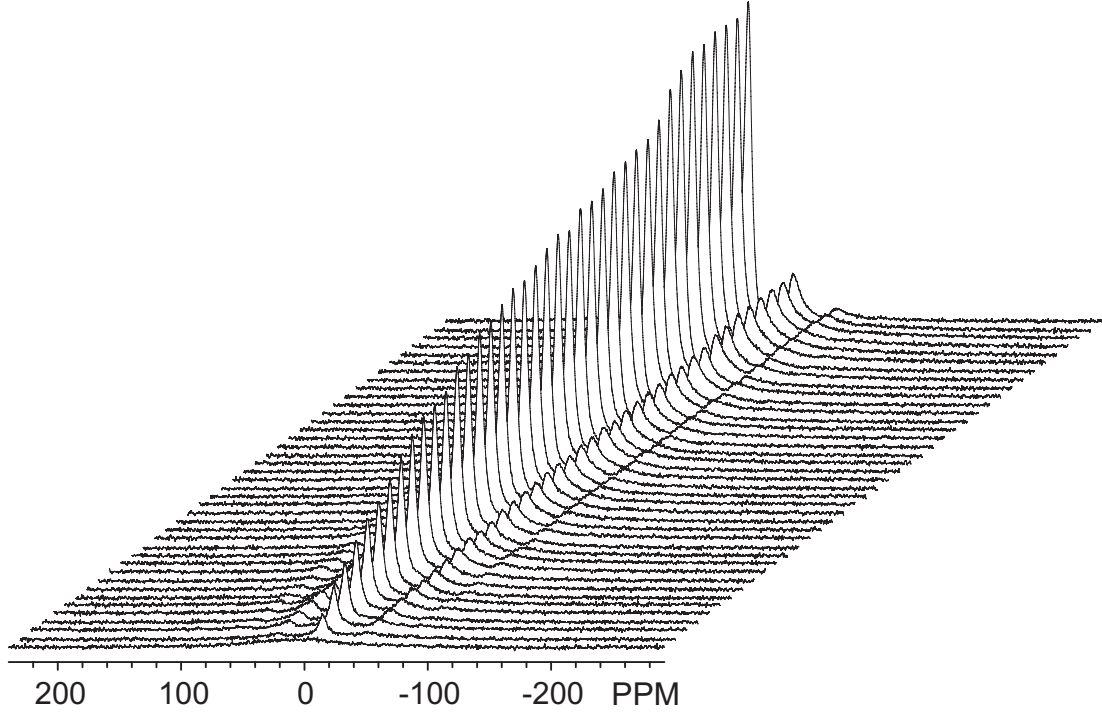


Figure 5.3: ^{19}F MAS NMR spectra for a CaF_2 sample milled for 64 h recorded at a spinning rate of 16 kHz with the saturation-recovery sequence for recovery times τ between 0 s and 16 s

To determine the relaxation time T_1 for a certain sample the integrals of all spectra are extracted and plotted against the recovery time, as shown in figure 5.4 for the sample milled for 32 h. As outlined in chapter 2.1.5 the relaxation time can be extracted by fitting the relaxation data with a mono exponential function:

$$A(\tau) = C [1 - \exp(-\tau/T_1)] \quad (5.1)$$

where A is the normalized extracted integral, C the maximum amplitude, τ the recovery time and T_1 the relaxation time. This procedure works perfectly for the non-milled as well as for the samples milled for 16 h, 32 h and 64 h. The analysis leads to relaxation times of 0.54 s, 0.79 s and 0.31 s, respectively.

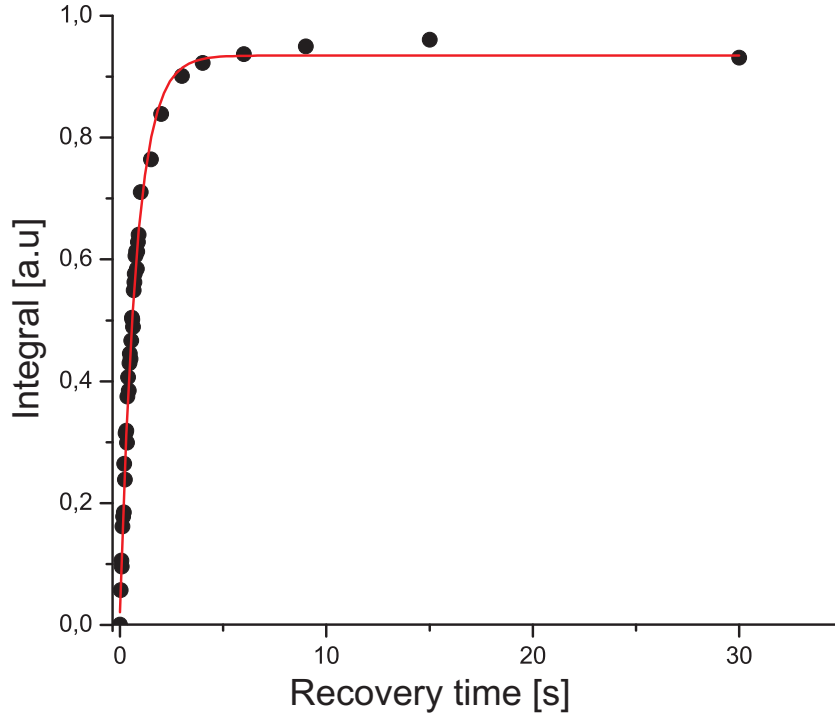


Figure 5.4: Extracted relaxation data for the sample which was ball-milled for 32 h and the curve fitted by function 5.1.

For the relaxation data extracted for the samples milled for 4 h and 8 h formula 5.1 is not suitable to achieve a high degree of correlation. The best fitting result for the sample milled for 8 h is shown in figure 5.5, revealing a large discrepancy in the intermediate recovery time range.

For these samples a different approach is needed to describe the relaxation process in a convenient way. Taking into account the already proposed inhomogeneity for samples milled for shorter time intervals, a biexponential formula was used to adapt the experimental data:

$$A(\tau) = C [1 - \exp(-\tau/T_{1,A})] + (C - 1) [1 - \exp(-\tau/T_{1,B})] \quad (5.2)$$

Where A is the normalized extracted integral, C the amplitude for component A, τ the recovery time and $T_{1,B}$ and $T_{1,A}$ the relaxation time for component B and A, respectively. Figure 5.6 shows the fitting result for the 8 h sample in comparison to the monoexponential approach. A high degree of conformity is found and two components with relaxation times of 20.52 s and 3.15 s are found.

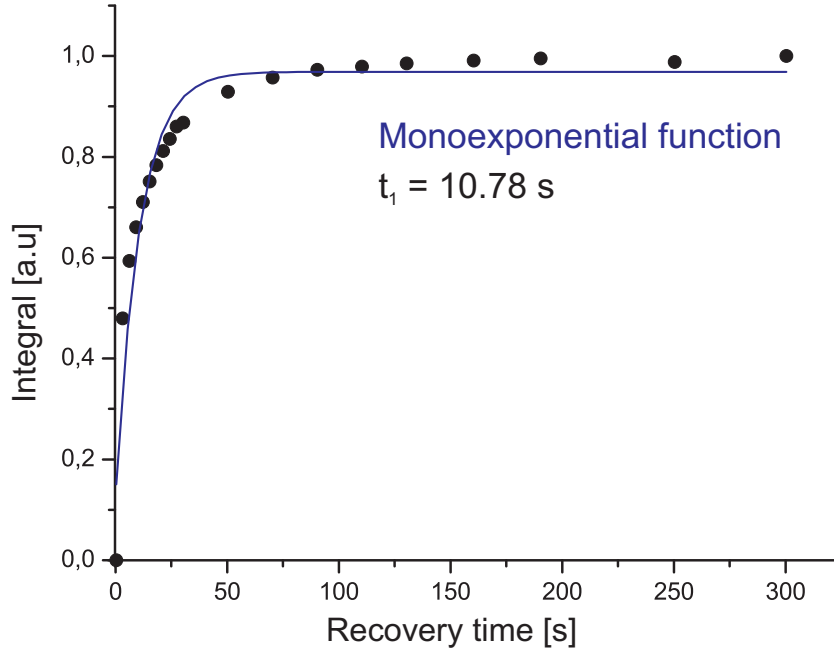


Figure 5.5: Extracted relaxation data for the sample ball-milled for 8 h and the best fitting curve for function 5.1.

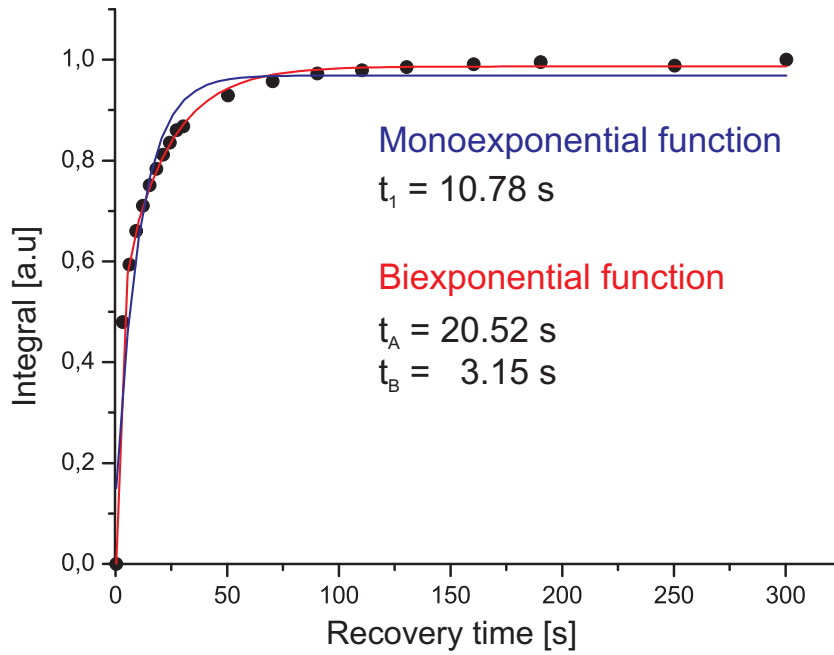


Figure 5.6: Extracted relaxation data for the sample ball-milled for 8 h and the fitting curve for the biexponential function 5.2 in comparison with the monoexponential function 5.1.

By the use of the two functions 5.1 and 5.2 it is possible to analyse the relaxation data of all samples. The overall results are shown in table 5.2 and plotted against the milling time in figure 5.7. For the non-milled CaF_2 a long relaxation time of 54 s is found. When the milling starts, the relaxation time splits up in two components which are both decreasing. After milling for 32 h the relaxation behaviour can be described by a relaxation time below one second.

Table 5.2: Relaxation times for samples milled for different intervals

Milling time [h]	Component	Relaxation time	
		Component A [s]	Component B [s]
0	A	54	—
4	A	20.64(1)	2.59(1)
8	A	20.52(1)	3.15(1)
16	A	—	0.54(1)
32	B	—	0.79(1)
64	B	—	0.31(1)

The analysis of the relaxation data also gives information about the relative amounts C and $(1 - C)$ of the two components. The results are shown in figure 5.8. Already after 4 h the amount of component B strongly decreases in benefit of component A and is still present in the sample milled for 8 h. Between 8 h and 16 h of milling component A disappears completely and only component B is left.

In contrary to the WPPM the ^{19}F relaxometry is able to distinguish between two components present for milling intervals of 4 h and 8 h. However, at this point it is only possible to speculate about the nature of the two components. It clearly could be possible that for short milling times two phases are present which are related to two different types of fluorine atoms distinguishable by their relaxation behaviour. Nevertheless, there are several other situations which could explain the two component relaxation behaviour, e.g. it is known that for nanoscopic materials bulk- and surface atoms can be related to two different relaxation times.

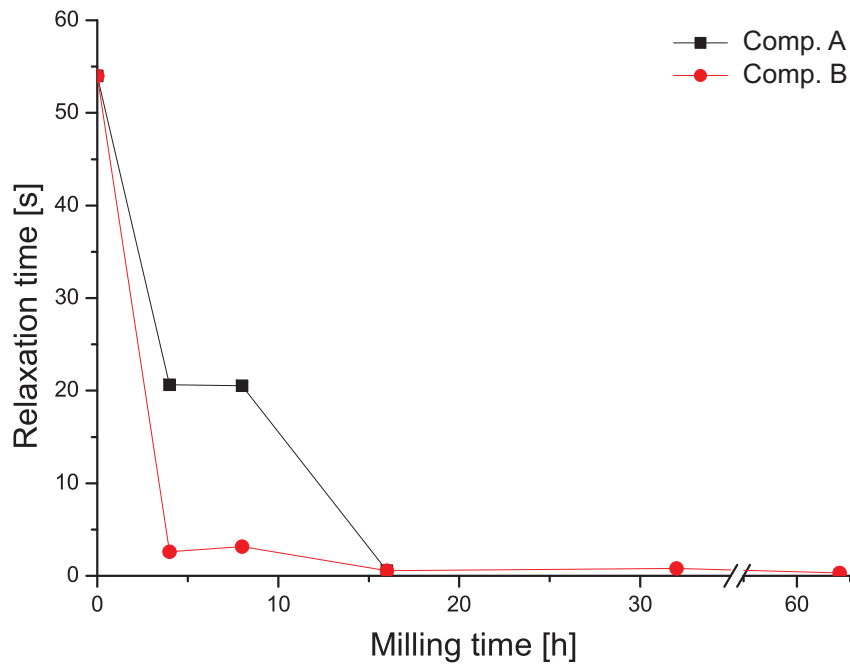


Figure 5.7: Dependency of the T_1 relaxation time on the milling time, revealing a splitting in two components for samples milled for 4 h and 8 h (the area between 35 h and 55 h is skipped)

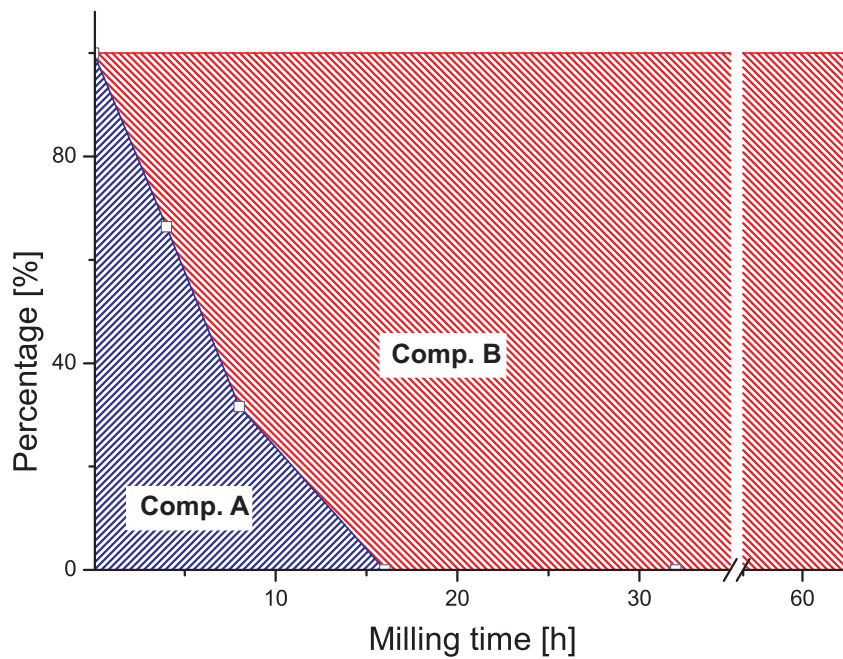


Figure 5.8: Development of the relative amount of the two components determined by the analysis of the relaxation data (the area between 35 h and 55 h is skipped)

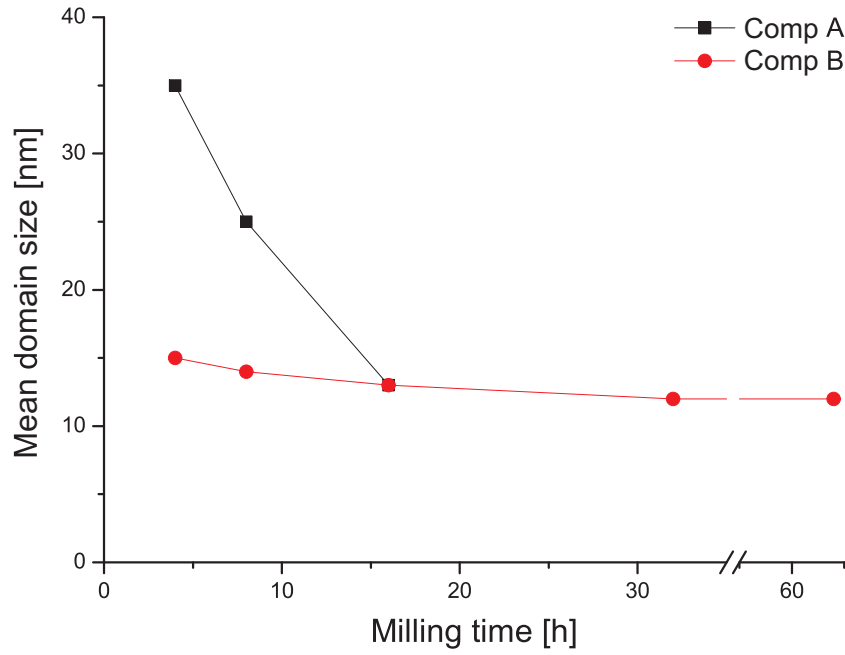


Figure 5.9: Dependency of the mean domain size on the milling time, revealing a splitting in two components for samples milled for 4 h and 8 h (the area between 35 h and 55 h is skipped)

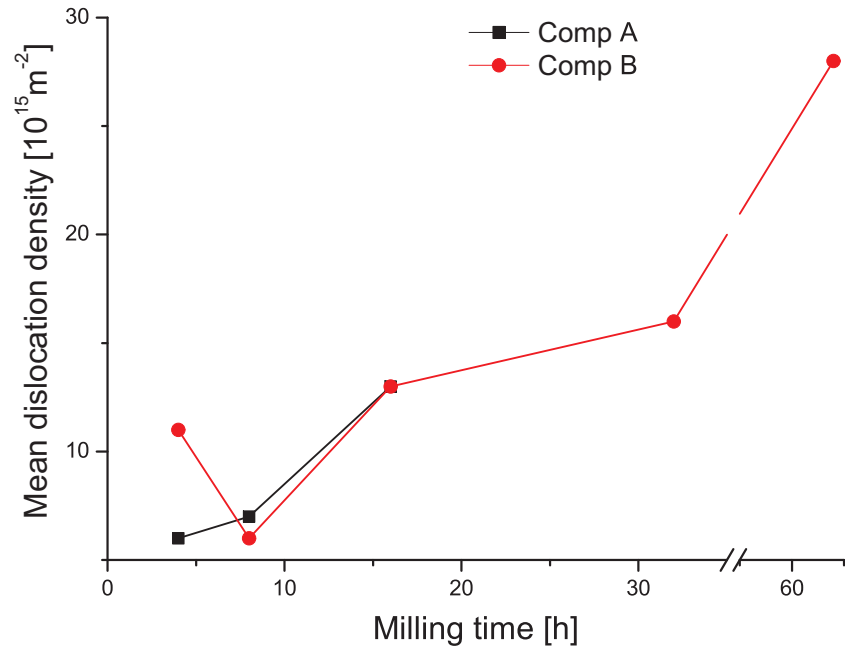


Figure 5.10: Dependency of the mean dislocation density on the milling time, revealing a splitting in two components for samples milled for 4 h and 8 h (the area between 35 h and 55 h is skipped)

To overcome this problem the idea is to use the NMR relaxation data to stabilize the WPPM, i.e. fitting of the relaxation data using the PM2K software simultaneously with the modelling of the X-ray powder pattern. The basic concept is to model a two phase system for the intermediate milling times and give high weight to the relaxation data with respect to the relative amounts of the two phases. In fact, the WPPM for the samples milled for 4 h and 8 h was stabilized in a strong way by the NMR data, resulting in a stable and robust modelling for the NMR and XRD data. The overall results for both techniques are shown in table 5.3. Figure 5.7 and 5.8 show the relaxation times and the relative amount of the phases, respectively. The results for the mean domain size and the mean dislocation density are visualized in figure 5.9 and 5.10, respectively.

Table 5.3: Results of the combined modelling of the XRD and Solid State NMR data for samples differing in their milling time. Two phases (A, B) were considered for 4 h and 8 h of milling. Estimated standard deviations are reported in parentheses, referred to the last significant digits.

Milling time		Lattice	Mean dislocation	Mean domain	T_1	C
[h]		parameter	density	size		
		[nm]	[10^{15} m^{-2}]	[nm]	[s]	[%]
4	A	0.54657(2)	6(1)	35(6)	20.639(1)	66.4
	B	0.54655(4)	11(3)	15(5)	2.593(1)	33.6
8	A	0.54659(6)	7(3)	25(11)	20.520(1)	31.6
	B	0.54657(3)	6(1)	14(4)	3.154(1)	68.4
16		0.54648(1)	13(1)	13(1)	0.54(1)	100
32		0.54646(1)	16(1)	12(1)	0.79(1)	100
64		0.54646(1)	28(3)	12(1)	0.31(1)	100

Already after 4 hours of milling two phases are present, namely phase A and B. Phase A is characterised by a relatively high mean domain size of 35 nm and a low mean dislocation density of $6 \cdot 10^{15} \text{ m}^{-2}$. The relaxation time is reduced from 54 s for the non-milled sample to 20.64 s. The second phase is characterized by a much lower domain size of 15 nm, a nearly twice as high dislocation density of $11 \cdot 10^{15} \text{ m}^{-2}$ and a much shorter relaxation time of 2.59 s. At this time phase A is still dominant with a relative amount of 66.4%. While the milling time is increased, the amount of phase

A decreases to 31.6% in the sample milled for 8 h. The mean domain size decreases with increasing milling time, whereby the decrease is stronger in phase A than in phase B. (A: 35 nm \rightarrow 25 nm, B: 15 nm \rightarrow 14 nm) The mean dislocation density slowly increases in phase A and B. For phase A the values stay below $10 \cdot 10^{15} \text{ m}^{-2}$, while the mean dislocation density in phase B after 8 hours of milling is already found to be $12 \cdot 10^{15} \text{ m}^{-2}$. The relaxation times found for phase B are much shorter than the relaxation times for phase A and are found to be approximately 20 s and 3 s for phase A and B, respectively. After 16 h of milling, phase A has completely disappeared and the system consists of one homogeneous phase again characterized by a mean domain size between 12 nm and 13 nm. Further milling is not affecting the mean domain size, but a further increase of the dislocation density from $13 \cdot 10^{15} \text{ m}^{-2}$ to $28 \cdot 10^{15} \text{ m}^{-2}$ can be observed leading to relaxation times of 0.54 s, 0.79 s and 0.31 s for 16 h, 32 h and 64 h of milling, respectively.

These results allow us to give a clear description of what happens during the milling process. In the beginning, the CaF_2 can be described as a microcrystalline material with a relatively low dislocation density. During the first period of the milling process two phases are formed which differ in their mean domain size and their mean dislocation density. As mentioned in the beginning the dislocations can be caused by the mechanical impact of the milling balls. This means, that the milling is simultaneously grinding the material and introducing dislocations. So on the one side there are less ground grains with a lower dislocation density and on the other side smaller grains with a higher dislocation density induced by the higher mechanical force they have been exposed to. This is true up till 8 h of milling. After milling for 16 h the system is homogenized with respect to the mean domain size, which is a known effect from ball milling. From this point on, further ball milling only causes an increase of the mean dislocation density caused by mechanical forces. So in general one can distinguish three sections during the milling process:

- Microcrystalline material with a low dislocation density
- From between 0 h and 4 h till between 8 h and 16 h a two phase situation is found, with two phases which differ in defect concentration and crystallite size:
 - Larger domains with low dislocation density
 - Smaller domains with higher dislocation density

- From between 8 h and 16 h only one phase is present with a small average domain size and a high dislocation density which is further increasing with milling time.

5.3.2 Discussion of the relaxation effects

At this point one could think about how the microstructural parameters can be related to the spin-lattice relaxation times. Both properties, the mean dislocation density and the mean domain size are known to affect the relaxation time. On the one side a decrease of the particle size down to a nanoscopic level is related to a non-negligible increase of the surface to bulk ratio which in turn is strongly affecting the local surrounding of a certain nucleus, i.e. an atom site in the bulk is distinguishable from an atom in the surface.⁷⁵ Since the relaxation time is strongly influenced by interferences in the local electronic surrounding, this causes a decrease of the relaxation time. On the other side, a similar effect can be caused by distortion in the local electronic surrounding connected to defects in the crystal structure. Before these effects are discussed in a more quantitative manner further results will be shown.

Several batches of nanocrystalline CaF_2 were chemically synthesized by co-precipitation under mild conditions. By doing so, crystals with a very low defect concentration can be grown. These samples allow us to have a look at samples mainly affected by the size effect described above. As described in chapter 5.2, the different chemically synthesized samples differ in the ethanol:water-ratio used for precipitation. All samples were analysed by means of NMR relaxometry and XRD WPPM. The results are shown in table 5.4.

Table 5.4: Results of the combined modelling of the XRD and Solid State NMR data for chemically synthesized samples differing in the water:ethanol-ratio during synthesis. Estimated standard deviations are reported in parentheses, referred to the last significant digits.

Ethanol content	Lattice parameter	Average domain size	T_1
[%]	[nm]	[nm]	[s]
0	0.546636(3)	15(1)	5.1(1)
30	0.546514(2)	12(1)	8.1(3)
60	0.546674(4)	13(1)	4.9(3)
90	0.54675(1)	9.2(3)	5.8(3)
100	0.54764(1)	6.1(2)	0.49(2)

The analysis of the NMR relaxation data leads to only one component for all samples. The X-ray results reveal a decrease of the average domain size for an increasing ethanol:water-ratio. For all samples a relatively wide size distribution is found, which is smaller for samples prepared in high ethanol concentrations (figure 5.11). The relaxation times are found to be between 4.9 s and 8.1 s with the exception of the sample prepared using pure ethanol as solvent for which a very short T_1 of 0.49 s is determined. Having a look at the ^{19}F MAS NMR spectra shown in figure 5.12 allows us to treat this last sample as an outlier. For an ethanol concentration of up to 90% the spectra show one single resonance, as also for the samples prepared by ball milling. If the sample is prepared in pure ethanol the ^{19}F MAS NMR spectrum reveals an extra signal, which can be attributed to a well-defined defect in the crystal structure. In literature a vacancy-interstitial pair (Frenkel defect) on cuboctahedral interstitial site in the unit cell is discussed and found to cause an extra resonance at the position that is also present in the sample prepared in pure ethanol.⁶⁵

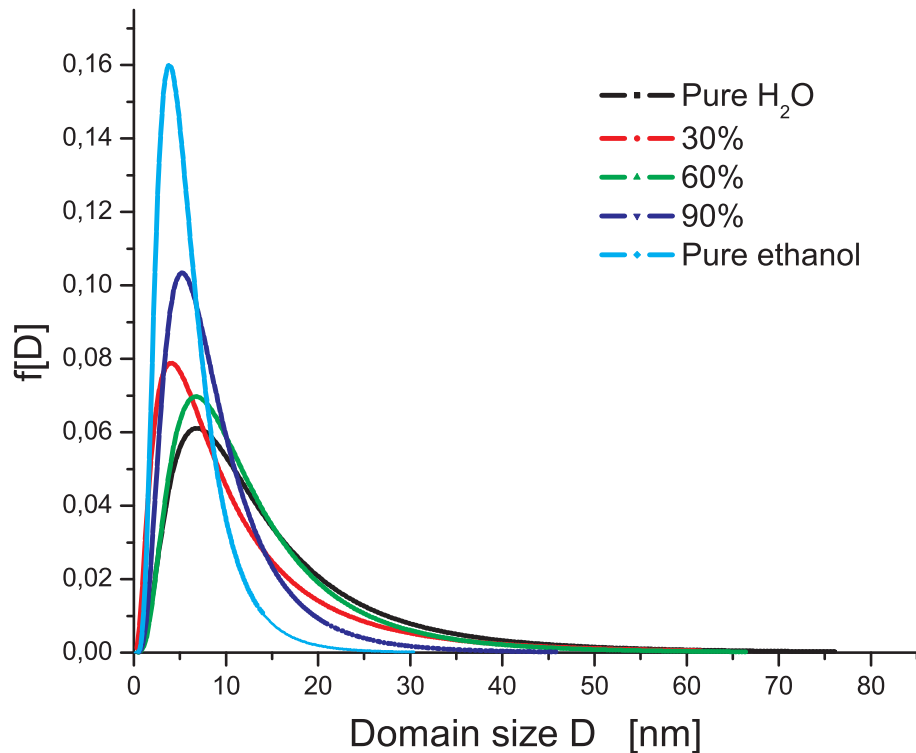


Figure 5.11: Wide size distributions for the samples chemically synthesized in different water:ethanol-ratios

All samples are characterized by a very low average domain size. By performing the precipitation in a solution containing 90% ethanol it is possible to achieve an

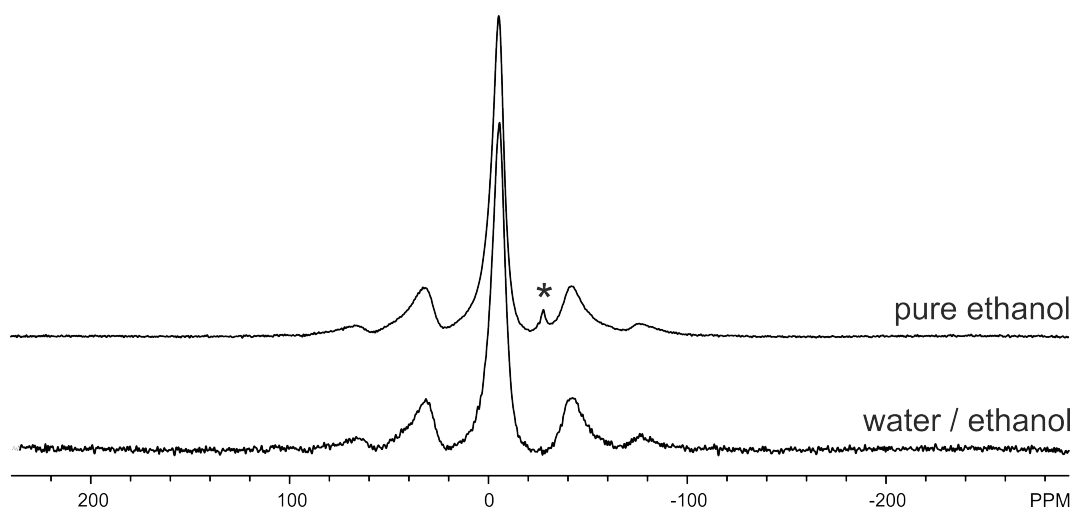
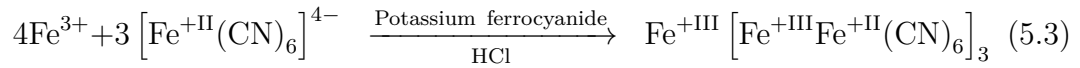


Figure 5.12: ^{19}F MAS NMR spectra for a CaF_2 prepared in a water/ethanol mixture and in pure ethanol. The extra peak present in the one prepared in pure ethanol is marked by a asterisk.

average domain size of 9.2 nm which is below the minimum of 12 nm found for the samples prepared by ball milling. Taking this into account, these results show that the size effect alone only can reduce the relaxation time down to a approximately 5 s. Any further decrease has to be related to the influence of distortions present in the lattice, e.g. dislocations present in the crystal structure. The very low T_1 -value found for the sample produced in pure ethanol inhabiting a high defect concentration confirms this. This observation is consistent with the data found for the ball-milled samples, where only the phases characterized by a high defect concentration and a small mean domain size reveal relaxation times below one second. For the samples milled for longer than 16 h only a further increase of the dislocation density can lead to an additional reduction of the relaxation times, while the mean domain size is not further affected by the ball milling.

5.3.3 CaF₂ milled using steel balls

As described in chapter 5.2, a series of ball-milled CaF₂ has been prepared with steel as vial- and ball material under the same conditions, like the samples prepared by WC. It is known that the influence of iron impurities is negligible for the X-ray measurements. However, the paramagnetic influence of iron on the NMR spectra and parameter is even known to be relatively strong compared to other interactions, as it can be seen in table 2.2. A first step to characterize these samples is the determination of the amount of iron contamination. On a first look the long-milled powders have a light grey colour, and it is not possible to identify isolated iron particles by the use of a microscope. Therefore the iron was complexed as Prussian blue with potassium ferrocyanide (5.3) and as iron thiocyanate by adding potassium thiocyanate (5.4).



Even by judging the colour of the solutions in a qualitative way it is possible to reveal the high concentration of iron in the samples milled for over 16 h (figure 5.13). To quantify the iron contamination, the solutions were analysed by the use of UV/Vis spectroscopy. The results are plotted in figure 5.14. The iron-concentration increases in a linear manner with the milling time. After 64 h of milling a high concentration of more than 1,5 wt% is reached.

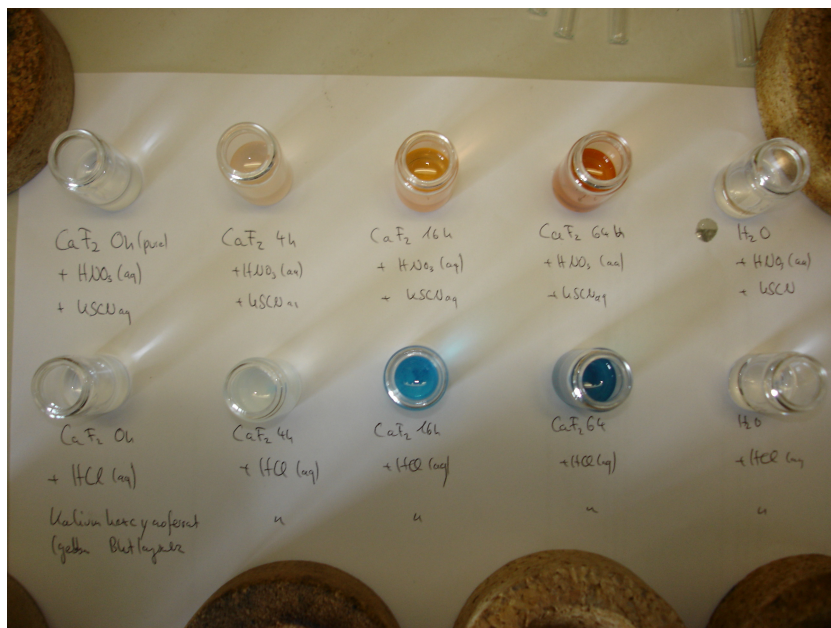


Figure 5.13: Iron analysis as Prussian blue with potassium ferrocyanide (5.3) and as iron thiocyanate by adding potassium thiocyanate (5.4). The milling time increases from the left to the right side and the most right is water as reference.

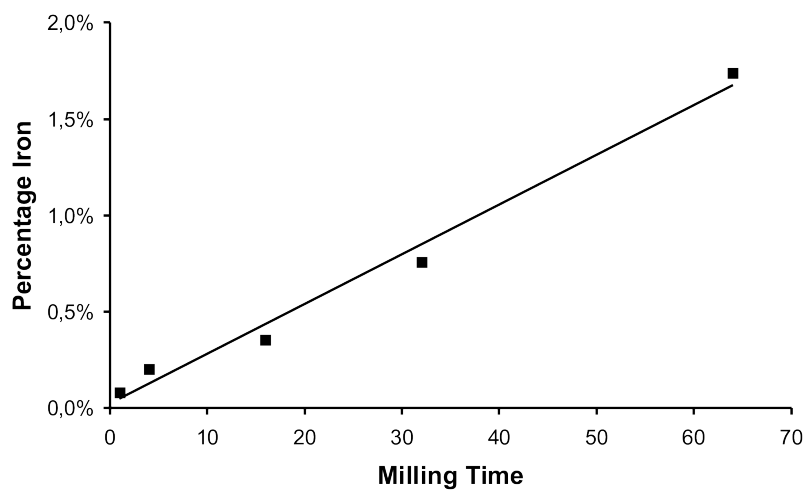


Figure 5.14: Iron concentration [wt%] in the samples milled by the use of iron in dependency of the milling time determined as iron thiocyanate by UV/Vis spectroscopy.

A first thing which will be considered here are the ^{19}F MAS NMR spectra recorded for the iron contaminated samples. Figure 5.15 shows the ^{19}F MAS NMR spectra recorded at a spinning rate of 16 kHz for two samples milled for 16 h under the use of WC and iron material. While the isotropic chemical shift value is the same in both spectra, the CSA is strongly affected by the paramagnetic influence of the iron. The sample milled under the use of steel balls and vial shows more spinning side bands with strongly increased intensities. This effect can be explained by the paramagnetic contribution for the CSA. This strong increase does not only illustrate the presence of iron, but can be also seen as evidence for a homogeneous distribution of iron in the samples. A less homogeneous distribution could not explain the strong paramagnetic influence present in the spectra.

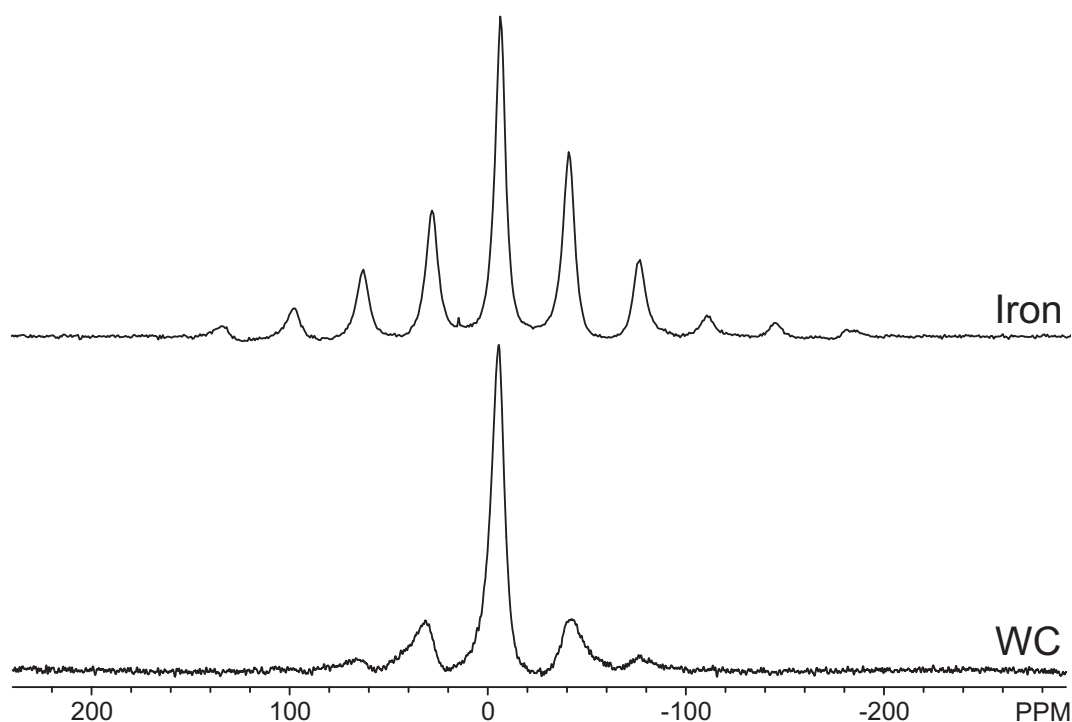


Figure 5.15: ^{19}F MAS NMR spectra recorded at a spinning rate of 16 kHz for two samples milled for 16 h under the use of WC and steel material. The higher noise in the lower spectrum is caused by a lower number of signal accumulations.

Further-on the iron contaminated samples were examined in the same way as the powders which were milled under the use of WC. First of all, this was done to validate the combination of XRD WPPM and NMR relaxometry for these samples and if possible to compare the milling performance of steel and WC. For the steel series the XRD WPPM lead to a one phase model for the samples milled for 32 h and

64 h. For the 32 h sample a mean domain size of 10.7 nm and a mean dislocation density of $16.6 \cdot 10^{15} \text{ m}^{-2}$ are found. Milling for 64 h leads to a further slight decrease of the mean domain size to 9.3 nm, while the mean dislocation density is strongly increased to $37.2 \cdot 10^{15} \text{ m}^{-2}$. The T_1 relaxation measurements agree with this observation and reveal a single T_1 component of 0.038 s and 0.036 s, respectively. In comparison to the T_1 values found for the WC samples, this much shorter T_1 below 0.1 s, accommodates the paramagnetic influence of the iron. Table 5.5 summarizes these results.

Table 5.5: NMR and X-ray results for the samples milled by steel for 32 h and 64 h. Estimated standard deviations are reported in parentheses, referred to the last significant digits.

Milling	Lattice	Mean	Mean	T_1
time	parameter	dislocation density	domain size	
[h]	[nm]	$[10^{15} \text{ m}^{-2}]$	[nm]	[s]
32	0.546347	16.6 (9)	10.7 (5)	0.038 (1)
64	0.546247	37.2 (2)	9.3 (4)	0.036 (1)

While it was also possible to describe the sample milled for 16 h by a single component for the samples milled by WC, the 16 h sample milled by steel balls still shows an inhomogeneous behaviour. Again the relaxation data was used to gather information about the relaxation behaviour and the relative amount of the two phases. As done for the WC samples, the relaxation data and the X-ray data were analysed simultaneously using the PM2K software. The overall results are shown in table 5.6. Figure 5.16 and 5.17 show the relaxation times and the relative amount of the phases, respectively. The results for the mean domain size and the mean dislocation density are visualized in figure 5.18 and 5.19, respectively.

Table 5.6: Results of the combined modelling of the XRD and Solid State NMR data for samples milled using steel balls and vial differing in their milling time. Two phases (A, B) were considered for 4 h, 8 h and 16 h of milling. Estimated standard deviations are reported in parentheses, referred to the last significant digits.

Milling time		Lattice	Mean dislocation	Mean domain	T_1	C
[h]		parameter	density	size		
		[nm]	[10^{15} m^{-2}]	[nm]	[s]	[%]
4	A	0.54653(1)	1.2 (3)	61.3 (7)	20.5 (9)	41.2
	B	0.54658 (2)	8.2 (2)	25.2 (9)	1.7 (2)	58.8
8	A	0.54656 (2)	1.1 (1)	13.7 (5)	11.0 (5)	34.4
	B	0.54657 (3)	10.4 (4)	13.2 (3)	0.51 (0)	65.6
16	A	0.54679 (3)	0.5 (1)	12.3 (7)	2.6 (4)	34.4
	B	0.54682 (2)	11.9 (5)	11.3 (0)	0.04 (0)	77.8
32		0.54635 (2)	16.6 (9)	10.7 (5)	0.038 (1)	100
64		0.54625 (2)	37.2 (2)	9.3 (4)	0.036 (1)	100

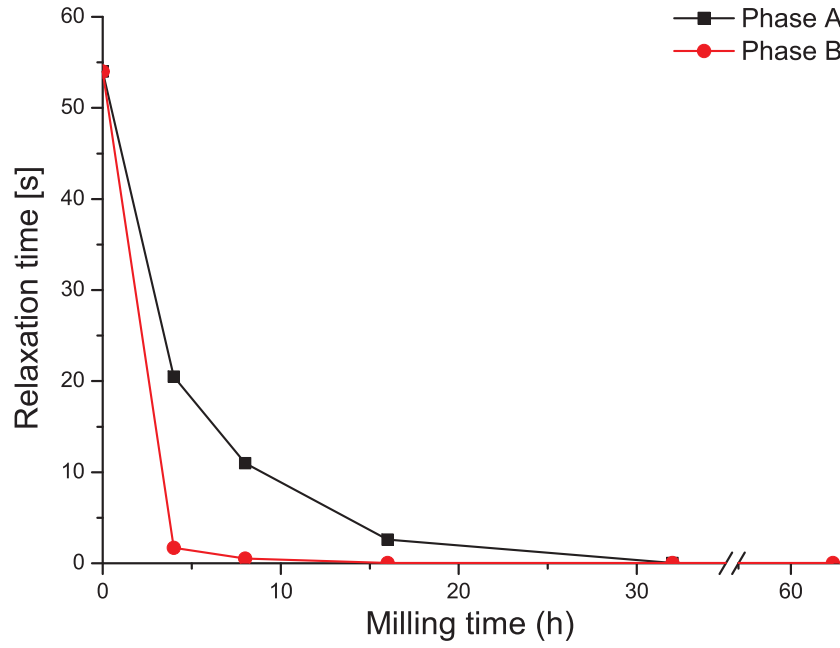


Figure 5.16: The dependency of the T_1 relaxation time on the milling time for the samples milled by steel reveals a splitting in two components for samples milled for 4 h, 8 h and 16 h (the area between 35 h and 55 h is skipped)

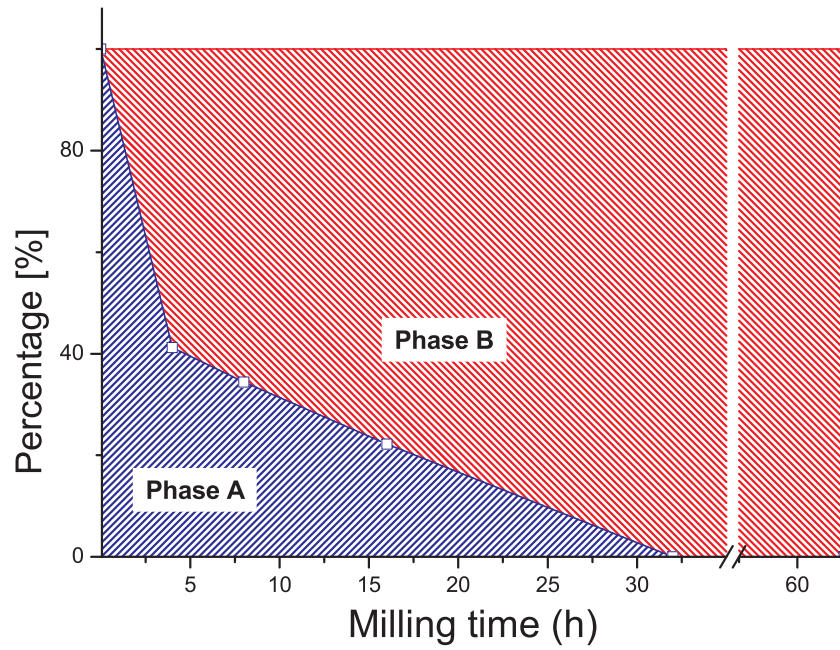


Figure 5.17: Development of the relative amounts of the two components in the samples milled by steel determined by the analysis of the relaxation data (the area between 35 h and 55 h is skipped)

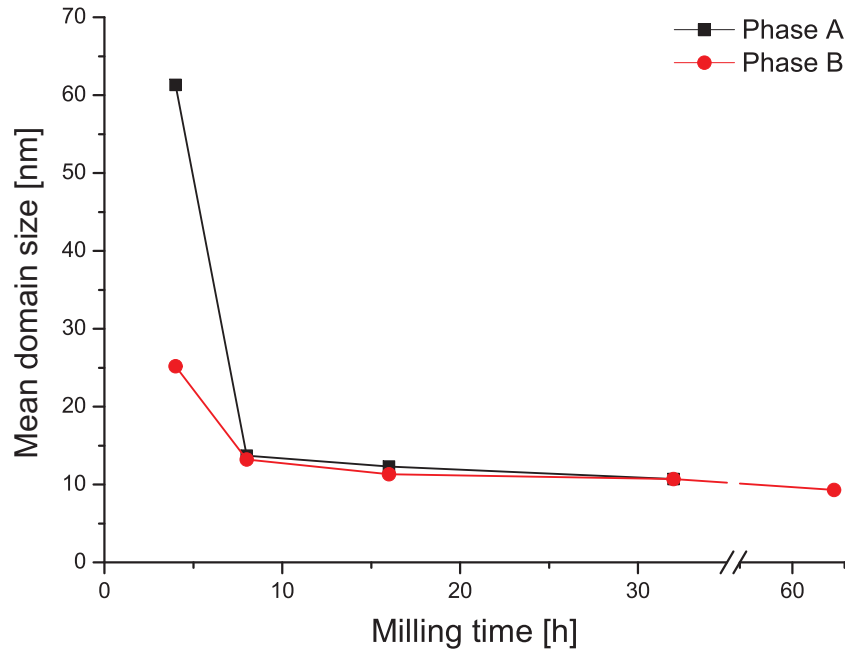


Figure 5.18: Dependency of the mean domain size on the milling time, revealing a splitting in two components for samples milled for 4 h and 8 h (the area between 35 h and 55 h is skipped)

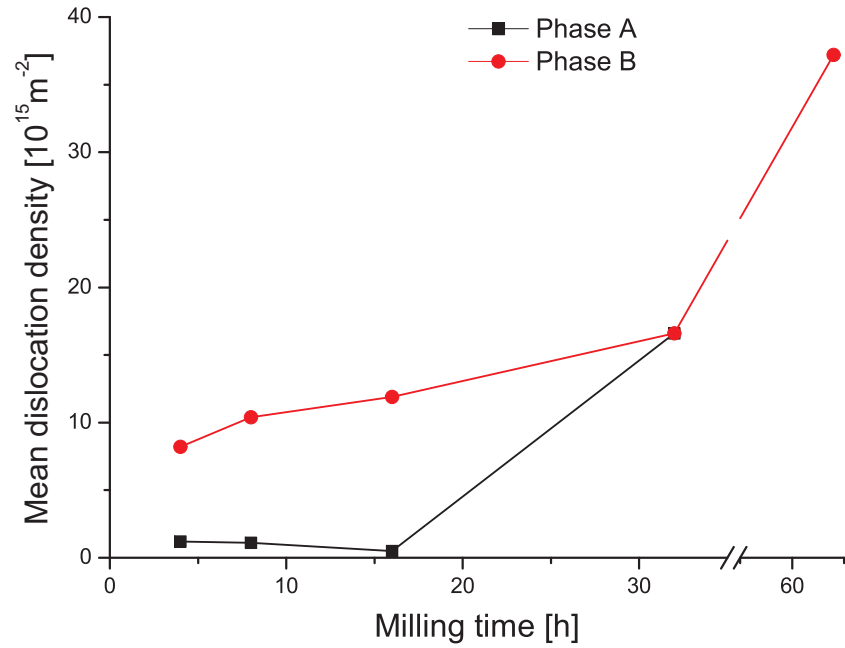


Figure 5.19: Dependency of the mean dislocation density on the milling time, revealing a splitting in two components for samples milled for 4 h and 8 h (the area between 35 h and 55 h is skipped)

As for the samples milled by WC, after 4 hours of milling two phases are present. Phase A is characterized by a relatively high mean domain size of 61.3 nm and a low mean dislocation density of $1.2 \cdot 10^{15} \text{ m}^{-2}$. The relaxation time is reduced from 54 s for the non-milled sample to 20.5 s. The second phase is characterized by a much lower domain size of 25.2 nm, a much higher dislocation density of $8.2 \cdot 10^{15} \text{ m}^{-2}$ and a much shorter relaxation time of 1.7 s. After 4 h of milling phase A is already the minority phase with a relative amount of 41.2%. When the milling time is further increased, the amount of phase A is decreasing, i.e. to 34.4% for the sample milled for 8 h. Certainly, the mean domain size decreases with the milling time, whereby the decrease in phase A is stronger than in phase B, as can be seen in figure 5.18. After 16 h the mean domain size is 12.3 nm and 11.3 nm in phase A and B, respectively. At the same time, the mean dislocation density slowly increases in phase A and B (see figure 5.19). For phase A the values stay below $2 \cdot 10^{15} \text{ m}^{-2}$, while the mean dislocation density in phase B after 4 h of milling is already found to be $8.2 \cdot 10^{15} \text{ m}^{-2}$. The relaxation times found for phase B are much shorter than the relaxation times for phase A. For both phases an increase of the milling time causes a decrease of the relaxation times (see figure 5.16). After 32 h of milling, phase A has completely disappeared and the system consists of one homogeneous phase again, characterized by a mean domain size of 10.7 nm and 9.3 nm for 32 h and 64 h of milling, respectively. Further milling does not affect the mean domain size in a strong way, but a further increase of the dislocation density from $16.6 \cdot 10^{15} \text{ m}^{-2}$ to $37.2 \cdot 10^{15} \text{ m}^{-2}$ is observed, leading to relaxation times of 0.038 s and 0.036 s, respectively.

As for the WC milled samples, these results give a clear description of the structural evolution during the milling process. In the beginning, the CaF_2 can be described as a microcrystalline material with a relatively low dislocation density. During the first period of the milling process two phases are formed which differ in their mean domain size and their mean dislocation density. The milling is simultaneously grinding the material and introducing dislocations, i.e. on the one side there are less ground grains with a lower dislocation density and on the other side smaller grains with a higher dislocation density induced by the higher mechanical force they have been exposed to. Compared to the samples milled by WC, the absolute values for the relaxation times are strongly reduced by up to one order of magnitude for the samples milled for 32 h and 64 h and reveal the strong influence of the paramagnetic iron contamination. However, the overall trend is still present and it is possible to

use the T_1 data to determine the relative amount of the two phases. Contrary to the WC milled samples, the time range for which there are two phases is wider, but again one can distinguish three sections during the milling process:

- Microcrystalline material with a low dislocation density
- From between 0 h and 4 h up to between 16 h and 32 h a two phase situation is found, with two phases that differ in defect concentration and crystallite size:
 - Larger domains with a low dislocation density
 - Smaller domains with a higher dislocation density
- From between 16 h and 32 h up to 64 h of milling, only one phase is present with a small average domain size and a high dislocation density which is further increased with milling time.

5.4 Conclusion

In this chapter it was shown that the positive combination of X-ray diffraction and NMR relaxometry is able to describe the micro- and nanostructural processes during the high energy milling of fluorite. Both, the NMR and XRD data was simultaneously refined using a biexponential function and the WPPM algorithm, respectively. Especially for dealing with inhomogeneous situations, the combination proved its potential. Thereby, the T_1 was able to provide reliable data about the relative amount of the phases, while the XRD WPPM was used to investigate the different parameters of the crystal system, as the lattice parameter, the mean domains size and the dislocation density. In the case of CaF_2 , the combination of both methods revealed high performance with respect to the two phase situations present in the intermediate samples.

Using this new combination analytical approach, it is possible to distinguish three different situations during the grinding of CaF_2 independently of the material used for the high energy ball milling:

- Microcrystalline material with a low dislocation density
- Two phase situation is found, with two phases that differ in defect concentration and crystallite size:
 - Larger domains with a low dislocation density
 - Smaller domains with a higher dislocation density
- Only one phase is present with a small average domain size showing a high dislocation density which is further increased with milling time.

A comparison of the two phase diagrams which can be found in figure 5.20 obtained for the samples milled under the use of steel and WC makes it possible to discuss the "harshness" of the two different materials, when used for the milling balls and vial.

The use of WC leads to a fast decrease of phase A and already after 16 h of milling only phase B is present. In contrary to this, the steel balls cause a slower decrease of the relative amount of phase A which is still present after 16 h of milling. This overall harsher milling behaviour of WC compared to the one of steel can be related to the three times higher stiffness described by a modulus of elasticity of approximately 500 GPa and 196 GPa for WC and steel, respectively. However, the

results for the mean dislocation densities and the mean domain sizes do not fully support this, since both are affected more strongly for the samples milled by the use of steel balls and end up with a smaller mean domain size and a higher dislocation density.

It was also possible to get an idea of the magnitude of the three effects leading to a reduction of the relaxation time T_1 during the milling process. By analysing the chemically synthesised samples, it is possible to demonstrate that the size effect, i.e. the increases of the surface-to-bulk-ratio is capable to reduce the relaxation time in the regime of some seconds, e.g. 5.1 s in the sample prepared in pure water. The influence of the dislocations causes a further decrease down to some tenths of a second, e.g. 0.31 s for the sample milled using WC balls for 64 h. Finally the influence of the homogeneously distributed iron can strongly reduce the relaxation times by up to another order of magnitude, e.g. 0.036 s for the sample ground by steel balls for 64 h. Nevertheless, the trend found for the relaxation times is still present and the data can be used for the simultaneous modelling (Figure 5.21).

As mentioned in chapter 5.1 there is a recent publication which also deals with the ball milling of CaF_2 by means of NMR and XRD.⁶⁷ It is difficult to compare the milling conditions, but it seems that in this publication comparably rough conditions with milling times up to only 16 h were used for the sample preparation. In this publication also a broadening in the XRD powder patterns is described, but the effect was not further investigated. The mean domain sizes are reported to go down to approximately 50 nm with a wide particle size distribution even for the extensively milled samples. Concerning the ^{19}F MAS NMR spectroscopy, they show the presence of two species separated by approximately 3 ppm and determined by deconvolution of the spectra recorded at a spinning rate of 30 kHz. It is possible that we were not able to achieve a resolution high enough to distinguish the two signals due to the lower spinning rate. The T_1 analysis in this publication was performed with respect to the main resonance exclusively, leading to a minimum T_1 value of 3.4 s. It is likely that the milling done by them was not harsh and long enough to fully reach, nor overcome the two-phase situation. The observance of a monoexponential relaxation behaviour for all samples found in this publication could be explained by the omittance of the minor resonance likely related to the dislocations formed in the crystals.

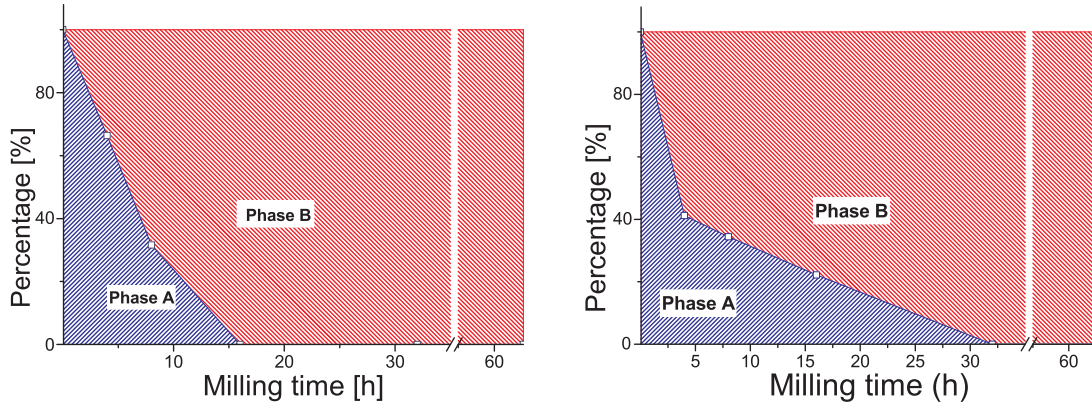


Figure 5.20: Comparison of the phase-diagrams found for the milling with WC (left graph) and steel (right graph) as material for balls and vial

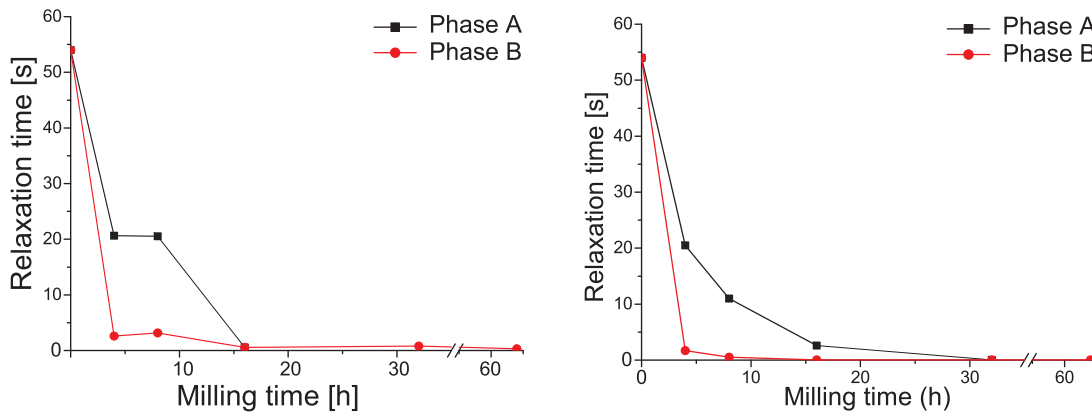


Figure 5.21: Comparison of the relaxation times found for the milling with WC (left graph) and steel (right graph) as material for balls and vial

6 Summary

The present thesis is divided into three chapters dealing with different aspects of the application of solid-state NMR as an analytical tool in material science instead of keeping the focus on one certain material which could be analysed by several analytical approaches.

Chapter 3 deals with a more methodological subject, namely the optimization of ^{19}F decoupling techniques for fluorinated membranes. In a first step I investigated the characteristics of the commonly used XY-16 decoupling scheme. By determination of the decoupling efficiency in dependency of the decoupling frequency an oscillating off-resonance behaviour was found, i.e. an opposite periodic behaviour for signal intensity and width. The intensity maxima, correlated to signal width minima, are located at offsets which are integer multiples of the spinning rate. The presented results show the possibility to further improve the high decoupling efficiency of the XY-16 decoupling scheme for fluoropolymers reported in literature by exploiting exactly this modulating off-resonance behaviour with maxima in intensity for $\Delta\nu_{dec} = n\nu_r$, while preserving the full width half maximum (FWHM) found for on-resonance decoupling. For a Nafion[®] sample one can achieve 20% gain in intensity with constant line width for a -50 kHz decoupling frequency offset at MAS rate of 25 kHz. Figure 6.1 shows the oscillating offset characteristics for an activated Nafion[®] sample and $^{13}\text{C} \{^{19}\text{F}\}$ NMR spectra recorded with and without the exploit of the off-resonance effect revealing the gain in intensity under conservation of the FWHM.

The oscillating effect can be explained by the high CSA found for the ^{19}F nuclei in the samples, i.e. the MAS is not able to fully average this interaction and the residual spinning side-bands in the ^{19}F spectrum are directly irradiated when the offset is a multiple of the spinning rate.

The high isotropic chemical shift dispersion and high CSA for ^{19}F gave rise to the idea that the pulses in the XY-16 sequence are not able to provide a sufficient spin inversion for the full ^{19}F spectrum. It was possible to show that the use of

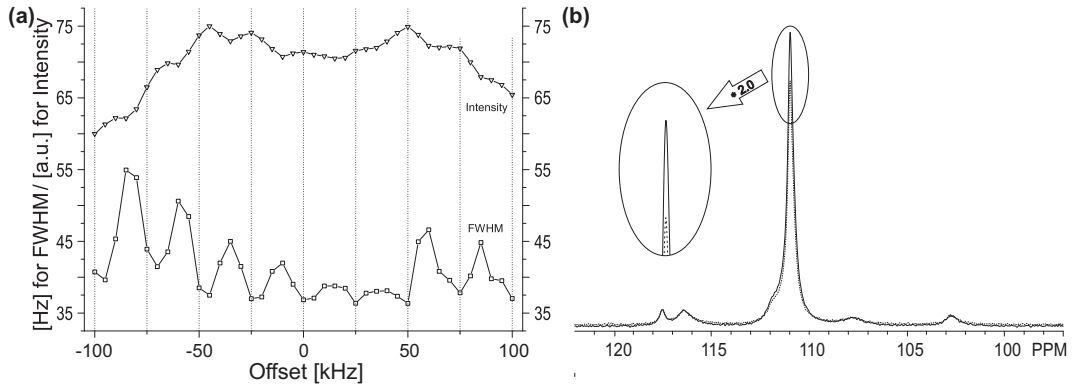


Figure 6.1: (a) Offset characteristics of XY-16 showed for the CF_2 of Nafion[®] at 25 kHz and (b) Nafion[®] spectra recorded for on- (dashed line) and off-resonance (solid line) decoupling

broadband composite pulses, like $90_x270_y90_y$ or $336_x246_{-x}10_y74_{-y}10_y246_{-x}336_x$ can further increase the line width of PTFE by ~ 1.5 Hz at a spinning rate of 20 kHz.⁴⁰ These results can be interesting with respect to systems with a higher dispersion of isotropic chemical shifts and even higher CSAs, in which case the effect could be even higher.

The XY-16 sequence is limited to high spinning rates since the homonuclear interactions are exclusively eliminated by MAS. This fact makes it impossible to use rather large rotors, so the idea was to search for an alternative decoupling scheme which is able to achieve a comparable decoupling efficiency at lower spinning rates. This was achieved by the use of the XiX decoupling scheme. The application of the XiX sequence on fluorinated membranes leads to a line width reduced by 40% compared to spectra recorded under XY-16 decoupling at the same spinning rate of 11 kHz, while a decoupling efficiency which is comparable to XY-16 at much higher spinning rates was achieved (see figure 6.2). In this respect XiX decoupling can be an interesting tool, if spinning is limited to low values $\nu_r < 15$ kHz, e.g. if larger amounts of sample are needed for sensitivity reasons or if it is not possible to pack foil-like samples into very small rotors.

The second part of the present thesis deals with the quantification of data obtained by the application of cross-polarization NMR spectroscopy on membranes for the use in polymer electrolyte fuel cells. A cheap possibility to produce a proton conducting polymer membrane is the modification of commercially available per-fluorinated or partially fluorinated base films. This can be achieved by radiation grafting during which the desired base film, e.g. PTFE, is electron beam irradiated

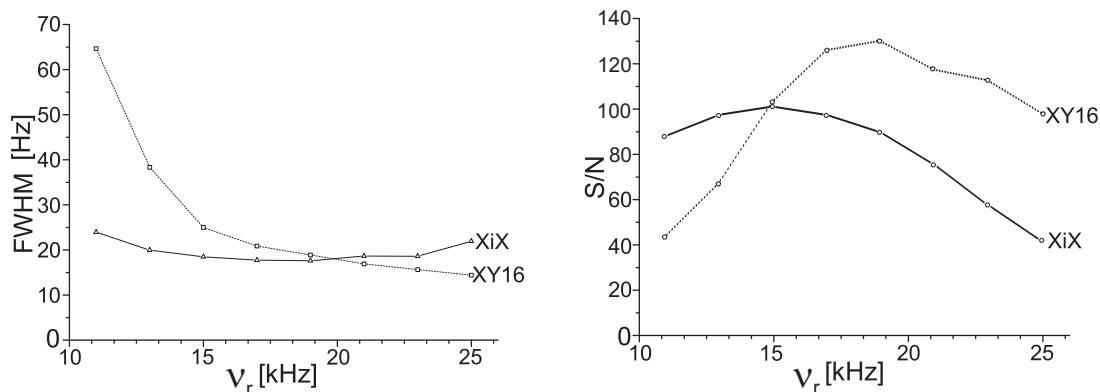


Figure 6.2: FWHM (left) and S/N (right) of the PTFE ^{13}C signal obtained under XY-16 and XiX decoupling at different spinning rates

to produce a certain concentration of radicals in the membrane, which in turn can react with a solution of suitable monomers, e.g. α -methylstyrene (AMS). The films for this work were synthesized by the use of a mixture of AMS and methacrylonitrile (MAN). Normally, the degree of grafting (DoG) is used as parameter for the overall grafting in such reactions. It is the mass-ratio of the reacted grafting component and the original base film mass ($\text{DoG} = (m_{\text{graft}} - m_{\text{base}})/m_{\text{base}}$, where m_{base} is the mass of the irradiated base film and m_{graft} is the mass of the membrane after the grafting reaction.). Since the membranes in this study are formed by the use of a mixture of AMS and MAN, the DoG alone cannot describe the molecular situation in a suitable manner, since it is not capable of describing the ratio of the two components in the membrane. The determination of the AMS:MAN-ratio can be a rather complicated challenge due to the poor solubility of the grafted membranes. For this reason the AMS:MAN-ratio is commonly determined by FT-IR spectroscopy. The FT-IR spectra reveal separate signals for the two components and the ratio can be calculated by the help of previously recorded calibration curves.^{47,48}

One major drawback of this method are the problems which arise from the expansion of the film during the grafting which in turn changes the area considered in the FT-IR measurements and leads to the exigency of a factor correcting this behaviour. I was able to show that the exact ratio can be determined by $\{^1\text{H}\}^{13}\text{C}$ CP NMR spectroscopy.

The first step in achieving the AMS:MAN-ratio by means of $\{^1\text{H}\}^{13}\text{C}$ CP NMR spectroscopy was the full signal assignment for the $\{^1\text{H}\}^{13}\text{C}$ CP NMR spectra and the results are shown in figure 6.3.

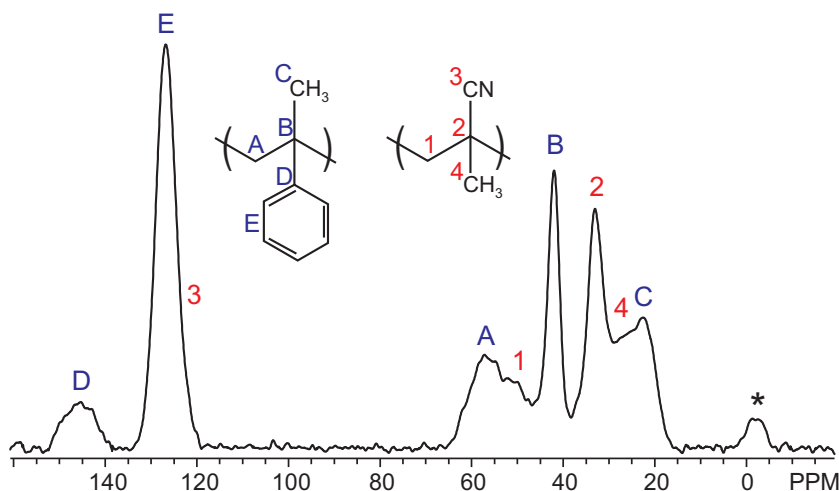


Figure 6.3: $\{^1\text{H}\}^{13}\text{C}$ CP NMR spectrum for a sample grafted with a MAN/AMS mixture.

The best signal separation was found for the two quaternary carbons in an α -position to the phenyl ring (assignment B in figure 6.3, 42 ppm) and next to the cyano group (assignment 2 in figure 6.3, 33 ppm). Also the fact that both are quaternary carbons and that it seems likely that both inhabit similar CP dynamics gave reason to use them for the determination of the AMS:MAN-ratio. This new approach for the determination of the AMS:MAN-ratios for the peaks at 33 ppm and 42 ppm was done in three steps:

- Acquisition of the $\{^1\text{H}\}^{13}\text{C}$ CP NMR spectra for all membranes for a fixed CT of 5 ms.
- Acquisition of the CP build-up curves, i.e. the signal integrals for different contact times, for selected samples to show that the ratio is independent from the chosen CT.
- Acquisition of the ^{13}C single pulse NMR spectra for the same selection of membranes to prove that the ratio determined by the CP spectra is not affected by the possibly different CP dynamics of the signals at 33 ppm and 42 ppm.

The deviation for the AMS:MAN-ratio obtained by NMR is found to be below 5% with respect to the CT and the value obtained by ^{13}C SP spectroscopy. The results for the membrane with DoG of 44% are plotted in figure 6.4. The values obtained by FT-IR spectroscopy and the ^{13}C SP spectra are also plotted in this graph.

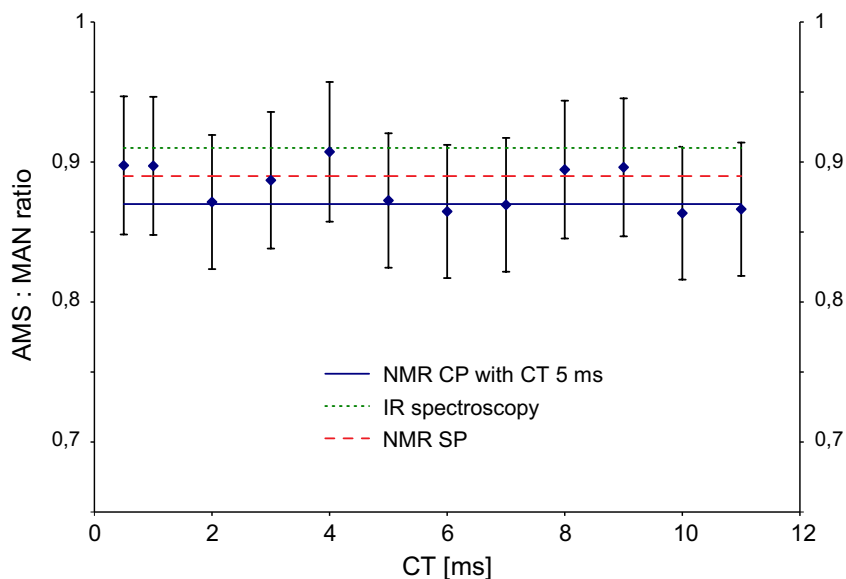


Figure 6.4: AMS:MAN-ratio in dependency of the CT with the respective error bars assuming an error of 6 %. The values obtained by FT-IR spectroscopy and the ^{13}C SP spectra are shown as horizontal lines.

The standard deviation for the molar AMS:MAN-ratio is found to be 5% for the values obtained by FT-IR spectroscopy. The values obtained by FT-IR spectroscopy and the ^{13}C SP spectra lay within the 6% error bars added to the CP dataset. The first thing to notice here is the good agreement between all three different methods. Table 6.1 combines the results for the AMS:MAN-ratio in dependency on the DoG obtained by the use of FT-IR, $\{^1\text{H}\}^{13}\text{C}$ CP and ^{13}C single pulse spectra.

The values for the AMS:MAN-ratio determined by the three different techniques reveal a high degree of consistence for all different membranes. However, the values obtained by FT-IR spectroscopy exhibit an uncertainty, since the values are corrected by an approximated expansion factor, while the values obtained by $\{^1\text{H}\}^{13}\text{C}$ CP possess a certain measurement inaccuracy caused by the slightly different CP dynamics of the signals used for the ratio calculation. Only in comparison with the values extracted from the ^{13}C SP spectra, both methods reveal a high degree of accuracy.

With respect to the good agreement of the values obtained by ^{13}C NMR and FT-IR spectroscopy, the latter will be further used as routine method to determine the monomer ratio, while the so far approximated expansion factor can now be calculated from the results of the exact ^{13}C SP NMR measurements. Nevertheless, the determination of the ratio by $\{^1\text{H}\}^{13}\text{C}$ CP NMR spectroscopy can still be an

Table 6.1: Results for the AMS:MAN-ratio in dependency on the DoG obtained by the use of the FT-IR $\{^1\text{H}\}^{13}\text{C}$ CP and ^{13}C single pulse spectra

Molar AMS:MAN-ratio			
DoG [m%]	in the grafted polymer obtained by		
	FT-IR	$\{^1\text{H}\}^{13}\text{C}$ CP	^{13}C SP
5	0.84	0.82	—
15	0.85	0.89	—
24	0.91	0.92	—
35	0.92	0.88	0.9
44	0.91	0.87	0.89

interesting alternative for different pairs of monomers or even for mixtures which consist of more than two components.

The last part of this thesis shows the capability of the positive combination of X-ray diffraction and NMR relaxometry to describe the micro- and nanostructural processes during the high energy milling of fluorite. The samples under investigation were prepared by high energy ball milling of commercially available CaF_2 powder. Two series of samples were prepared using WC and Fe as material for the vial and the balls. The milling time was varied from 4 h to 64 h (4 h, 8 h, 16 h, 32 h and 64 h). A third series of samples was prepared by the direct co-precipitation method by the use of CaCl_2 and NH_4F as reactant in an exchange reaction in a mixture of water and ethanol.⁶⁸

For all CaF_2 samples milled for different milling times X-ray powder patterns were recorded. To quantify these features the powder patterns were analysed by the whole powder pattern modelling (WPPM) method which was briefly described in chapter 2.2.2 and is a convenient method to analyse the domain size and lattice strain broadening effects simultaneously.^{62,69} By analysing the powder patterns by WPPM with the PM2K software^{25,62,69} the mean dislocation density (ρ) and the effective cut-off radius (R_e) could be determined. When analysing the powder patterns of the samples which have been milled relatively long, the WPPM gave satisfactory results with a high degree of conformity between the experimental and the theoretical powder diffraction patterns. However, for the powders milled for short milling times the WPPM was not capable of describing the experimental powder pattern in a

sufficient way. It seemed to be likely that for these samples which were milled only for a shorter period, the powders are not homogeneous and a two phase system could be best to describe the situation. But even under this assumption the WPPM was unstable and the parameters for the two phases correlated in a strong way.

This situation was underpinned by the results of the ^{19}F MAS NMR spectroscopy. All spectra show one broad resonance, and strong spinning side bands are found. The spinning side bands, still present at rather high spinning rates, reveal the high CSA found for the samples.⁷⁴ Unfortunately it was not possible to achieve a spectral resolution high enough to distinguish two or more different fluorine sites. Even at high spinning rates of 28 kHz it was not possible to distinguish between different signals.

The next step in the analysis by means of NMR spectroscopy was the measurement of the ^{19}F spin-lattice relaxation times. This was done by the use of the saturation-recovery sequence which is briefly described in chapter 2.1.5. To determine the relaxation time T_1 for a certain sample the integrals of all spectra were extracted and plotted against the recovery time. Normally the relaxation time can be extracted by fitting the relaxation data with a mono-exponential function.

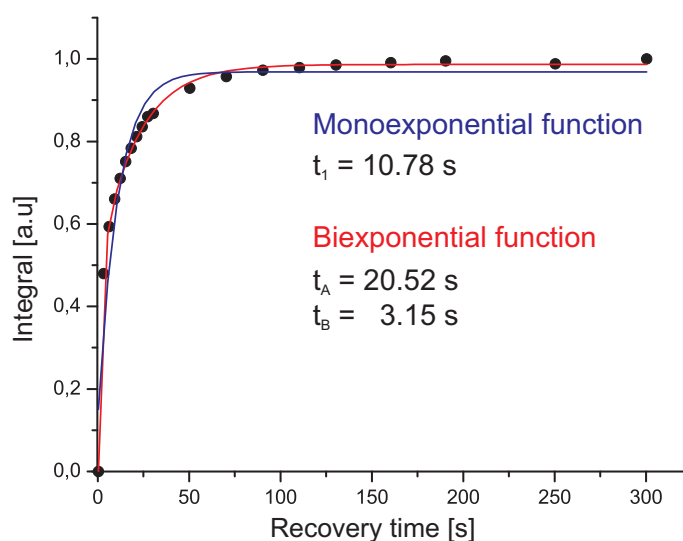


Figure 6.5: Extracted relaxation data for the sample ball-milled by WC balls for 8 h and the fitting curve for the biexponential function in comparison with the monoexponential function.

This was possible with a high degree of conformity for the long-milled samples. As already for the XRD-WPPM, the short-milled samples caused problems in the analysis of the data. For them, a mono-exponential function is not suitable to

achieve a high degree of correlation. The best fitting result for the sample milled with WC balls for 8 h is shown in figure 6.5, revealing a large discrepancy in the intermediate recovery time range.

For these samples a different approach was needed to describe the relaxation process in a convenient way. Taking into account the already proposed inhomogeneity for samples milled for shorter time intervals, a biexponential formula was used to adapt the experimental data. By the use of the two different functions it is possible to analyse the relaxation data of all samples (figure 6.5). The overall results for the samples milled by WC balls are plotted against the milling time in figure 6.6, revealing a splitting in two components for samples milled for 4 h and 8 h.

The analysis of the relaxation data also gives information about the relative amounts C and $(1 - C)$ of the two components. The results for the WC-milled samples are shown in figure 6.6. Already after 4 h the amount of component B strongly decreases in benefit of component A and is still present in the sample milled for 8 h. Between 8 h and 16 h of milling component A disappears completely and only component B is left.

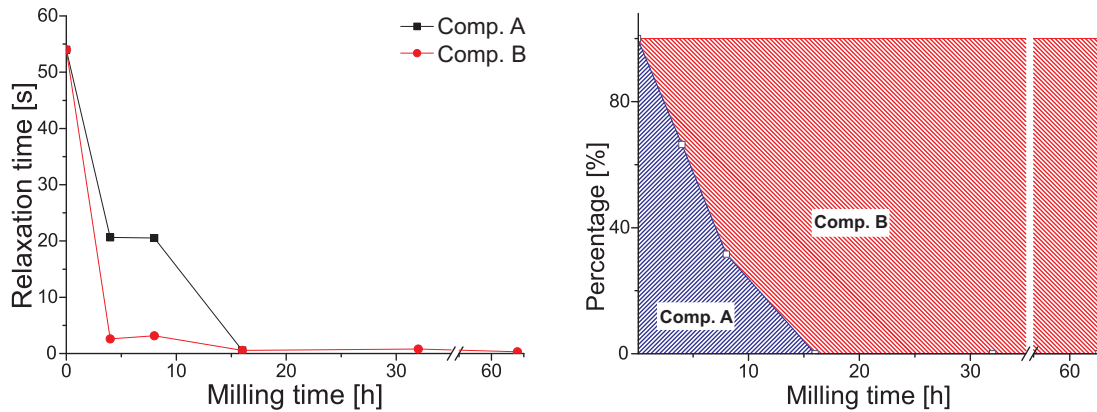


Figure 6.6: Dependency of the relaxation time on the milling time (left side) and the development of the relative amount of the two components (right side). (the area between 35 h and 55 h is skipped)

In contrary to the WPPM the ^{19}F relaxometry is able to distinguish between two components present for milling intervals of 4 h and 8 h. However, at this point it was only possible to speculate about the nature of the two components, e.g. it is known that for nanoscopic materials bulk and surface atoms can be connected to two different relaxation times.

To solve this problem, the NMR and XRD data was simultaneously refined us-

ing a biexponential function and the WPPM algorithm, respectively. Especially for dealing with inhomogeneous situations, the combination proved its potential. Thereby, the T_1 was able to provide reliable data about the relative amount of the phases, while the XRD WPPM was used to investigate the different parameters of the crystal system, as the lattice parameter, the mean domain size and the dislocation density. In the case of CaF_2 , the combination of both methods revealed high performance with respect to the two phase situations present in the intermediate samples.

Based on this information it was possible to give a clear description of what is happening during the milling process. In the beginning, the CaF_2 can be described as a microcrystalline material with a relatively low dislocation density. During the first period of the milling process two phases are formed which differ in their mean domain size and their mean dislocation density. These dislocations are caused by the mechanical impact of the milling balls. This means, that the milling is simultaneously grinding the material and introducing dislocations. So on the one side there are less ground grains with a lower dislocation density and on the other side smaller grains with a higher dislocation density induced by the higher mechanical force they have been exposed to. This is true up till 8 h (WC) or 16 h (Fe) of milling. After milling for longer times the system is homogenized with respect to the mean domain size, which is a known effect from ball milling. From this point on, further ball milling only causes an increase of the mean dislocation density caused by mechanical forces. Using this new combinational analytical approach, it is possible to distinguish three different situations during the grinding of CaF_2 independently of the material used for the high energy ball milling:

- Microcrystalline material with a low dislocation density
- A two-phase situation is found, with two phases that differ in defect concentration and crystallite size:
 - Larger domains with a low dislocation density
 - Smaller domains with a higher dislocation density
- Only one phase is present with a small average domain size showing a high dislocation density which is further increased with milling time.

A comparison of the two phase diagrams which can be found in figure 6.7 obtained

6 Summary

for the samples milled under the use steel and WC, makes it possible to discuss the 'harshness' of the two different materials, when used for the milling balls and vial.

The use of WC leads to a fast decrease of phase A and already after 16 h of milling only phase B is present. In contrary to this, the steel balls cause a slower decrease of the relative amount of phase A which is still present after 16 h of milling. This overall harsher milling behaviour of WC compared to the one of steel can be related to the three times higher stiffness described by a modulus of elasticity of approximately 500 GPa and 196 GPa for WC and steel, respectively. However, the results for the mean dislocation densities and the mean domain sizes do not fully support this, since both are affected more strongly for the samples milled by the use of steel balls and end up with a smaller mean domain size and a higher dislocation density.

It was also possible to get an idea of the magnitude of the three effects leading to a reduction of the relaxation time T_1 during the milling process. By analysing the chemically synthesised samples, it is possible to demonstrate that the size effect, i.e. the increases of the surface-to-bulk-ratio is capable to reduce the relaxation time in the regime of some seconds, e.g. 5.1 s in the sample prepared in pure water. The influence of the dislocations causes a further decrease down to some tenths of a second, e.g. 0.31 s for the sample milled using WC balls for 64 h. Finally the influence of the homogeneously distributed iron can strongly reduce the relaxation times by up to another order of magnitude, e.g. 0.036 s for the sample ground by steel balls for 64 h. Nevertheless, the trend found for the relaxation times is still present and the data can be used for the simultaneous modelling.

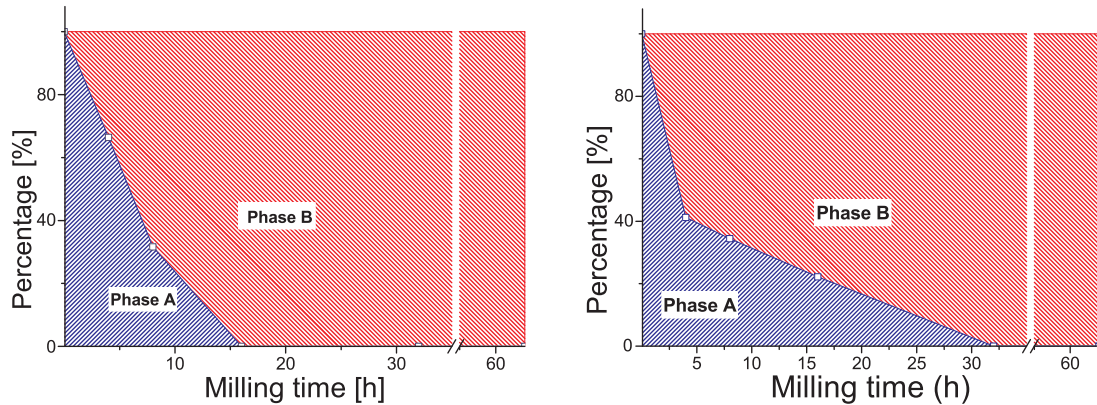


Figure 6.7: Comparison of the phase-diagrams found for the milling with WC (left graph) and steel (right graph) as materials for balls and vial

7 Zusammenfassung

Die vorliegende Doktorarbeit ist in drei Teile unterteilt, welche sich mit verschiedenen Aspekten der Festkörper-NMR (ss-NMR) Spektroskopie beschäftigen. Anstatt eine bestimmte Probenart mit einer Vielzahl von Methoden zu untersuchen, wurden hier verschiedene Materialien für die unterschiedlichen ss-NMR-Methoden verwendet.

Kapitel 3 beinhaltet einen eher methodischen Aspekt der ss-NMR-Spektroskopie, nämlich die Optimierung von ^{19}F -Entkopplungstechniken für die Anwendung an fluorierten Membranen für den Einsatz in Brennstoffzellen. Der erste Teil dieses Kapitels beschäftigt sich mit der Optimierung der XY-16-Entkopplungssequenz, welche für solche Materialien Anwendung findet. Durch die genaue Untersuchung der Abhängigkeit der Signalintensitäten und Signalbreiten der ^{13}C -Resonanz einer Polytetrafluoroethylen- (PTFE) und einer Nafion[®]-Probe von der Entkopplerfrequenz konnte ein oszillierendes Verhalten der Entkopplungseffizienz entdeckt werden. Wenn der Abstand der gewählten Entkopplungsfrequenz zur isotropen chemischen Verschiebung des Fluors einem Vielfachen der Probenrotation entspricht, findet man Maxima in der Signalintensität, beziehungsweise Minima in der Signalbreite. Die vorgestellten Ergebnisse verdeutlichen die Möglichkeit, die Signalintensität unter Erhaltung der geringen Signalbreite mit Hilfe dieser "Offset"-Bedingung zu optimieren. Im Falle der Nafion[®]-Probe konnte unter Erhaltung der Signalbreite ein Intensitätsgewinn von 20% erzielt werden. Abbildung 7.1 verdeutlicht das oszillierende Verhalten der Signalbreite und der Signalintensität und zeigt den möglichen Intensitätsgewinn an einem $^{13}\text{C} \{^{19}\text{F}\}$ -NMR-Spektrum einer aktivierten Nafion[®]-Probe.

Die Oszillationen können durch die hohe chemische Verschiebungsanisotropie (CSA) erklärt werden. Die Probenrotation im magischen Winkel (MAS) ist somit nicht in der Lage diese Wechselwirkung vollständig zu eliminieren und es bleiben selbst bei relativ hohen MAS-Geschwindigkeiten Rotationsseitenbänder im ^{19}F -NMR-Spektrum präsent. Eine hohe Entkopplungseffizienz ist in diesem Fall dann zu finden, wenn die gewählte Frequenz exakt auf einem Seitenband positioniert wird.

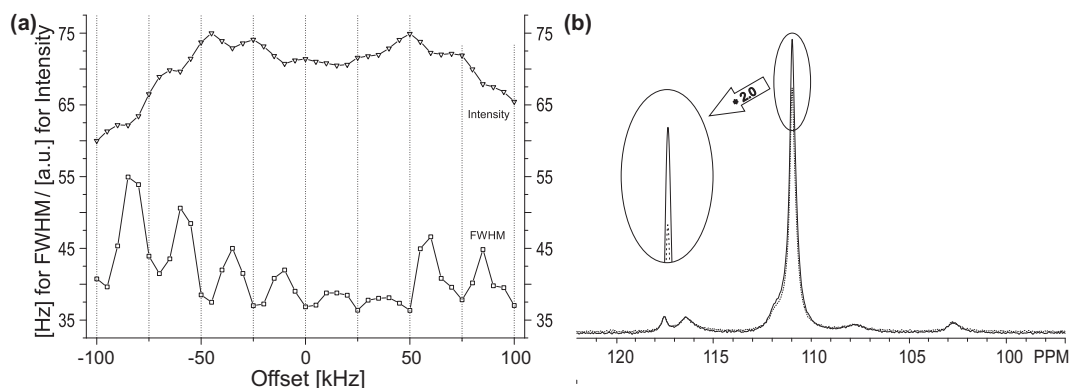


Abbildung 7.1: (a) "Offset"-Charakteristik von XY-16 an einer CF₂-Resonanz von Nafion® bei 25 kHz und (b) Nafion® Spektren, aufgenommen mit (gestrichelte Linie) und ohne (durchgezogene Linie) Verwendung der "Offset"-Bedingung.

Die hohe CSA und große Bandbreite der chemischen Verschiebungen des ¹⁹F legt den Verdacht nahe, dass die Pulse der XY-16-Sequenz nicht in der Lage sind die Spinpopulation vollständig zu invertieren. Dies bestätigte sich bei der Verwendung von, in dieser Hinsicht optimierten, Kompositenpulsen, wie z.B. $90_x 270_y 90_y$ oder $336_x 246_{-x} 10_y 74_{-y} 10_y 246_{-x} 336_x$.⁴⁰ Auf diesem Wege war es möglich, die Signalbreite der ¹³C einer PTFE-Probe um weitere $\sim 1,5$ Hz zu verringern. Dieser relativ kleine Unterschied könnte sich bei Proben mit einer noch höheren CSA und einer breiteren Bandbreite der chemischen Verschiebungen als sehr nützlich erweisen.

Ein großer Nachteil der XY-16-Sequenz ist die Limitierung auf hohe MAS-Geschwindigkeiten. Der Grund hierfür ist in der Tatsache zu finden, dass die homonukleare Spin-Spin-Wechselwirkung ausschließlich durch die MAS-Technik eliminiert wird. Dies war der Grund für die Suche nach einer Entkopplungssequenz, welche bereits bei niedrigen MAS-Geschwindigkeiten eine vergleichbare Entkopplungsleistung erzielt.

Die präsentierten Ergebnisse zeigen, dass die XiX-Sequenz im Vergleich zur XY-16-Sequenz in der Lage ist, bei einer MAS-Frequenz von lediglich 11 kHz eine um 40% verringerte Linienbreite zu erzielen (siehe Abbildung 7.2). Die bei 11 kHz vorliegenden Linienbreiten und Intensitäten sind außerdem vergleichbar mit Werten, welche unter Verwendung der XY-16-Sequenz bei MAS-Frequenzen von über 20 kHz zu finden sind. Angesichts dieser Ergebnisse stellt die XiX-Sequenz speziell dann einen Vorteil da, wenn das MAS auf niedrige Geschwindigkeiten begrenzt ist, z.B. bei der Verwendung großer Rotoren.

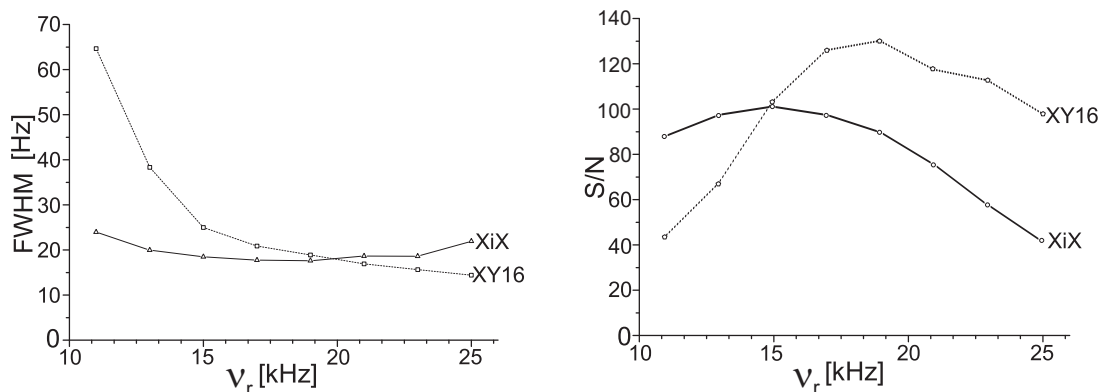


Abbildung 7.2: Signalbreiten (FWHM, links) und Signal-Rausch-Verhältnisse (S/N, rechts) für eine PTFE ^{13}C -Resonanz unter der Verwendung von XY-16- und XiX-Entkopplungen bei verschiedenen MAS-Frequenzen.

Der zweite Teil der Arbeit beschäftigt sich mit der Quantifizierung von NMR-Daten, welche für Membranen unter der Verwendung von Kreuzpolarisationsexperimenten aufgenommen wurden. Eine kostengünstige Alternative bei der Herstellung von Membranen für die Verwendung in Brennstoffzellen ist die Modifizierung von kommerziell erhältlichen teil- oder vollfluorierten Grundmembranen. Dies kann durch radikalisches Pfropfen eines Trägerfilms, z.B. PTFE, geschehen. Hierbei werden in der Membran durch Elektronenbestrahlung Radikale erzeugt, welche mit einer geeigneten Monomer-Lösung in Reaktion gebracht werden. Die Filme dieser Untersuchung basieren auf einem PTFE-Film, welcher mit einer Mischung von α -methylstyrol (AMS) und Methacrylonitril (MAN) modifiziert wurden. Normalerweise findet der sogenannte Pfropfgrad (Degree of Grafting, DoG) zur quantitativen Beschreibung des Vorgangs Verwendung ($\text{DoG} = (m_{\text{graft}} - m_{\text{base}}) / m_{\text{base}}$, wobei m_{base} die Masse des bestrahlten Films und m_{graft} die Masse des Films nach dem Pfropfen ist.).

Aufgrund der Tatsache, dass die hier vorliegenden Filme mittels einer Monomermischung hergestellt wurden, ist der DoG alleine kein geeigneter Parameter um den Prozess zu beschreiben, da er das Verhältnis der zwei Monomere nicht berücksichtigt. Das zur Beschreibung notwendige Monomerverhältnis wird im Normalfall unter Verwendung von Infrarot(IR)-Spektroskopie bestimmt. Das IR-Spektrum weist für beide Monomere zahlreiche Banden auf, welche zur Bestimmung des Verhältnisses dienen können. In der Praxis werden hierfür Kalibrierkurven für zahlreiche Proben aufgenommen.^{47,48}

Ein großer Nachteil dieser Technik ist in der Ausdehnung des Films während

des Propfens zu finden. Die durch die IR-Spektroskopie erfasste Fläche verändert sich dadurch und es muss ein Korrekturfaktor zur Kompensation verwendet werden. Die hier präsentierten Ergebnisse zeigen, dass die $\{^1\text{H}\}^{13}\text{C}$ -CP-NMR-Spektroskopie als alternative Bestimmungsmethode dienen kann. Ein erster notwendiger Schritt hierfür war die Zuordnung aller Signale der ^{13}C -NMR Spektren, welche in Abbildung 7.3 zu finden ist.

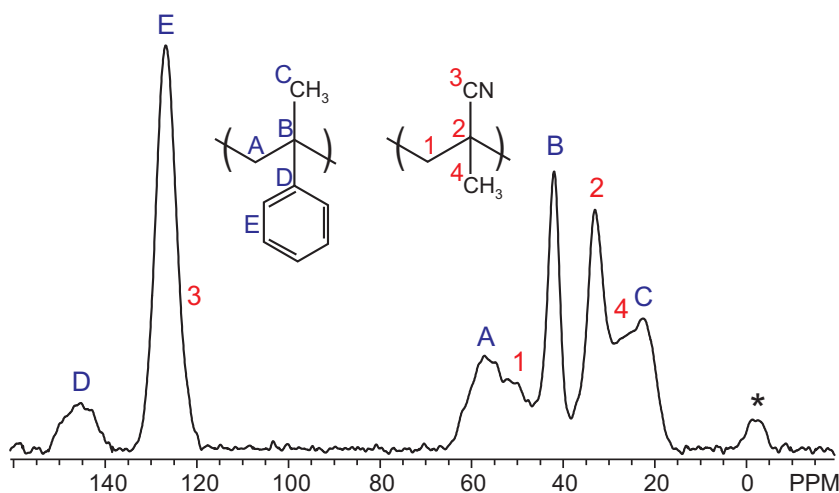


Abbildung 7.3: $\{^1\text{H}\}^{13}\text{C}$ -CP-NMR-Spektrum für eine mit MAN und AMS gepfropfte Probe.

Für die Bestimmung des Verhältnisses wurden die Resonanzen der zwei quartären Kohlenstoffresonanzen in α -Position zur Phenylgruppe (Zuordnung B in Abbildung 7.3, 42 ppm) und neben der Cynaogruppe (Zuordnung 2 in Abbildung 7.3, 33 ppm) gewählt. Da es sich bei beiden Positionen um quartäre Kohlenstoffe handelt, ist eine ähnliche CP-Dynamik zu erwarten. Dieser neue analytische Ansatz wurde in drei Schritten durchgeführt:

- Aufnahme von $\{^1\text{H}\}^{13}\text{C}$ -CP-NMR-Spektren bei einer fixen CT von 5 ms für alle Membranen.
- Aufnahme von CP-Kurven, d.h. die Monomerverhältnisse für verschiedene Kontaktzeiten, für eine Probenauswahl. Auf diesem Wege kann sichergestellt werden, dass das Verhältnis unabhängig von der CT ist.
- Aufnahme von ^{13}C -Ein-Puls-NMR-Spektren für die gleiche Auswahl, um den absoluten Wert in Hinsicht auf eine unterschiedliche CP-Dynamik der zwei ausgewählten Resonanzen zu verifizieren.

Der Fehler für die Bestimmung des AMS:MAN-Verhältnisses durch CP-NMR-Spektroskopie in Bezug auf die CT liegt unter 5%. Die Abweichung in Bezug auf die durch IR-Spektroskopie bestimmten Verhältnisse liegt unter 6%. Die Ergebnisse für die Membran mit einem DoG von 44% sind in Abbildung 7.4 graphisch dargestellt, wobei die durch ^{13}C -Ein-Puls-NMR- und IR-Spektroskopie erhaltenen Werte ebenfalls eingezeichnet sind.

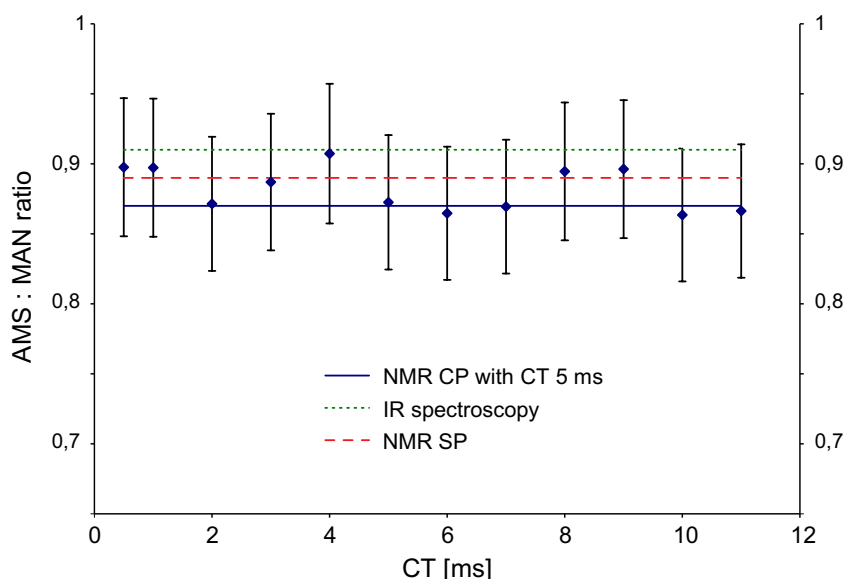


Abbildung 7.4: AMS:MAN-Verhältnis in Abhängigkeit zur CT mit entsprechenden 6%-Fehlerbalken. Die durch ^{13}C -Ein-Puls-NMR- und IR-Spektroskopie erhaltenen Werte sind durch horizontale Linien dargestellt.

Für die Bestimmung der Verhältnisse durch IR-Spektroskopie gilt ein Fehler von 5%. Die durch ^{13}C -Ein-Puls-NMR- und IR-Spektroskopie erhaltenen Werte liegen innerhalb der 6%-Fehlerbalken der CP-Daten. Bereits an diesem Punkt zeigt sich die hohe Übereinstimmung der verschiedenen Messmethoden.

Tabelle 7.1 vereinigt die durch ^{13}C -Ein-Puls-NMR-, ^{13}C -CP-NMR- und IR-Spektroskopie bestimmten Verhältnisse für die Proben mit unterschiedlichem DoG. Für alle Membranen zeigen die verschiedenen Methoden eine hohe Übereinstimmung. Nichtsdestotrotz beinhalten die durch IR-Spektroskopie bestimmten Werte eine durch den Korrekturfaktor verursachte Unsicherheit, während die durch ^{13}C -CP-NMR-Spektroskopie bestimmten Werte durch die potenziell unterschiedliche CP-Dynamik der zwei Signale fehlerbehaftet sein könnten. Erst im Vergleich zu den durch ^{13}C -Ein-Puls-NMR-Spektren ermittelten Werten ergibt sich die hohe Genauigkeit beider

Tabelle 7.1: Durch ^{13}C -Ein-Puls-NMR-, ^{13}C -CP-NMR- und IR-Spektroskopie bestimmten Verhältnisse für die Proben mit unterschiedlichem DoG

DoG [m%]	Molares AMS:MAN-Verhältniss im gefropften Polymer bestimmt durch		
	FT-IR	$\{^1\text{H}\}^{13}\text{C}$ -CP	^{13}C -SP
5	0.84	0.82	—
15	0.85	0.89	—
24	0.91	0.92	—
35	0.92	0.88	0.9
44	0.91	0.87	0.89

Methoden.

Zieht man die hohe Übereinstimmung zwischen ^{13}C -NMR- und IR-Spektroskopie in Betracht, wird Letztere auch in Zukunft als Standardmethode Anwendung finden, wobei die ^{13}C -Ein-Puls-NMR-Daten in Zukunft als Grundlage für den Expansionsfaktor dienen können. Denkt man an aus anderen oder aus mehr als zwei Monomeren aufgebaute Systeme kann die hier vorgestellte NMR-Technik eine ernsthafte Alternative darstellen.

Der letzte Teil der vorliegenden Doktorarbeit beschäftigt sich mit der Möglichkeit, Prozesse während des Kugelmahlens von CaF_2 auf mikro- und nanokristalliner Ebene mittels der Kombination von Röntgendiffraktometrie und NMR-Relaxometrie zu untersuchen. Die vorliegenden Proben wurden durch Kugelmahlen von kommerziell erhältlichem CaF_2 unter Verwendung von Stahl- und Wolframcarbid-Kugeln dargestellt. Die Mahlzeit wurde zwischen 4 h und 64 h variiert (4 h, 8 h, 16 h, 32 h and 64 h). Eine dritte Probenreihe wurde durch gemeinsame Fällung von CaCl_2 und NH_4F in einer Wasser-Ethanol-Mischung hergestellt. Das Verhältnis wurde dabei so variiert, dass Alkoholkonzentrationen von 0%, 30%, 60%, 90% und 100% erzielt wurden.⁶⁸

Für alle, für verschiedene Zeiten gemahlene, CaF_2 -Proben wurden Röntgen-Pulverdiffraktogramme aufgenommen. Zur Analyse und Quantifizierung der Kristallstruktur und ihrer Parameter wurden die Pulverdiffraktogramme nach der "whole powder pattern modelling"-Methode modelliert, welche in Kapitel 2.2.2 ausführlich beschrieben wurde. Diese Methode ist speziell dann geeignet, wenn man die mittlere

Domänengröße und Gitterdefekte simultan bestimmen möchte.^{62,69} Auf diesem Wege wurden die mittlere Fehlerdichte und die mittlere Domänengröße für alle Proben bestimmt. Für die relativ lang gemahlenen Proben ergab sich eine große Übereinstimmung zwischen den gemessenen und den simulierten Pulverdiffraktogrammen, während die Methode nicht in der Lage war, die kurz gemahlenen Proben zufriedenstellend zu beschreiben. Selbst unter der naheliegenden Annahme eines Zweiphasensystems, welches die Inhomogenität zu Beginn des Mahlvorgangs beschreiben könnte, blieb die Simulation instabil und die Parameter korrelierten stark.

Diese Beobachtung konnte durch die ^{19}F -MAS-NMR-Ergebnisse untermauert werden. In einem ersten Schritt wurden gewöhnliche ^{19}F -MAS-NMR-Spektren aufgenommen, welche in allen Fällen lediglich eine breite Resonanz zeigten. Die im Spektrum sichtbaren, stark ausgebildeten Seitenbänder spiegeln die große CSA wider.⁷⁴ Es war selbst durch hohe MAS-Frequenzen nicht möglich, eine Aufspaltung unterscheidbarer Fluor-Spezies zu erzielen.

Für eine weitergehende Untersuchung mittels NMR wurden für alle Proben T_1 -Relaxationsmessung durchgeführt. Hierbei kam die in Kapitel 2.1.5 beschriebene "Saturation-Recovery"-Sequenz zum Einsatz. Die extrahierten Integrale wurden gegen das Zeitinkrement τ aufgetragen und durch Anpassung einer Funktion analysiert. Im Normalfall verwendet man hierbei die im Theorieteil beschriebene Exponentialfunktion.

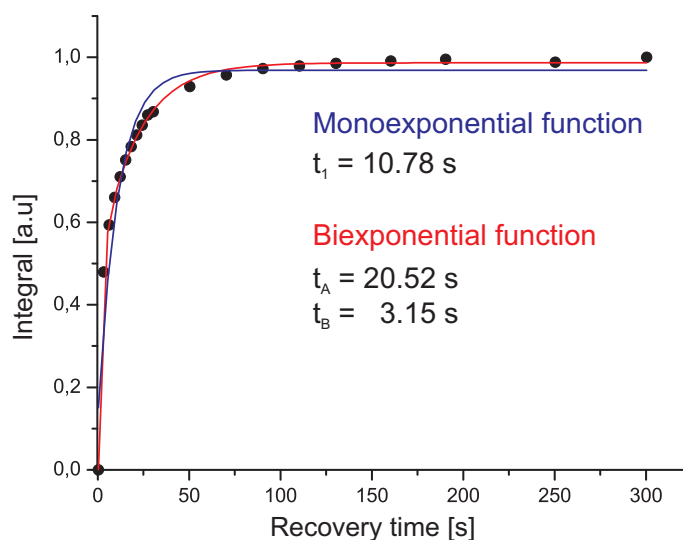


Abbildung 7.5: Extrahierte Relaxationsdaten für die mit WC-Kugeln für 8 h gemahlene Probe und die Anpassungskurven unter Verwendung eines mono- und biexponentiellen Ansatzes.

Für die lange gemahlenen Proben war dies möglich und es konnte ein hohes Maß an Übereinstimmung erzielt werden. Wie bereits bei der Röntgendiffraktometrie, kam es bei den nur kurz gemahlenen Proben zu Anomalien. Die bestmögliche Anpassung unter Verwendung einer monoexponentiellen Funktion ist für eine für 8 h gemahlene Probe in Abbildung 7.5 darstellt und weist für mittlere τ -Werte eine hohe Diskrepanz auf. Um den Relaxationsprozess der kurz gemahlenen Proben zu beschreiben, fand ein biexponentieller Ansatz Anwendung, welcher erneut der Idee des Zweiphasensystems, und somit der zu Beginn vorhandenen Inhomogenität, Rechnung trägt. Unter Verwendung der beiden Funktionen war es möglich, alle Datensätze erfolgreich zu beschreiben (Abbildung 7.5). Die Ergebnisse für die mit WC-Kugeln gemahlen Proben sind in Abbildung 7.6 graphisch dargestellt und zeigen eine Aufspaltung in zwei Komponenten für Mahlzeiten zwischen 4 h und 8 h.

Die zweite Information, welche sich aus den Relaxationsdaten ergibt sind die relativen Anteile C und $(1 - C)$ der zwei so unterscheidbaren Komponenten. Abbildung 7.6 stellt diese graphisch dar, wobei nach 4 h der Anteil von Komponente B bereits stark zugenommen hat, wobei Komponente A nach 8 h Mahlzeit immer noch in der Probe präsent ist. Erst zwischen 8 h und 16 h verschwindet Komponente A vollständig.

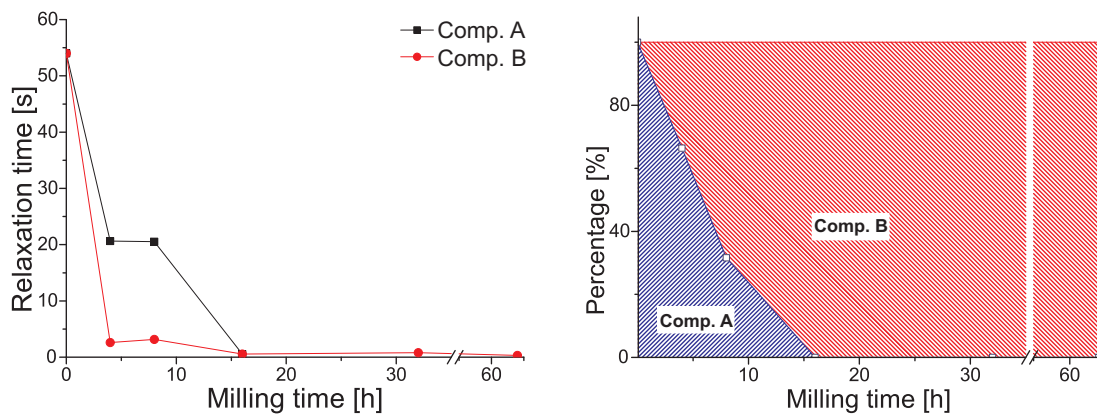


Abbildung 7.6: Abhängigkeit der Relaxationszeit T_1 (links) und der relativen Anteile (rechts) der zwei Komponenten von der Mahlzeit (Das Gebiet zwischen 35 h und 55 h ist ausgespart.)

Im Gegensatz zu den Ergebnissen der Röntgendiffraktometrie ist somit die ^{19}F -Relaxometrie in der Lage, zwei verschiedene Komponenten und die jeweiligen Anteile zu unterscheiden. Direkte Aussagen über die Natur der zwei Komponenten hingegen können an dieser Stelle nicht getroffen werden. Ein solches Verhalten könnte

verschiedene Gründe haben, so ist zum Beispiel bekannt, dass sich in nanokristallinen Materialien das Relaxationsverhalten an der Oberflächen und im inneren der Partikel stark unterscheiden kann.

Diese Frage konnte abschließend geklärt werden, indem die Röntgen- und NMR-Daten simultan angepasst wurden. Hierbei wurde den Relaxationsdaten ein hohes Gewicht bzgl. der relativen Zusammensetzung und den Röntgendaten ein hohes Gewicht bzgl. der Domänengröße und Defektdichte gegeben. Somit konnten die Relaxationsdaten die Zusammensetzung beschreiben, während die Röntgendaten Parameter, wie z.B. die Domänengröße oder die Defektdichte, lieferten. Der Kombinationsansatz lieferte Ergebnisse hoher Qualität für alle Proben und es war somit möglich, ein detailliertes Bild der Prozesse während des Mahlvorganges zu geben.

Zu Beginn des Mahlvorganges liegt mikrokristallines CaF_2 mit einer relativ niedrigen Defektdichte vor. Während einer ersten Mahlphase bilden sich zwei Phasen aus, welche sich in ihrer Domänengröße und Defektdichte unterscheiden. Die Defekte werden durch mechanische Beanspruchung durch die Mahlkugeln induziert, d.h. der Mahlvorgang besteht aus zwei simultanen Effekten: dem eigentlichen Zerkleinern der Partikel und dem Einbringen von Defekten durch mechanische Beanspruchung. Man kann somit sagen, dass sich das Material aus weniger gemahlenen Partikeln mit einer niedrigen Defektkonzentration und bereits stärker gemahlenen Partikeln mit einer höheren Defektkonzentration zusammensetzt. Dies ist korrekt bis zu einer Mahlzeit von 8 h (WC), bzw. 16 h (Fe). Nach längerem Mahlen ist das System homogenisiert und in Bezug auf die Domänengröße stabil, was beim Kugelmahlen einen bekannten Effekt darstellt. Lediglich die Defektkonzentration nimmt durch die fortgeführte mechanische Beanspruchung weiter zu. Somit kann man den Mahlvorgang unabhängig vom gewählten Kugelmateriale in drei Phasen unterteilen:

- Mikrokristallines Material mit einer niedrigen Defektdichte
- Inhomogenes Gebiet, mit zwei in Fehlerdichte und Domänengröße unterscheidbaren Phasen:
 - Größere Domänen mit niedriger Defektkonzentration
 - Kleinere Domänen mit höherer Defektkonzentration
- Homogene Situation mit einer Phase, welche sich durch eine kleine Domänengröße und hohe Defektkonzentration auszeichnet. Während die Domänengröße nicht mehr weiter abnimmt, ist mit steigender Mahlzeit ein Zunahme der Defektkonzentration zu beobachten.

Ein Vergleich der zwei auf diese Weise ermittelten Phasendiagramme ermöglicht es, den Mahlcharakter der zwei verschiedenen Kugelmaterien zu vergleichen (Abbildung 7.7). Die Verwendung von WC-Kugeln führt zu einem schnellen Zerfall von Phase A, wobei bereits nach 16 h nur noch Phase B vorhanden ist. Bei der Verwendung von Stahlkugeln ist dies erst nach 32 h der Fall. Dieser Unterschied spiegelt sich im Elastizitätsmodul der beiden Materialien wieder, welches für WC 500 GPa und für Stahl 196 GPa beträgt. Im Widerspruch hierzu stehen die gefundenen Werte für die mittlere Defektdichte und die mittlere Domänengröße, welche durch die Verwendung von Stahlkugeln stärker beeinflusst sind und es wird ein kleinerer Wert für die Domänengröße und ein höherer Wert für die Fehlerdichte erreicht.

Zusätzlich war es anhand des Kombinationsansatzes möglich, die Größenordnung der verschiedenen Effekte, welche zu einer Verkürzung der Relaxationszeit T_1 führen, zu bestimmen. Durch die Analyse der chemisch hergestellten Proben war es möglich, den Anteil des reinen Größeneffektes zu ermitteln, d.h. der Anstieg des "surface-to-bulk"-Verhältnisses erklärt die Verkürzung der Relaxationszeit bis in die Größenordnung einiger Sekunden, z.B. 5,1 s für die in purem Wasser hergestellte Probe. Der Einfluss der Defekte muss daher für die weitere Verkürzung der Relaxationszeit bis in die Größenordnung von einigen Zehntel einer Sekunden verantwortlich sein, z.B. 0,31 s für die für 64 h mit WC-Kugeln gemahlene Probe. Der paramagnetische Einfluss der Eisenverunreinigungen führt letzten Endes zur Reduktion der Relaxationszeit um eine weitere Potenz, z.B. 0,036 s für die für 64 h mit Fe-Kugeln gemahlene Probe. Unabhängig davon können die Relaxationsdaten dennoch für den oben beschriebenen analytischen Ansatz verwendet werden.

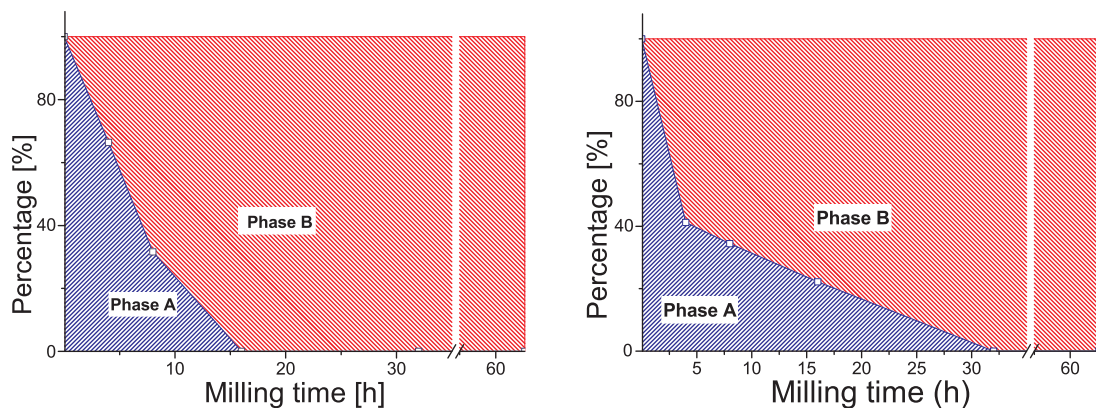


Abbildung 7.7: Phasendiagramme für das Mahlen mit WC- (links) und Fe-Kugeln (rechts).

Abbreviations and variables

α, β	spin states
Q	quadrupole coupling tensor
V	electric field gradient
ΔE	energy of a transition
δ	chemical shift
Δ	path difference
γ	gyromagnetic ratio
\hbar	Planck's constant
λ	wavelength
μ	magnetic moment
ν_a	emergent angle
ν_L	Larmor frequency
ρ	dislocation density
τ	time increment
τ_P	pulse length
τ_R	pulse length of a rotor-synchronous pulse
θ, β	angles

Abbreviations and variables

A	normalized signal integral
B_0	static magnetic field
C	maximum amplitude
d	distance
E	energy
f_e	edge/screw factor
I	magnetic quantum number
M_0	net magnetization
m_i	magnetic quantum number
M_i	magnetization along the i-axis
N_i	population of an energy level
P	intrinsic angular momentum
R_e	local strain field
T_1	spin-lattice relaxation time
$T_{1\rho}$	spin-lattice relaxation time under spin-lock conditions
T_2	spin-spin relaxation time
T_2^*	spin-spin relaxation time including field inhomogeneities
AMS	α -MethylStyrene
APB	Anti-Phase domain Boundaries
C	Composition Fluctuation

CP	Cross-Polarization
CPMG	Carr-Purcell-Meiboom-Gil
CS	Chemical Shift
CSA	Chemical Shift Anisotropy
CT	Contact-Time
cw	Continuous wave
D	Dipolar
D	Lattice Distortions
DoG	Degree of Grafting
F	Faulting
fcc	face-centred cubic
FID	Free Induction Decay
FT	Fourier Transform
FT-IR	Fourier-Transformed InfraRed
FWHM	Full Width Half Maximum
GSR	Grains Surface Relaxation
hetero	heteronuclear
HH	Hartmann-Hahn
homo	homonuclear
IP	Instrumental Profile
IR	Inversion-Recovery

K	Knight shift
K _n , L _n	electron shells
LPA	Line Profile Analysis
MAN	MethAcrylNitrile
MAS	Magic Angle Spinning
NFBS-K	potasium NonaFluoro-1-ButaneSulfonate
NMR	Nuclear Magnetic Resonance
P	Paramagnetic
PFP-Na	sodium PentaFluoro-Propionate
PM2K	Software for WPPM
PTFE	PolyTetraFluoroEthylen
Q	Quadrupolar
QUCP	Quantitative Cross-Polarization
r	distance
RF	RadioFrequency
S	Coherent scattering domain
SP	Single Pulse
SPINAL	decoupling sequence
SR	Saturation-Recovery
TEM	Transmission Electron Microscopy
TPPM	Two-Pulse Phase-Modulated

UV/Vis	UltraVisible/Visible
WC	tungsten carbide
WPPM	Whole Powder Pattern Modelling
XiX	decoupling sequence
XRD	X-Ray Diffraction
XY-16	decoupling sequence
Z	Zeeman

List of Figures

2.1	Quantization for the spin angular momentum P in a magnetic field . . .	9
2.2	Precession double cone for a spin $I = \frac{1}{2}$ nucleus	9
2.3	Energy levels for an $I = \frac{1}{2}$ and an $I = 1$ spin-system	10
2.4	Formation of the macroscopic magnetization for ensemble spin- $\frac{1}{2}$ nuclei	10
2.5	Schematic comparison of the cw- und FT-experiment ¹⁹	12
2.6	90°- and 180°-pulse in the rotating frame	13
2.7	Evolution of the transverse magnetization $M_{y'}$	14
2.8	Schematic FID $f(t)$ for an isolated spin, e.g. in CH ₃ I	15
2.9	Example of a Fourier transform	15
2.10	Powder pattern for a molecule with an axially symmetric chemical shift tensor	17
2.11	Example for J-coupling in an anisotropic solution	18
2.12	Illustration of the orientation dependency of the dipolar coupling ¹⁷ .	19
2.13	Splitting and mixing of degenerate Zeeman levels due to homonuclear dipolar coupling ¹⁷	20
2.14	Splitting of degenerate Zeemann levels due to heteronuclear dipolar coupling ¹⁷	20
2.15	Scheme of an electrical quadrupole	21
2.16	NMR time scale for the most common parameters and experiments .	23
2.17	The dependency of T_1 , T_2 and $T_{1\rho}$ on the correlation time τ_c	24
2.18	Schematic representation of an NMR spectrometer	25
2.19	Rotors and probe-head used for MAS experiments. The Canadian one penny coin has a diameter of 19 mm.	26
2.20	Definition of the angles describing the tensors' orientation with re- spect to the external magnetic field in a MAS experiment	27
2.21	Formation of spinning side-bands at different MAS speeds	28
2.22	¹ H-CW-decoupling during ¹³ C-detection	29
2.23	¹ H-TPPM-decoupling during ¹³ C-detection	30

2.24	^1H -XY16-decoupling during ^{13}C -detection	30
2.25	Single pulse experiment	32
2.26	Spin-echo experiment	32
2.27	Exemplary spin-echo decay curve	33
2.28	Scheme of the inversion-recovery sequence	33
2.29	Exemplary inversion-recovery curve	34
2.30	Scheme of the saturation-recovery sequence	35
2.31	Exemplary saturation-recovery curve	35
2.32	CP experiment for a ^1H - ^{13}C spin system	36
2.33	Scheme for the CP transfer in a ^1H - ^{13}C spin system	37
2.34	Ramped CP experiment for a ^1H - ^{13}C spin system	38
2.35	Diffraction at a 1D-lattice	39
2.36	Destructive interference of scattered waves for a path difference of $\frac{\lambda}{10}$ ²¹	40
2.37	Diffraction of a row of atoms ²¹	41
2.38	Example for lattice planes in a crystal ²¹	41
2.39	Definition of the hkl -values by the reciprocal axis intercepts relative to the unit cell ²¹	42
2.40	Derivation of the Bragg equation ²¹	42
2.41	Scheme of an X-ray tube	43
2.42	Formation of X-ray radiation	43
2.43	Typical X-ray spectrum	44
2.44	Example for a four-circle-diffractometer with "kappa-circle" geometry	44
2.45	Bragg-Brentano-Geometry and an example for a powder diffractometer	45
2.46	PM2K results for a ball milled α -iron alloy ^{22,26} . For description see figure 2.47.	49
2.47	(continued) PM2K results for a ball-milled α -iron alloy ^{22,26}	50
3.1	Comparison of different ^{19}F decoupling methods applied to PTFE	54
3.2	Schemes for the (a) XY-16, (b) XiX, (c) TPPM and (d) cw decoupling sequences	55
3.3	Decoupling performance on PTFE for XY-16 in dependence of the pulse width at a MAS frequency of 25 kHz	56
3.4	Offset characteristics of XY-16 shown for PTFE spectra recorded at (a) 25 kHz and (b) 15 kHz	57

3.5	(a) Offset characteristics of XY-16 showed for the CF ₂ of Nafion [®] at 25 kHz and (b) Nafion [®] spectra recorded for on- (dashed line) and off-resonance (solid line) decoupling	59
3.6	¹³ C { ¹⁹ F} NMR spectra for Nafion [®] recorded under XY-16 and XiX decoupling at a spinning rate of 11 kHz	60
3.7	Dependency of line width and intensity on the τ_p/τ_r -ratio found for PTFE under XiX decoupling	61
3.8	Offset characteristics for XiX decoupling on the PTFE ¹³ C resonance	62
3.9	FWHM of the PTFE ¹³ C signal obtained under XY-16 and XiX decoupling at different spinning rates	63
3.10	S/N of of the PTFE ¹³ C signal obtained under XY-16 and XiX decoupling at different spinning rates	63
4.1	Grafting by the front-mechanism	66
4.2	Build-up curves for the CH ₃ , CN and CO carbon resonances in a { ¹ H} ¹³ C CP spectrum of N-t-Boc-alanine for a (a) normal and a (b) ramped CP sequence. <i>Adopted from Metz et al.</i> ⁴⁹	68
4.3	{ ¹ H} ¹³ C CP NMR spectrum for a sample grafted with MAN.	71
4.4	{ ¹ H} ¹³ C CP NMR spectrum for a sample grafted with a MAN/AMS mixture.	71
4.5	Spectral deconvolution of the region between 0 and 70 ppm using the NUTS NMR utility transformation software (Acorn NMR 2009, Livermore, CA).	72
4.6	Build-up curves for the two quaternary carbons in α -position to the phenyl ring (assignment B in figure 3, 42 ppm) and next to the cyano group (assignment 2 in figure 3, 33 ppm) and the calculated AMS:MAN-ratios.	74
4.7	Comparison of the { ¹ H} ¹³ C CP and the ¹³ C single pulse spectrum recorded for the sample with DoG of 44%.	75
4.8	AMS:MAN-ratio in dependency of the CT with the respective error bars assuming an error of 6 %. The values obtained by FT-IR spectroscopy and the ¹³ C SP spectra are shown as horizontal lines.	76
5.1	X-ray powder patterns recorded for CaF ₂ samples milled for 4 h, 8 h, 16 h, 32 h and 64 h	83

5.2	^{19}F MAS NMR spectra for a CaF_2 sample milled for 16 h and recorded at a spinning rate of 16 kHz	85
5.3	^{19}F MAS NMR spectra for a CaF_2 sample milled for 64 h recorded at a spinning rate of 16 kHz with the saturation-recovery sequence for recovery times τ between 0 s and 16 s	86
5.4	Extracted relaxation data for the sample which was ball-milled for 32 h and the curve fitted by function 5.1.	87
5.5	Extracted relaxation data for the sample ball-milled for 8 h and the best fitting curve for function 5.1.	88
5.6	Extracted relaxation data for the sample ball-milled for 8 h and the fitting curve for the biexponential function 5.2 in comparison with the monoexponential function 5.1.	88
5.7	Dependency of the T_1 relaxation time on the milling time, revealing a splitting in two components for samples milled for 4 h and 8 h (the area between 35 h and 55 h is skipped)	90
5.8	Development of the relative amount of the two components determined by the analysis of the relaxation data (the area between 35 h and 55 h is skipped)	90
5.9	Dependency of the mean domain size on the milling time, revealing a splitting in two components for samples milled for 4 h and 8 h (the area between 35 h and 55 h is skipped)	91
5.10	Dependency of the mean dislocation density on the milling time, revealing a splitting in two components for samples milled for 4 h and 8 h (the area between 35 h and 55 h is skipped)	91
5.11	Wide size distributions for the samples chemically synthesized in different water:ethanol-ratios	96
5.12	^{19}F MAS NMR spectra for a CaF_2 prepared in a water/ethanol mixture and in pure ethanol. The extra peak present in the one prepared in pure ethanol is marked by a asterisk.	97
5.13	Iron analysis as Prussian blue with potassium ferrocyanide (5.3) and as iron thiocyanate by adding potassium thiocyanate (5.4). The milling time increases from the left to the right side and the most right is water as reference.	99

5.14	Iron concentration [wt%] in the samples milled by the use of iron in dependency of the milling time determined as iron thiocyanate by UV/Vis spectroscopy.	99
5.15	^{19}F MAS NMR spectra recorded at a spinning rate of 16 kHz for two samples milled for 16 h under the use of WC and steel material. The higher noise in the lower spectrum is caused by a lower number of signal accumulations.	100
5.16	The dependency of the T_1 relaxation time on the milling time for the samples milled by steel reveals a splitting in two components for samples milled for 4 h, 8 h and 16 h (the area between 35 h and 55 h is skipped)	103
5.17	Development of the relative amounts of the two components in the samples milled by steel determined by the analysis of the relaxation data (the area between 35 h and 55 h is skipped)	103
5.18	Dependency of the mean domain size on the milling time, revealing a splitting in two components for samples milled for 4 h and 8 h (the area between 35 h and 55 h is skipped)	104
5.19	Dependency of the mean dislocation density on the milling time, revealing a splitting in two components for samples milled for 4 h and 8 h (the area between 35 h and 55 h is skipped)	104
5.20	Comparison of the phase-diagrams found for the milling with WC (left graph) and steel (right graph) as material for balls and vial . . .	109
5.21	Comparison of the relaxation times found for the milling with WC (left graph) and steel (right graph) as material for balls and vial . . .	109
6.1	(a) Offset characteristics of XY-16 showed for the CF_2 of Nafion [®] at 25 kHz and (b) Nafion [®] spectra recorded for on- (dashed line) and off-resonance (solid line) decoupling	112
6.2	FWHM (left) and S/N (right) of the PTFE ^{13}C signal obtained under XY-16 and XiX decoupling at different spinning rates	113
6.3	$\{^1\text{H}\}^{13}\text{C}$ CP NMR spectrum for a sample grafted with a MAN/AMS mixture.	114
6.4	AMS:MAN-ratio in dependency of the CT with the respective error bars assuming an error of 6 %. The values obtained by FT-IR spectroscopy and the ^{13}C SP spectra are shown as horizontal lines.	115

6.5	Extracted relaxation data for the sample ball-milled by WC balls for 8 h and the fitting curve for the biexponential function in comparison with the monoexponential function.	117
6.6	Dependency of the relaxation time on the milling time (left side) and the development of the relative amount of the two components (right side). (the area between 35 h and 55 h is skipped)	118
6.7	Comparison of the phase-diagrams found for the milling with WC (left graph) and steel (right graph) as materials for balls and vial . .	120
7.1	(a) "Offset"-Charakteristik von XY-16 an einer CF_2 -Resonanz von Nafion [®] bei 25 kHz und (b) Nafion [®] Spektren, aufgenommen mit (gestrichelte Linie) und ohne (durchgezogene Linie) Verwendung der "Offset"-Bedingung.	122
7.2	Signalbreiten (FWHM, links) und Signal-Rausch-Verhältnisse (S/N, rechts) für eine PTFE ^{13}C -Resonanz unter der Verwendung von XY-16- and XiX-Entkopplungen bei verschiedenen MAS-Frequenzen. . . .	123
7.3	$\{^1\text{H}\}^{13}\text{C}$ -CP-NMR-Spektrum für eine mit MAN und AMS gepfropfte Probe.	124
7.4	AMS:MAN-Verhältnis in Abhängigkeit zur CT mit entsprechender 6%-Fehlerbalken. Die durch ^{13}C -Ein-Puls-NMR- und IR-Spektroskopie erhaltenen Werte sind durch horizontale Linien dargestellt.	125
7.5	Extrahierte Relaxationsdaten für die mit WC-Kugeln für 8 h gemahlene Probe und die Anpassungskurven unter Verwendung eines mono- und biexponentiellen Ansatzes.	127
7.6	Abhängigkeit der Relaxationszeit T_1 (links) und der relativen Anteile (rechts) der zwei Komponenten von der Mahlzeit (Das Gebiet zwischen 35 h und 55 h ist ausgespart.)	128
7.7	Phasendiagramme für das Mahlen mit WC- (links) und Fe-Kugeln (rechts).	130

List of Tables

2.1	Exemplary NMR-active nuclei and their properties	7
2.2	Overview of common interactions in NMR ²⁰	22
4.1	Comparison of the AMS:MAN molar ratios determined with FT-IR spectroscopy	70
4.2	Signal assignment for the $\{^1\text{H}\}^{13}\text{C}$ CP NMR spectra. The signal positions are found in figure 4.4.	72
4.3	Comparison of the AMS:MAN molar ratios determined by the use of the $\{^1\text{H}\}^{13}\text{C}$ CP and ^{13}C single pulse spectra	75
4.4	Results for the AMS:MAN-ratio in dependency on the DoG obtained by the use of the FT-IR $\{^1\text{H}\}^{13}\text{C}$ CP and ^{13}C single pulse spectra . .	77
5.1	X-ray WPPM results for the samples milled for 16 h, 32 h and 64 h. Estimated standard deviations are reported in parentheses, referred to the last significant digits.	84
5.2	Relaxation times for samples milled for different intervals	89
5.3	Results of the combined modelling of the XRD and Solid State NMR data for samples differing in their milling time. Two phases (A, B) were considered for 4 h and 8 h of milling. Estimated standard deviations are reported in parentheses, referred to the last significant digits.	92
5.4	Results of the combined modelling of the XRD and Solid State NMR data for chemically synthesized samples differing in the water:ethanol-ratio during synthesis. Estimated standard deviations are reported in parentheses, referred to the last significant digits.	95
5.5	NMR and X-ray results for the samples milled by steel for 32 h and 64 h. Estimated standard deviations are reported in parentheses, referred to the last significant digits.	101

5.6	Results of the combined modelling of the XRD and Solid State NMR data for samples milled using steel balls and vial differing in their milling time. Two phases (A, B) were considered for 4 h, 8 h and 16 h of milling. Estimated standard deviations are reported in parentheses, referred to the last significant digits.	102
6.1	Results for the AMS:MAN-ratio in dependency on the DoG obtained by the use of the FT-IR $\{^1\text{H}\}^{13}\text{C}$ CP and ^{13}C single pulse spectra . .	116
7.1	Durch ^{13}C -Ein-Puls-NMR-, ^{13}C -CP-NMR- und IR-Spektroskopie bestimmten Verhältnisse für die Proben mit unterschiedlichem DoG . .	126

References

1. R.R. Ernst, G. Bodenhausen, A. Wokaun et al., Principles of nuclear magnetic resonance in one and two dimensions, **1987**, 332
2. T. D. W. Claridge, High-resolution NMR techniques in organic chemistry, **1999**, 19
3. M. Mehring, *Principles of high resolution NMR in solids*, volume 7, Springer-Verlag Berlin, **1983**
4. K. Schmidt-Rohr und H. W. Spiess, Multi-dimensional NMR and polymers, **1994**
5. A. E. Bennett, M. C. Rienstra, M. Auger, K. V. Lakshmi und R.G. Griffin, Heteronuclear decoupling in rotating solids, *The Journal of Chemical Physics*, **1995**, 103(16), 6951
6. P. Tekely, P. Palmas und D. Canet, Effect of proton spin exchange on the residual ^{13}C MAS NMR linewidths. Phase-modulated irradiation for efficient heteronuclear decoupling in rapidly rotating solids, *Journal of Magnetic Resonance, Series A*, **1994**, 107(2), 129
7. T. K. Pratum, Correction for anisotropic off-resonance decoupling effects in CP MAS of moderate susceptibility materials, *Chemical Physics Letters*, **1990**, 172(3-4), 291–294
8. S. F. Liu und K. Schmidt-Rohr, High-resolution solid-state ^{13}C NMR of fluoropolymers, *Macromolecules*, **2001**, 34(24), 8416
9. D. M. Grant und R. K. Harris, Encyclopedia of nuclear magnetic resonance, volume 1-9, *England: John Wiley & Sons Ltd*, **1996**, 62

References

10. G. Hou, F. Deng, S. Ding, R. Fu, J. Yang und C. Ye, Quantitative cross-polarization NMR spectroscopy in uniformly ^{13}C -labeled solids, *Chemical Physics Letters*, **2006**, 421(4-6), 356
11. X. Yang und K. Müller, Solid-state nmr studies on the guest ordering and dynamics in α , ω -dibromoalkane/urea inclusion compounds, *Applied Magnetic Resonance*, **2007**, 32(3), 407
12. C. Heuber, F. Formaggio, C. Baldini, C. Toniolo und K. Müller, Multinuclear solid-state-NMR and FT-IR-absorption investigations on lipid/trichogin nilayers, *Chemistry & biodiversity*, **2007**, 4(6), 1200
13. J. A. Villanueva-Garibay, M. Abele und K. Müller, Solid-state NMR investigations on complex disordered materials, *Encyclopedia of Analytical Chemistry*
14. P. J. McDonald, J.-P. Korb, J. Mitchell und L. Monteilhet, Surface relaxation and chemical exchange in hydrating cement pastes: A two-dimensional NMR relaxation study, *Phys. Rev. E*, **2005**, 72, 11409
15. L. Miljkovic, D. Lasic, J. C. MacTavish, M. M. Pintar, R. Blinc und G. Lahajnar, Nmr studies of hydrating cement: A spin-spin relaxation study of the early hydration stage, *Cement and Concrete Research*, **1988**, 18(6), 951
16. A. M. Kenwright, K. J. Packer und B. J. Say, Numerical simulations of the effects of spin-diffusion on NMR spin-lattice relaxation in semicrystalline polymers, *Journal of Magnetic Resonance*, **1986**, 69(3), 426
17. M. Duer, Solid-State NMR Spectroscopy, *Blackwell Publishing, Oxford*, **2004**
18. H. Friebolin, Ein- und Zwei-Dimensionale NMR-Spektroskopie, *Wiley-VCH, Weinheim*, **2006**
19. K. Müller und H. Dilger, *Physikalisch-Chemisches Fortgeschrittenen-Praktikum, Universität Stuttgart*, **2008**
20. M. E. Smith, Multinuclear Solid-State NMR of Inorganic Materials, *Pergamon, Ibbenbüren*, **2002**
21. W. Massa, Kristallstrukturbestimmung, *Teubner-Verlag, Stuttgart*, **2004**

22. P. Scardi, M. Ortolani und M. Leoni, WPPM: Microstructural analysis beyond the Rietveld method, *Materials Science Forum*, **2010**, 651, 155
23. P. Scherrer, Bestimmung der Grösse und der inneren Struktur von Kolloidteilchen mittels Röntgenstrahlen, *Nachr. Ges. Wiss. Göttingen*, **1918**, 2, 98
24. A. Guinier, X-ray diffraction in crystals, imperfect crystals, and amorphous bodies, *Dover Publications*, **1994**
25. M. Leoni, T. Confente und P. Scardi, PM2K: a flexible program implementing Whole Powder Pattern Modelling, *Zeitschrift für Kristallographie Supplements*, **2006**, page 249
26. G. Caglioti, A. Paoletti und F.P. Ricci, Choice of collimators for a crystal spectrometer for neutron diffraction, *Nuclear Instruments*, **1958**, 3(4), 223
27. A. Detken, E. H. Hardy, M. Ernst und B. H. Meier, Simple and efficient decoupling in magic-angle spinning solid-state NMR: the XiX scheme, *Chemical Physics Letters*, **2002**, 356(3-4), 298
28. B. M. Fung, A. K. Khitrin und K. Ermolaev, An improved broadband decoupling sequence for liquid crystals and solids, *Journal of Magnetic Resonance*, **2000**, 142(1), 97
29. T. Gullion und M. S. Conradi, Time symmetries in rotating sample NMR, *Journal of Magnetic Resonance*, **1990**, 86(1), 39
30. M. Weingarth, P. Tekely und G. Bodenhausen, Efficient heteronuclear decoupling by quenching rotary resonance in solid-state NMR, *Chemical Physics Letters*, **2008**, 466(4-6), 247
31. K. A. Mauritz und R. B. Moore, State of understanding of Nafion, *Chem. Rev*, **2004**, 104(10), 4535
32. B. Smitha, S. Sridhar und A. A. Khan, Solid polymer electrolyte membranes for fuel cell applications - a review, *Journal of Membrane Science*, **2005**, 259(1-2), 10–26

33. Q. Chen und K. Schmidt Rohr, Backbone dynamics of the Nafion ionomer studied by ^{19}F - ^{13}C Solid State NMR, *Macromolecular Chemistry and Physics*, **2007**, 208(19-20), 2189
34. Q. Chen und K. Schmidt-Rohr, ^{19}F and ^{13}C NMR signal assignment and analysis in a perfluorinated ionomer (Nafion) by two-dimensional solid-State NMR, *Macromolecules*, **2004**, 37(16), 5995
35. L. Ghassemzadeh, M. Marrony, R. Barrera, K. D. Kreuer, J. Maier und K. Müller, Chemical degradation of proton conducting perfluorosulfonic acid ionomer membranes studied by solid-state nuclear magnetic resonance spectroscopy, *Journal of Power Sources*, **2009**, 186(2), 334
36. M. Body, G. Silly, C. Legein und J. Y. Buzaré, Correlation between ^{19}F environment and isotropic chemical shift in barium and calcium fluoroaluminates, *Inorg. Chem*, **2004**, 43(8), 2474
37. B. Ruprecht, M. Wilkening, A. Feldhoff, S. Steuernagel und P. Heitjans, High anion conductivity in a ternary non-equilibrium phase of BaF_2 and CaF_2 with mixed cations, *Physical Chemistry Chemical Physics*, **2009**, 11(17), 3071–3081
38. C. Vinod, P. K. Madhu, P. Wormald und T. Bräuniger, Frequency-swept pulse sequences for ^{19}F heteronuclear spin decoupling in solid-state NMR, *Journal of Magnetic Resonance*, **2010**, 206(2), 255
39. Z. Gan und R. R. Ernst, Frequency- and phase-modulated heteronuclear decoupling in rotating solids, *Solid State Nuclear Magnetic Resonance*, **1997**, 8(3), 153
40. R. Tycko, H. M. Cho, E. Schneider und A. Pines, Composite pulses without phase distortion, *Journal of Magnetic Resonance*, **1985**, 61(1), 90
41. M. Carravetta, M. Edén, X. Zhao, A. Brinkmann und M. H. Levitt, Symmetry principles for the design of radiofrequency pulse sequences in the nuclear magnetic resonance of rotating solids, *Chemical Physics Letters*, **2000**, 321(3-4), 205
42. M. V. Rouilly, E. R. Kötz, O. Haas, G. G. Scherer und A. Chapiro, Proton exchange membranes prepared by simultaneous radiation grafting of styrene

- onto teflon-FEP films. Synthesis and characterization, *Journal of Membrane Science*, **1993**, 81(1-2), 89
43. B. Gupta und G. G. Scherer, Proton exchange membranes by radiation-induced graft copolymerization of monomers into teflon-FEP films, *CHIMIA International Journal for Chemistry*, **1994**, 48(5), 127
 44. M. M. Nasef und E. S. A. Hegazy, Preparation and applications of ion exchange membranes by radiation-induced graft copolymerization of polar monomers onto non-polar films, *Progress in Polymer Science*, **2004**, 29(6), 499
 45. F. Wallasch, M. Abele, L. Gubler, A. Wokaun und K. Müller, Characterization of radiation grafted polymer films using CP/MAS NMR spectroscopy and confocal Raman microscopy, *Journal of Applied Polymer Science*, **accepted**
 46. G.G. Scherer, Polymer membranes for fuel cells, *Berichte der Bunsengesellschaft für physikalische Chemie*, **1990**, 94(9), 1008
 47. L. Gubler, M. Slaski, A. Wokaun und G. G. Scherer, Advanced monomer combinations for radiation grafted fuel cell membranes, *Electrochemistry Communications*, **2006**, 8(8), 1215
 48. L. Gubler, M. Slaski, F. Wallasch, A. Wokaun und G. G. Scherer, Radiation grafted fuel cell membranes based on co-grafting of α -methylstyrene and methacrylonitrile into a fluoropolymer base film, *Journal of Membrane Science*, **2009**, 339(1), 68
 49. G. Metz, M. Ziliox und S. O. Smith, Towards quantitative CP MAS NMR, *Solid State Nuclear Magnetic Resonance*, **1996**, 7(3), 155–160
 50. B. J. Van Rossum, C. P. De Groot, V. Ladizhansky, S. Vega und H. J. M. De Groot, A method for measuring heteronuclear (^1H - ^{13}C) distances in high speed MAS NMR, *Journal of the American Chemical Society*, **2000**, 122(14), 3465
 51. G. G. Amatucci und N. Pereira, Fluoride based electrode materials for advanced energy storage devices, *Journal of Fluorine Chemistry*, **2007**, 128(4), 243
 52. S. Chandra, Superionic solids: Principles and applications, *North-Holland Publishing Co.*, **1981**

53. G. A. Niklasson und C. G. Granqvist, Electrochromics for smart windows: thin films of tungsten oxide and nickel oxide, and devices based on these, *J. Mater. Chem.*, **2006**, 17(2), 127
54. P. Heitjans und S. Indris, Diffusion and ionic conduction in nanocrystalline ceramics, *Journal of Physics: Condensed Matter*, **2003**, 15, R1257
55. H. Gleiter, Nanocrystalline materials, *Progress in Materials Science*, **1989**, 33(4), 223
56. R. W. Siegel, Encyclopedia of applied physics, volume 11, *VCH, New York*, **1994**
57. J. Y. Ying und T. Sun, Research needs assessment on nanostructured catalysts, *Journal of Electroceramics*, **1997**, 1(3), 219
58. G. De Giudici, R. Biddau, M. D'incanu, M. Leoni und P. Scardi, Dissolution of nanocrystalline fluorite powders: An investigation by XRD and solution chemistry, *Geochimica et cosmochimica acta*, **2005**, 69(16), 4073
59. H. P. Klug und L. E. Alexander, X-ray diffraction procedures: for polycrystalline and amorphous materials, *X-Ray Diffraction Procedures: For Polycrystalline and Amorphous Materials, 2nd Edition*, **1974**, 1, 992
60. J. Martinez-Garcia, M. Leoni und P. Scardi, A general approach for determining the diffraction contrast factor of straight-line dislocations, *Acta Crystallographica Section A: Foundations of Crystallography*, **2009**, 65(2), 109
61. H. Gleiter, Nanostructured materials: basic concepts and microstructure, *Acta materialia*, **2000**, 48(1), 1
62. E. J. Mittemeijer und P. Scardi, Diffraction analysis of the microstructure of materials, *Springer Verlag*, **2004**, 68
63. H. Eckert, Solid state nuclear magnetic resonance: a versatile tool in solid state chemistry and materials science, *Bunsen-Magazin*, **2008**, 10
64. B. Ruprecht, M. Wilkening, S. Steuernagel und P. Heitjans, Anion diffusivity in highly conductive nanocrystalline BaF₂: CaF₂ composites prepared by high-energy ball milling, *J. Mater. Chem.*, **2008**, 18(44), 5412

- 65. P. Jain, S. Kim, R. E. Youngman und S. Sen, Direct observation of defect dynamics in nanocrystalline CaF_2 : Results from ^{19}F MAS NMR spectroscopy, *The Journal of Physical Chemistry Letters*, **2010**, 1(7), 1126
- 66. F. Qi, C. Rier, R. Böhmer, W. Franke und P. Heitjans, Ion hopping in crystalline and glassy spodumene $\text{LiAlSi}_2\text{O}_6$: ^7Li spin-lattice relaxation and ^7Li echo NMR spectroscopy, *Physical Review B*, **2005**, 72(10), 104301
- 67. G. Scholz, I. Dorfel, D. Heidemann, M. Feist und R. Stösser, Nanocrystalline CaF_2 particles obtained by high-energy ball milling, *Journal of Solid State Chemistry*, **2006**, 179(4), 1119
- 68. F. Wang, X. Fan, D. Pi und M. Wang, Synthesis and luminescence behavior of Eu^{3+} -doped CaF_2 nanoparticles, *Solid state communications*, **2005**, 133(12), 775
- 69. P. Scardi und M. Leoni, Whole powder pattern modelling, *Acta Crystallographica Section A: Foundations of Crystallography*, **2002**, 58(2), 190
- 70. A. Munoz, A. Domínguez-Rodríguez und J. Castaing, Slip systems and plastic anisotropy in CaF_2 , *Journal of Materials Science*, **1994**, 29(23), 6207
- 71. O. Madelung, K. Kuchitsu, E. Hirota, H. Landolt und R. Börnstein, Landolt-Börnstein: Numerical data and functional relationships in science and technology. Atomic and molecular physics. Structure data of free polyatomic molecules, **1992**
- 72. T. Ungar, I. Dragomir, A. Revesz und A. Borbely, The contrast factors of dislocations in cubic crystals: the dislocation model of strain anisotropy in practice, *Journal of applied crystallography*, **1999**, 32(5), 992
- 73. M. Wilkens, Fundamental aspects of dislocation theory, *National Bureau of Standards Special Publication*, **1970**, 317(11), 1195
- 74. K. A. Smith und D. P. Burum, Application of fluorine-19 cramps to the analysis of calcium fluoride/fluoroapatite mixtures, *Journal of Magnetic Resonance (1969)*, **1989**, 84(1), 85
- 75. S. R. Rabbani und D. T. Edmonds, Nuclear spin-lattice relaxation-time reduction in small particles, *Physical Review B*, **1994**, 50(9), 6184